POLITECNICO DI MILANO
Ph.D. in Aerospace Engineering – XXIV cycle

Computational Aeroservoelasticity of Free-Flying Deformable Aircraft

Ph.D. candidate:
Giulio Romanelli

Supervisor:
Prof. Paolo Mantegazza

Tutor:
Prof. Chiara Bisagni

Coordinator:
Prof. Sergio Ricci

March 2012

I now walk into the wild
Chris McCandless, 1992

Contents

Abstract

The reduced weight and improved efficiency of modern, highly flexible, aeronautical structures (as a consequence of multidisciplinary optimization procedures and the extensive use of composite materials) result in a smaller and smaller separation of rigid and elastic modes frequency ranges. Therefore the availability of an integrated environment for tackling both static (stability derivatives correction, control surfaces efficiency, non-linear trim of maneuvering flexible aircraft) and/or dynamic (flutter, gust and turbulence response, active control systems design) aeroservoelastic problems is almost mandatory from the very beginning of the design process. Together with the availability of more and more powerful computing resources, current trends pursue the adoption of high-fidelity tools and state-of-the-art technology within the very active and fruitful research fields of Computational Structural Dynamics (CSD), Multibody System Dynamics (MSD) and Computational Fluid Dynamics (CFD). This choice is somehow obliged when dealing with non-linear aeroservoelastic phenomena, such as transonic flutter, aileron buzz and buffeting.

The objective of the present work is to illustrate the design and implementation of a platform for solving multidisciplinary non-linear Fluid-Structure Interaction (FSI) problems with a partitioned approach, that is coupling high-fidelity state-of-the-art CSD/MSD and CFD tools by means of a robust, flexible aeroelastic interface scheme. We deal with mesh deformation by means of a novel hierarchical strategy particularly suited for the aeroservoelastic simulation of free flying aircraft. A significant challenge consists in demonstrating that such a platform can be assembled using free software.

The credibility of the proposed aeroservoelastic analysis toolbox is assessed by tackling a set of realistic static and dynamic problems such as the non-linear trim of the HiReNASD wing (selected for the 1-st AIAA Aeroelastic Prediction Workshop), the non-linear trim of a free-flying deformable A320 aircraft (investigating different design concepts of innovative wing tip devices), the evaluation of the transonic flutter boundary for the AGARD 445.6 wing and the design and verification of an active control system for flutter suppression for the BACT wing. The results are compared with reference experimental and numerical data available in literature.

Sommario

La diminuzione del peso e l'incremento dell'efficienza delle strutture aeronautiche moderne caratterizzate da una flessibilità elevata (in conseguenza delle tecniche di ottimizzazione multidisciplinare e del sempre maggiore utilizzo di materiali compositi) comportano una sempre minore separazione in frequenza tra i modi rigidi ed elastici del velivolo. Di conseguenza la disponibilità di un ambiente integrato per affrontare problemi di aeroservoelasticità statica (correzione delle derivate di stabilità, efficienza delle superfici di controllo, trim di un velivolo deformabile in manovra) e/o dinamica (flutter, risposta a raffica e turbolenza, progetto e verifica di sistemi di controllo attivo) è fondamentale sin dalle prime fasi di progetto. Grazie alla disponibilità di risorse di calcolo sermpre più potenti, la tendenza attuale è quella di adottare modelli matematici e metodi numerici sempre più sofisticati e ad alta fedeltà appartenenti alla Computational Structural Dynamics (CSD) e/o Multibody System Dynamics (MSD) per il sotto-sistema strutturale ed alla Computational Fluid Dynamics (CFD) per il sotto-sistema aerodinamico. Tale scelta è obbligata per affrontare problemi aeroservoelastici non-lineari quali flutter transonico, aileron buzz e buffeting.

L'obiettivo di questo lavoro consiste nell'illustrare il progetto e l'implementazione di una piattaforma per risolvere problemi di Fluid-Structure Interaction (FSI) secondo un approccio partizionato, accoppiando strumenti allo stato dell'arte CSD/MSD e CFD mediante un opportuno schema di interfaccia aeroelastica flessibile e robusto. Il problema di deformazione della griglia di calcolo è risolto grazie ad un'innovativa strategia gerarchica particolarmente adatta per applicazioni aeronautiche. Una sfida impegnativa consiste nel dimostrare che tale obiettivo può essere raggiunto utilizzando esclusivamente software libero.

Tale toolbox di analisi aeroservoelastica è messo alla prova affrontando una serie di problemi realistici statici e dinamici quali il trim non lineare dell'ala HiReNASD, il trim non lineare del velivolo A320 in manovra, il calcolo del flutter transonico dell'ala AGARD 445.6 e il progetto e la verifica di un sistema di controllo attivo per la soppressione del flutter per l'ala BACT. I risultati sono confrontati con dati sperimentali e numerici di riferimento disponibili in letteratura.

1

Introduction

This Chapter provides an overview of the motivation, the background and the organization of the present work. As described in §1.1, the present work deals with the design and implementation of a high-fidelity multidisciplinary analysis toolbox of free software to tackle real-world aeroservoelastic problems. The continuous achievements in terms of mathematical models, numerical methods, computational resources and costs discussed in §1.2 provide the background for the growing importance of integrated environments in today's aeronautical industry. Finally in §1.3 the outline of the present work is presented, highlighting the results achieved, the original contributions and the future challenges.

1.1 Motivation

The aeroservoelastic interaction between aerodynamic, elastic and control forces tends to dominate the behavior of modern, highly flexible, aeronautical structures. In fact, as a consequence of the weight savings and efficiency improvements resulting from e.g. multidisciplinary optimization procedures, extensive use of composite materials, the frequency separation between rigid and elastic modes of the aircraft is significantly reduced if not even canceled. Therefore the availability of an integrated environment for accurately and efficiently tackling both static (e.g. stability derivatives correction, control surfaces efficiency, non-linear trim of maneuvering flexible aircraft) and/or dynamic (e.g. flutter, gust and turbulence response, active control systems design) aeroservoelastic problems is almost mandatory from the very beginning of the design process. [71, 74]

At the beginning of the first century of flight, aeroelasticity was ignored during the design process. Later, when the first catastrophic failures occurred, it was given new prominence and theories and testing were developed to eliminate problems. Eventually aeroelasticity became a required part of safety-check procedures for new designs, forcing modifications that were considered by designers to be aeroelastic penalties.

Only recently aeroelasticity has progressed from a problem area to become one of the first areas to use integrated technologies to turn problems into opportunities and harness aeroelastic interactions to improve airplane performance. [52, 61]

Any military or civil aircraft must meet the aeroelastic elements of the requirements against which the aircraft is qualified. For instance civil aircraft are designed to meet EASA and/or FAA requirements [84, 83] with a common top level objective: to ensure that the aircraft is free from flutter and other aeroelastic instabilities throughout the flight envelope. For aeroelastic clearance the flight envelope is bounded by the design dive speed V_D and to ensure freedom from flutter within the flight envelope, the concept of the flutter margin has been introduced with the usual requirement that no flutter must exist within the flight envelope expanded by 15% on V_D. The concept of the flutter margin has served the community well in providing a reasonable margin of safety. The factors addressed within the concept of the flutter margin include: a) possible variability between individual aircraft manufactured, b) possible differences in mass distribution from the test conditions, c) variation of structural properties with aircraft age and d) other inaccuracies of modelling and/or testing. Within such a regulatory framework the general decline in flutter incidents, over the last 25 year, has been taken, in some quarters, to imply that flutter has been solved. However, this view is overly optimistic and dangerously complacent and there are many reasons why more sophisticated aeroelastic modelling and prediction will be required for future conventional and unconventional applications. [21, 45]

In fact the specific meaning of the words “conventional” and “unconventional” depends on the disciplinary context. From an aerodynamic perspective the overall shape of the vehicle, the flow regime in which it operates and details such as high-lift devices and flow-control determine whether the configuration is conventional or unconventional. For the structural designer conventional refers to the types of material used, the geometry of the structural layout, the thermal environment and design details such as actuation and shape control mechanisms. From the control perspective the level of complexity and the degree to which it departs from past designs will depend on sensing, actuation and control technologies used, including analytical foundation, software and hardware of control law mechanization. Aeroelasticity involves all of the preceding considerations. [53]

In recent years some challenging aeroelastic problems have been tackled for the very first time, such as the study of the highly non-linear transonic flutter, buzz and buffeting phenomena. A better understanding of these phenomena is important to design more efficient and safer aircraft. In fact the typical mission envelope of many modern civil and military aircraft includes long segments of flight in the transonic regime, highly non-linear because of the simultaneous presence within the flow-field of locally subsonic and supersonic regions and shock waves: the appearance of shock waves may provoke a significant and sudden drop of the flutter velocity, the so-called transonic dip phenomenon. [1, 46, 47] Moreover the position of the shock waves can rapidly change in response to motion of the wings and more in particular the non-linear interaction of control surfaces with shock waves is referred to as buzz and can severely affect aircraft maneuverability, as in the T-45 trainer. [65] Finally in many modern military aircraft it is desirable to preserve a decent maneuverability even at high angle of attacks. This is achieved using tailored leading-edge extensions (LEX)

to generate vortices and enhance lift as in the F/A-18 fighter. However if the so-called vortex breakdown phenomenon occurs ahead of the twin vertical tail surfaces, high frequency oscillations of the aerodynamic loads (buffeting) on the twin vertical tail surfaces may provoke structural fatigue problems. [59, 69]

It is clear that inability to model and predict such non-linear aeroservoelastic behaviour is resolved by extensive flight test programmes, informed through experimental, empirical or simplified modelling, techniques. This is an expensive approach to qualification and has the major disadvantage that should an aeroservoelastic susceptibility be identified, redesign must take place late in the development cycle: again this can be (and usually is) extremely costly. New approaches to high-fidelity aeroservoelastic modelling and prediction tools are needed to reduce the costs and risks of current processes. This is true, not only for new designs, but also for existing aircraft that may go through several major upgrades (and in the case of military aircraft be fitted with new weapons) when re-certification is required. [21]

The coupling of dedicated state-of-the-art fluid and structure solvers for aeroservoelastic analysis of free-flying deformable aircraft is a well established research topic. Together with the availability of more powerful computing resources, current trends pursue the adoption of high-fidelity mathematical models and numerical methods, e.g. Computational Structural Dynamics (CSD) or Multibody System Dynamics (MSD) for the structural sub-system and Computational Fluid Dynamics (CFD) for the aerodynamic sub-system. [15] This choice is somehow obliged when dealing with non-linear aeroservoelastic phenomena. In fact the classical, computationally efficient, linearized numerical methods to evaluate the unsteady aerodynamic loads due to a structural displacement such as the Doublet Lattice Method (DLM) cannot be used as a black-box tool and empirical corrections based on expensive wind tunnel experiments must be applied to yield reliable information. It is then necessary to focus on the more sophisticated mathematical models and numerical methods within the very active and fruitful research field of Computational Aeroelasticity (CA). [92] At the same time it is also important to carefully monitor the run-time and memory requirements of such tools, since a very large number of numerical simulations must be accounted for in order to complete the aeroelastic analysis even only of an isolated wing. Starting in the 1970s with the first numerically viable non-linear mathematical models such as the Transonic Small Disturbances (TSD) and Non Linear Full Potential (NLFP) equations, the fidelity of the analysis tools has been constantly increasing thanks to the more and more powerful computer hardware available. [52] In the 1980s the Euler equations and in the 1990s the Reynolds Averaged Navier-Stokes (RANS) equations have been firstly used for three-dimensional aeroelastic applications. [26] Recently even more complex options are being surveyed, such as the enrichment of turbulence models with the so-called Detached Eddy Simulation (DES) in order to predict massively separated flow. [59] The present trend in the aerospace industry, even in preliminar design, is that of replacing or better placing side by side the low-fidelity efficient methods with the high-fidelity more expensive ones. [87]

The objective of the present work is to illustrate the implementation of a platform for solving intrinsically multidisciplinary non-linear Fluid-Structure Interaction (FSI) problems with a partitioned approach, that is coupling high-fidelity state-of-the-art CSD/MSD and CFD tools by means of a robust, flexible aeroelastic interface scheme.

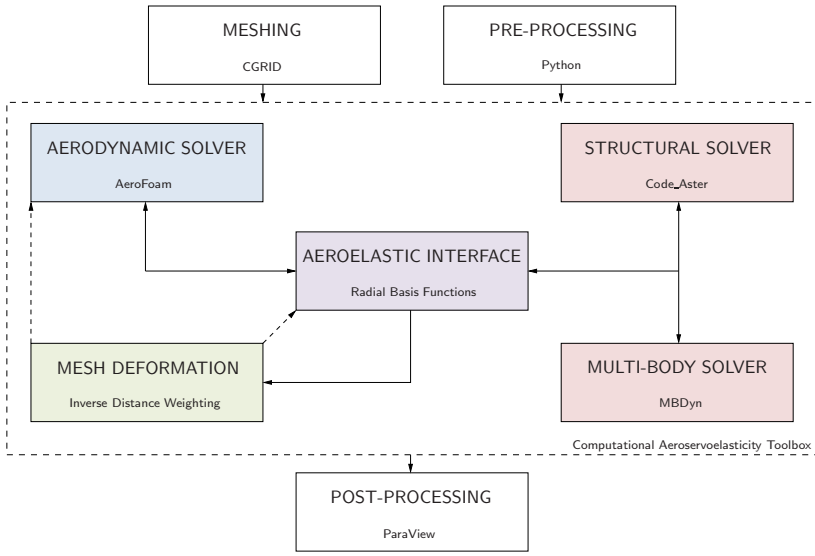

Figure 1.1: Architecture of the proposed high-fidelity toolbox for aeroservoelastic analysis.

A significant challenge consists in demonstrating that such a toolbox to effectively solve non-linear aeroservoelastic problems in both an academic and an industrial environment can be built using, maybe for the first time, exclusively free software, not only for the numerical simulation of the structural and aerodynamic sub-systems, but also for the pre/post-processing stages.

With reference to the block diagram of Figure 1.1, the architecture of the toolbox can be summarized as follows: the aeroelastic interface provides all the functionalities necessary to link the structural sub-system with the aerodynamic one. The structural sub-system can be modelled with the Finite-Element (FE) solver Code_Aster [82] or the Multi-Body (MB) solver MBDyn [85]. It is also possible to build the structural model by importing e.g. the results of the modal analysis of a general commercial software such as Nastran, a "de-facto" standard tool within the aeronautical industry. The aerodynamic sub-system is modelled with the Finite-Volume (FV) aerodynamic solver AeroFoam developed within the collaborative project OpenFOAM. [72, 86] Moreover for dealing with moving boundary problems in Arbitrary Lagrangian Eulerian (ALE) formulation a dedicated hierarchical mesh deformation tool is also available. [80, 91] Such a graphical representation closely matches the actual structure of the Python script responsible of supervising all the workflow and which is based on the three following suitably wrapped C^{++} libraries: myMesh, mySolver and myInterface.

1.2 Background

Due to global competition, economical and ecological pressures, the aircraft industry now needs to deliver products which are better, faster and cheaper to produce. This shift in design paradigm forces the rethinking of the design and production process.

Such a challenge can be addressed by allowing each subsystem design to proceed simultaneously supported by fast, cost-effective and accurate data obtained through high-fidelity simulation for each contributing sub-discipline as well as for the complex interdisciplinary dependencies among them. [87]

Within such a framework it is worthwhile to survey the evolution in recent years of Computational Fluid Dynamics (CFD) and Computational Aeroservoelasticity (CA) to fully appreciate the milestones achieved in terms of high-fidelity modelling and multidisciplinary integration respectively.

1.2.1 New challenges in aircraft design

Since the birth of flight, and until the early 1990s, the driving force behind aerospace products and systems has predominantly been the goals of higher, faster and farther (technology-driven design). But starting in the 1990s with the privatization of the aircraft industry, and driven by world-wide competition (globalization), economical and ecological pressures and the need to finance new products over the capital markets, the aerospace field is now challenged to offer products that are both better in performance and faster and cheaper to produce (market-driven design). Thus the current business market forces airframe designers towards the strong necessity of risk minimization and a definitive reduction of costs and time-to-market. [44]

The possibility to influence the life-cycle costs (for military planes), or the direct operating costs (for commercial planes), of an aircraft design is the largest in the early design stages, followed by a rapid decrease in the more detailed design phases. More in particular within the early product definition phase the final manufacturing, operation and support costs are fixed to a large degree. This may pertain to as much as $70\% - 80\%$ of the life-cycle cost. This observation shows that to increase the life-cycle value (or to decrease the life-cycle cost and direct operating costs) of an aircraft, one should re-think the early stages of the design process to include requirements on life-cycle costs, operating costs, maintenance costs, etc. on the design. It also means that high-fidelity simulations must enter the design cycle earlier.

In order to meet these changing markets and challenging demands of "first-time right", the aerospace industry since the middle of the 1990s, has been moving towards a more integrated design approach with underlying concepts like Virtual Product (VP) or the closely related Integrated Product and Process Development (IPPD). What are the enabling technologies for a more integrated design paradigm? One is the high-fidelity mathematical/numerical representation of properties and functions of the flight vehicle that is playing a much greater role in simulation-based design. The other is the tremendous growth in computer power over the years.

Within such a framework the VP can be defined as a high-fidelity mathematical/numerical representation of the physical properties and the functions of a product. Critical to the success of the VP is the capability for rapid generation of high-fidelity information from all disciplines, which recent advances in information technologies and high-performance computer systems have now enabled. Computer power presently increases by an order of magnitude every five years, and no saturation is discernible at this time. Using the VP generates more and better knowledge about the design during the conceptual design phases, resulting in an improved final design because the

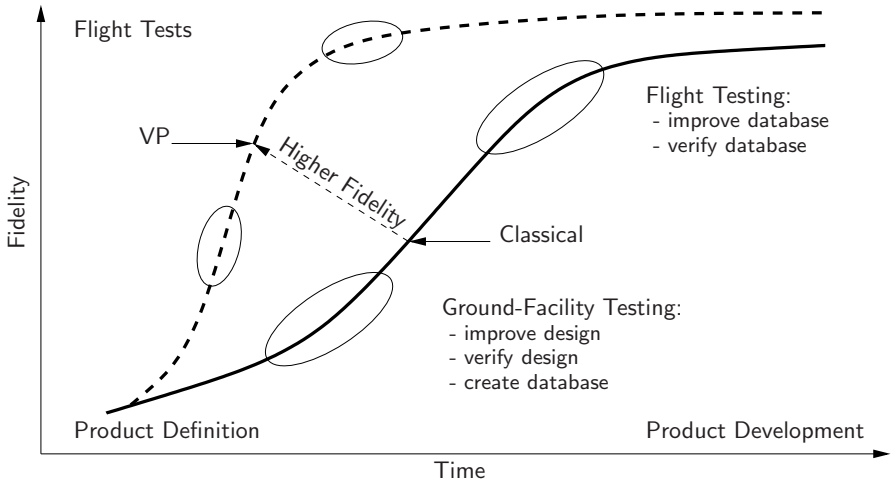

Figure 1.2: Benefits of the Virtual Product (VP) concept in today's aeronautical industry.

fidelity of the design is higher and available earlier in the cycle. As shown in Figure 1.2 doing so reduces: the number of design cycles, the development risks, the number of flight tests, the costs and time-to-market, and possible later repair solutions, among other benefits. Of course a big challenge to VP will be the implementation of the new multidisciplinary capabilities into computational simulation and increasing the fidelity of the representation in the product-definition phase. However for industry the VP is one of the few approaches with a large potential to reduce design risks, costs and time-to-market. [87]

Aeroelastic design exemplify the current frontier of aerospace vehicle multidisciplinary analysis and optimization, indicating the framework in which aerodynamics, loads, structural dynamics, weights, controls, flight mechanics and propulsion can be integrated, and where multidisciplinary interactions and trade-offs can be examined. The integration of aeroelastic phenomena into the aircraft design process is only starting now. In the past, aeroelastic repair or flight limitation were applied once the aircraft design was already completed. As an example, winglets are optimized in an aerodynamic design process. This will usually create additional structural weight penalties from a reduced flutter stability. This weight penalty requires an incremental increase of the lift coefficient, which in turn results in an increase of the induced drag, which can be higher than the gains from the winglets. If the elastic deformations of the structure are not included in the winglets design process, their effectiveness is reduced even more. An integrated design process would create winglets of different size and shape, which would improve the overall benefits from the winglets. [14]

In order for an integrated aeroelastic design process to be successful, the following functions need to be developed further: a) high-fidelity and flexible coupling procedures among sub-systems, b) efficient and robust grid generation, deformation and adaptation technologies with particular focus on how to deal with moving control surfaces and c) easy-to-use general interface to external programs such as an optimizer.

This application shows that multidisciplinary high-performance simulation and optimization in aircraft design reaches far beyond the classical aeroelastic design (and its computation topics) towards the holistic design and optimization of the controlled elastic aircraft. [3, 66, 67]

1.2.2 Computational Fluid Dynamics

The use of Computational Fluid Dynamics (CFD) for industrial aircraft design started in the 1960s, and since then has grown from a tool used to supplement wind tunnel or flight experiments to an identifiable new technology standing on its own, making important contributions to all stages of the design process of a flying machine. [87] Almost 20 years ago massive use of CFD started to find its breakthrough within the aeronautical industry. Step by step routine use extended from simplified cases up to the most complex configurations and geometrical shapes. Furthermore, flow modelling improved from inviscid flow simulation to the standard use of Reynolds Averaged Navier-Stokes (RANS) equations with one/two-equation or full Reynolds Stress Model (RSM) turbulence models. Now flow modelling is on its way to Detached Eddy Simulation (DES) and Large Eddy Simulation (LES), although not ready yet for routine use in the industrial framework. [5] Three factors were instrumental in this enormous progress: a) the progress in mathematical modelling, b) the progress in development of efficient numerical methods and c) the increase in available computer resources.

In the 1960s and early 1970s, CFD applied to aircraft design consisted only of simplified (linear) models, e.g. lifting-line and lifting-surface theories, then vortex lattice procedures and since the mid-1960s panel methods. Boundary-layer methods to study viscous effects became sufficiently mature in the early 1970s to be applicable in design. In this decade, much work was done on coupling panel methods with boundary-layer methods, and on developing non-linear compressible potential formulations to treat transonic flows with shocks. The first Euler codes for research associated with aircraft design appeared in the 1980s, applied mainly to steady aerodynamics, while panel methods were extended to handle unsteady problems. By the end of the 1980s, a further increase in computing resources became available in the form of parallel computers. Massively parallel architectures were seen as a very promising way to solve realistic flow problems in an acceptable turn-around time for industrial design. Among others, parallel simulation contributed to the move from Euler to Navier-Stokes simulations for steady flows, and the use of the unsteady Euler formulation for studying transient phenomena. At the same time concern arose for the need to integrate CFD codes into the engineering design environment in order to meet the new challenges posed by the changing forces of the economic market for aircraft. Since the mid-1990s efforts are underway to incorporate the existing body of CFD knowledge fully into methods and routines used in aircraft design. [87]

Thus numerical simulation has become a principal element in the aircraft design process because of the flexibility it provides for rapid and comparatively inexpensive evaluation of alternative designs, and because it can be integrated in a simulation environment treating concurrently both multidisciplinary analysis and optimization.

Figure 1.3: Use of CFD in aircraft development in Airbus

Typical applications of CFD, currently underway or planned in the near future are: a) design of the aircraft external shape, e.g. airfoil and wing design, nacelles and body-fairings optimization, b) evaluation of the performance and control database, e.g. stability and control derivatives together with the analysis of stability, control and handling characteristics, c) evaluation of the loads database for the structural design, d) systems integration, e.g. interference between weapons and the airframe or evaluation of the performances of the air conditioning system in the cabin and e) many more, among which aeroservoelatic analysis. A graphical survey of the typical applications of CFD within today's aeronautical industry is presented in Figure 1.3 and in Figure 1.4 for the leading aircraft manufacturing companies Airbus and Boeing. The reasons why its use is increasing despite the higher costs, is that the results obtained with it deliver an added value over the results of the standard methods.

Together with the increasing fidelity of mathematical modelling and numerical methods within the fruitful research field of Computational Fluid Dynamics (CFD), the role of the wind tunnel is currently changing: it is moving from being a design tool to becoming a tool that validates the designs obtained through the use of CFD. This shift is also favourable because it yields significant savings in terms of both time and budget for wind tunnel experimental campaigns and because it allows the engineer to go into even more detail, namely to analyze local features of the flow solution.

Figure 1.4: Use of CFD in aircraft development in Boeing

Such information is sometimes not easy to obtain from wind tunnel tests, and CFD through its three-dimensional volumetric results can significantly help to understand the flow physics at very detailed levels. For example it is worthwhile to remark the achievements of the AIAA Drag Prediction Workshop and High Lift Prediction Workshop series with the objective of providing an impartial forum for evaluating the effectiveness of existing computer codes and modelling techniques, focusing on a "blind" prediction (no experimental data available) respectively of the trimmed polar curve and high-lift configuration performance for a reference civil aircraft model. These ongoing initiatives provide a key contribution for assessing the credibility of CFD as a quantitatively reliable tool to be used in the design and qualification processes of conventional (and unconventional) aircraft.

With reference to the European framework, it is interesting to provide a quick overview of the common features of the CFD codes used within the aeronautical industry. It is convenient to subdivide the items according to the approach chosen for discretizing the domain, i.e. structured grids, unstructured grids and hybrid grids. In broad terms, approximately half of the codes are structured multi-block, another third are unstructured, and the final sixth are hybrid. However a significant amount of research is presently devoted to the unstructured category in order to possibly cut the time overhead and the expertise necessary for building a high-quality multi-block structured grid. [87]

Within the framework of a structured multi-block approach it is possible to identify the following common features: a) cell-centered Finite-Volume (FV) formulation, b) space discretization using an upwind scheme and/or a centered scheme plus artificial dissipation, b) optimized Explicit Runge-Kutta (ERK) time integration schemes, c) steady-state convergence acceleration drivers such as Implicit Residual Smoothing (IRS) and Multi-Grid (MG) and d) implicit Dual Time-Stepping (DTS) for unsteady calculations. All codes include a two-equation turbulence model, and some kind of fixed transition modelling. Finally all the codes were optimized and run on parallel computers. Other distinctive features include the use of an Arbitrary Lagrangian Eulerian (ALE) formulation for moving grids applications and the possibility of discontinous connectivity at block interfaces. Among the others it is worthwhile to describe more in detail the elsA code developed by ONERA. It is one of the few codes designed and implemented using the object-oriented programming approach, written mostly in the C^{++} programming language. Two other programming languages are considered: Fortran 90 for crunching time-consuming loops, and Python, a public domain interpreted object-oriented programming language for the user interface, including a Graphical User Interface (GUI). [12]

Within the framework of an unstructured and hybrid approaches it is possible to find more or less all the common features already cited above. It is interesting that some codes are based on a Finite-Element (FE) formulation. Among the others it is worthwhile to provide more details about the EDGE code developed by FOI. It is written in Fortran 90 programming language, using the dual-mesh approach with an edge-based formulation. It is parallelized by means of domain decomposition and a Message Passing Interface (MPI) communication layer. [23] Another important player is the TAU code developed by DLR. The use of the dual-mesh approach makes the solver independent of the element type used in the primary hybrid mesh (hexahedra, tetrahedra, prisms, etc.). It is used for the development of an aerodynamic simulation toolbox for the analysis of unsteady maneuvers and it relies on MpCCI coupling library to automatically handle the data transfer to other disciplines. Finally to allow for aeroservoelastic simulations, a dedicated mesh deformation module is included. [32]

Most of the CFD codes currently used within the aeronautical industry are written in Fortran 77/90 programming languages, without exploiting object-oriented features. Although these kinds of codes are very efficient, their inherent simple data structure makes it complicated to extend the codes to interact with other physical or numerical models since modifications on a low level may propagate changes up to the highest level of the code, thus complicating the whole endeavor, and integrating these kinds of CFD codes into a multidisciplinary simulation environment that requires interaction with other simulation tools is an almost impossible task. In the middle of the 1990s, object-oriented programming concepts started to be used within CFD. The principal advantage of object-oriented programming is that the structure of a program becomes simpler because operations are performed on an object. This facilitates code maintenance, and permits an easy extension of the code to interact with other physical models. Also, coupling of object-oriented CFD codes with codes from other disciplines seems to be easier. In summary, the software-engineering requirements of future CFD tools within the integrated environment are: a) efficient computer implementation, b) high modularity, c) easy to maintain and d) easy to couple with other codes. [87]

1.2.3 Computational Aeroservoelasticity

It can be presumed that many early aircraft suffered catastrophic structural failure due to a lack of understanding of interactions between the aerodynamic forces and the structure. As the understanding of two-dimensional unsteady aerodynamics improved with the seminal work by Theodorsen, the modelling capability of aeroservoelastic phenomena did as well. Classically by the 1950s aerodynamic strip theory was used for flutter predictions, with empirical compressibility and aspect ratio effects, combined with an assumed modes structural model. The methodology could be applied to include control surfaces and also swept wings. However, configurations such as T-tails required a more sophisticated aerodynamic analysis, and this was provided in the 1960s by unsteady panel methods such as the Doublet Lattice Method (DLM) which is embedded in Nastran, a "de-facto" standard tool for aerospace industry. This approach, combined with the structural Finite-Element (FE) method developed at a similar time, provides the fundamental tools that have been used for aeroservoelastic static and dynamic analysis for the past 40 years.

Non-linearities can be present in an aeroservoelastic system due to a number of different phenomena that occur in the structure, aerodynamics, and control systems. In fact these disciplines are the building blocks of aeroservoelasticity as graphically summarized in Figure 1.5 with Collar's triangle. [9] Structural non-linearities manifest themselves mainly as non-uniform stiffness effects and/or freeplay of control surface attachments. Some very flexible aircraft exhibit geometric stiffness non-linearities due to the large deflections that can occur in flight. Aerodynamic non-linearities occur primarily in the transonic flight regime due to the complex interaction of shock waves and structural movement (e.g. transonic flutter, aileron buzz). A further example is buffeting, occurring at large angles of attack due to massively separated flows. Finally control systems non-linearities can manifest themselves as deflection and rate limits whereby the control surfaces cannot respond as required by control laws. These non-linearities affect the aeroservoelastic behaviour in a manner that cannot be predicted using linear analysis methods.

However current industrial practice for the analysis of aeroservoelastic static and dynamic phenomena relies heavily on linear methods and this has led to overly conservative design and flight envelope restrictions for aircraft. Although such lower-fidelity methods have served the aeronautical industry well, it is clear that the adoption of higher-fidelity mathematical models and numerical methods is desirable. The research field of Computational Fluid Dynamics (CFD) has achieved enormous successes, providing progressively higher-fidelity flow modelling capabilities through Transonic Small Disturbances (TSD) and/or Non-Linear Full Potential (NLFP) equations in the 1970s, Euler equations in the 1980s, Reynolds Averaged Navier-Stokes (RANS) equations in the 1990s and more recently Detached Eddy Simulation (DES) and Large Eddy Simulation (LES). In terms of flow phenomena these models all allow the prediction of shocks, and the more advanced ones allow the prediction of massively separated flow. The exploitation of such tools for aeroservoelastic simulation is called Computational Aeroservoelasticity (CA). The increase in available and affordable computational resources means that such analysis tools are now viable for a transition from a research to an industrial environment. The major challenge faced by

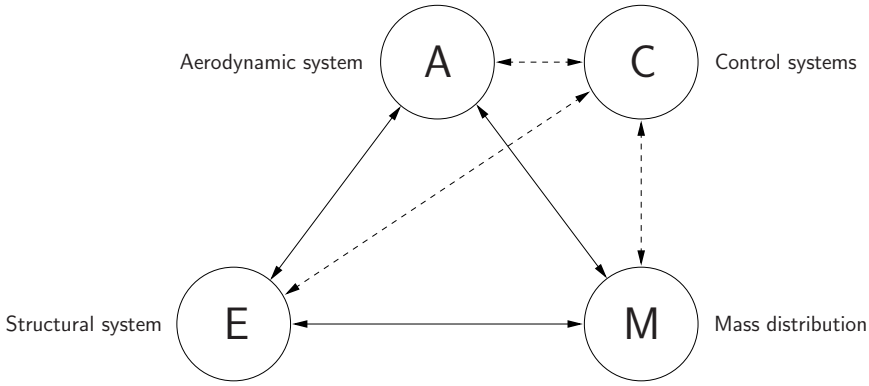

Figure 1.5: Collar's triangle.

industry in aeroservoelastic design and qualification of aircraft is the shear number of load cases that must be considered. Several thousands of cases must be considered, and for combat aircraft this number is multiplied by the number of possible store configurations. Presently CA is one or two orders of magnitude too slow for routinary use, e.g. for flutter qualification purposes. However it provides cost-effective tools for high-fidelity analysis of critical or unexpected cases at conditions identified by other means. [21] Significant successes and progresses have been achieved in recent years both for static and dynamic aeroservoelastic problems. [76] It is worthwhile to mention some examples such as the aeroservoelastic trim of a maneuvering flexible aircraft [16], the analysis of the transonic flutter of the AGARD 445.6 wing [13], the simulation of oscilatting flap configurations for the Benchmark Active Controls Technology (BACT) wing [88], the study of Limit-Cycle Oscillations (LCO) [26] and finally the use of Reduced Order Models (ROM) for active control system design. [33]

The following four considerations provide challenges to CA: a) how to sequence in time between the aerodynamic and structural models, b) how to exchange information between the aerodynamic and structural grids, c) how to deform the aerodynamic grid due to the structural movement and d) the computational cost of the unsteady CFD solution. Issue a) has been tackled satisfactorily in a number of ways and possible solutions include the use of staggered schemes without sub-iterations or the embedding of the structural solver within the aerodynamic one with little impact on the computational cost. [26, 66] Issue b) is of particular concern when the structural model is very simplified (e.g. beam-stick model) while the aerodynamic one is very detailed and the most promising solutions in terms of efficiency, robustness and flexibility rely on the use of Radial Basis Function (RBF) interpolation schemes. [17, 63] There are several approaches available for dealing with issue c): for unstructured grids a spring analogy is often used. Other possible approaches include multivariate interpolation schemes such as Inverse Distance Weighting (IDW). [78, 91] Of particular concern is the management of the grid deformation for cases involving control surface movement. Sliding grids have been used successfully and an alternative interesting option consists of blending the control surface edge into the wing. [21, 65] Finally regarding issue d) the same considerations made in §1.2.2 are valid.

The central role of numerical simulation in the integrated design environment requires short turn-around times. Today this is accomplished by using lower-fidelity more efficient methods, e.g. potential-flow methods. However, when resorting to the higher-fidelity more expensive Euler or Navier-Stokes methods, there are still some bottlenecks to overcome in order to effectively use CA tools within the VP concept. The bottleneck in automatic grid generation appears now to be broken, although not yet for aerodynamic/structure couplings involving moving or deforming surfaces that are needed for transient simulations of control surfaces movements. The turn-around time for a CFD simulation seems to be acceptable compared to the time needed for the grid generation, but if a large number of cases must be tackled (with an upper bound of several thousands of cases), it becomes clear that the time for a CFD simulation must be reduced by at least one or two orders of magnitude. Improved steady-state convergence acceleration drivers (e.g. multigrid coupled with implicit schemes) and faster, massively parallel computers are only some of the ingredients needed to meet this challenge. Finally post-processing of the computed solution is today already a time-consuming and labor-intensive task. In the future, the number of grid points in each simulation will increase, together with the number of cases taken into account. Improvements therefore in visualization tools are needed with fast data-extraction tools, feature-detection tools, and better Man-Machine Interfaces (MMI). Another important bottleneck in the application of computational-based design is to assess whether the solution meets with the desired accuracy. The ultimate goal of computational tools is to be able to certify a vehicle concept without the use of wind tunnel experiments and with only a limited amount of certification flight testing. This requires that simulation tools be able to make quantitative predictions (within some known error bounds) over the whole flight envelope of the vehicle. While it is possible to make an estimation of uncertainties related to the numerical modelling (e.g. grid convergence, time convergence), it is very difficult to estimate uncertainties in results due to the physical modelling. To this end it is worthwhile to remark the recent kick-off of the AIAA Aeroelastic Prediction Workshop series with the objective of providing an impartial forum for assessing state-of-the-art CA methods as practical tools for the prediction of static and dynamic aeroservoelastic phenomena. In fact no comprehensive aeroeservolastic benchmarking validation standard currently exists, hindering validation objectives.

1.2.4 Free software

Most of the Computational Fluid Dynamics (CFD) codes in use in the aeronautical industry are developed in close collaboration between aeronautical industry, aeronautical research establishments and universities with close links to the users in industry. Commercial codes are being used in the aeronautical industry, but rarely for external aerodynamics. There are several reasons for this. Firstly when the aeronautical industry started to use CFD in the 1970s, no commercial codes were available on the market, so in-house codes were developed. Secondly CFD codes are used in an integrated environment with a variety of other tools and therefore the source code needs to be accessible, which is rarely the case for a commercial software. Thirdly a CFD code is a very complex system, and people using it must understand how it

Figure 1.6: Logo of the Free Software Foundation (FSF) (left) and of the collaborative project GNU/Linux (right).

functions and behaves. This can only be achieved when the code-development team interacts closely with the code users. Fourthly innovation is an overriding factor in the aeronautical industry, which is easier to satisfy with in-house codes rather than with commercial ones. And finally, confidence in the computed results increases with the possibility to verify what is happening in the source code, and although it is possible to get the source code from some commercial-code vendors, this is in general not the case, and in any case would require a very close working arrangement between code vendor and industry. [87] There are significant common features between such guidelines and the concept of free software.

Free software can be defined as a program released under a particular license not only allowing, but encouraging anyone to use, study, modify and redistribute it. Contrary to a popular misconception that software is either free or commercial these are unrelated traits. One example of free commercial software is GNAT, developed and available commercially, but free software because of its non-proprietary nature, with the source code publicly available. [2] On the other hand, free and proprietary software are opposite traits, and an application can be one or the other but never both, contingent upon the availability of the source code with certain minimum freedoms.

In the 1950s and 1960s software was commonly shared by individuals who used computers and by hardware manufacturers who welcomed the fact that people were making software that made their hardware useful. Organizations of users and suppliers were formed to facilitate exchange of software. By the late 1960s the picture changed with software costs dramatically increasing and in the 1970s and early 1980s the software industry began using technical measures (e.g. only distributing binary copies of computer programs) to prevent computer users from being able to study and modify software. In 1980 copyright law was extended also to computer programs. The current idea of free software was born in 1983 when R. Stallman created the Free Software Foundation (FSF) with the target of developing a completely free operating system. With the collaborative effort of many programmers in 1991 the operating system GNU/Linux was born, a freely available, modifiable and redistributable clone of UNIX. Following the formal definition by R. Stallman a software is free if people who receive a copy of the software have the following four freedoms:

Freedom 0: freedom to run the program for any purpose,

Freedom 1: freedom to study how the program works, and change it,

Freedom 2: freedom to redistribute copies so you can help your neighbor,

Freedom 3: freedom to improve the program, and release your improvements (and modified versions) to the public, so that the whole community benefits. To this end the availability of the source code is a prerequisite.

However the word "free" does not imply that such a free software can be used indiscriminately, as it is released under a particular license designed for encouraging the collaboration among users without jeopardizing the intellectual property (e.g. the original authors or copyright holders must always be cited in all modified or redistributed versions of a computer program). A significant segment of free software is released under the GNU General Public License (GPL) [58], written by R. Stallman and E. Moglen in 1985 in order to grant users the fundamental freedoms discussed above. This so-called "copyleft" license is very strict, since it requires any modified application to be released under the same license. Alternatively other less restrictive licenses exist such as the GNU Lesser General Pubblic License (LGPL), allowing the user to mix free and proprietary software.

The economic viability of free software has been recognized by large corporations such as IBM, Red Hat, and Sun Microsystems. Many companies whose core business is not in the IT sector choose free software, due to the lower initial capital investment and ability to freely customize the application packages. Also, some non-software industries are beginning to use techniques similar to those used in free software development for their research and development process. Since free software may be freely redistributed it is generally available at little or no cost. Therefore free software business models are usually based on adding value such as applications, support, training, customization, integration, or certification. Within such a framework it is interesting to draw a quick comparison between a commercial black-box tool and a customized tool based on free software. In the first case everyone gets the same package with no possible strategic advantage over competitors, while in the second case it is possible due to the availability of the source code to fit the software to the specific needs of the user. Moreover as the software is continuously under the investigation of a significant user community, the process of bug fixing, update and optimization of the program are definitely faster. However it is undeniable that free tools yield some limitations with respect to proprietary ones, e.g. the documentation of a commercial product is in general superior.

1.3 Overview of the thesis

After providing an overview of the background and the motivation for designing and implementing a high-fidelity multidisciplinary analysis toolbox of free software to tackle real-world aeroservoelastic problems, the outline of the present work is now surveyed. More in particular the following Chapters are dedicated to remarkable and/or original features within the block diagram of Figure 1.1, namely:

Chapter 2

This Chapter is aimed at providing a theoretical background for the aeroservoelastic modelling of a free-flying deformable aircraft. Despite its intrinsically multidisciplinary nature, it is convenient to study separately the structural and aerodynamic problems, relying on the aeroelastic interface for realizing the closed-loop connection between the sub-systems. In §2.1 the mathematical modelling of the structural sub-system is discussed, focusing on how to choose a convenient reference frame for dealing with a free deformable body. In §2.2 the hierarchy of possible mathematical models of the aerodynamic problem in the transonic regime is surveyed, with the target of striking the best balance between fidelity and costs. The closed-loop interaction between structural and aerodynamic sub-system, suitably linked by means of the aeroelastic interface strategy described in §2.3, is the core of the aeroservoelastic system presented in §2.4, focusing on both static (e.g. non-linear trim of maneuvering flexible aircraft) and dynamic (e.g. flutter) problems.

Chapter 3

This Chapter provides an overview of the background for dynamic mesh handling within the framework of OpenFOAM software and then illustrates the motivation for designing and implementing a novel mesh deformation strategy, particularly suited for the aeroservoelastic analysis of free-flying deformable aircraft. More in particular in §3.1 some challenging applications closely related to mesh deformation are surveyed, together with the tools already available within the framework of OpenFOAM software to tackle such problems. Particular focus is dedicated to the Geometric Conservation Law (GCL) which can be interpreted as a link between mathematical models and numerical methods (and therefore programming tools). Successively in §3.2 a novel mesh deformation strategy is presented, stressing the hierarchical nature of the algorithm and the advantages when dealing with the aeroservoelastic analysis of free-flying deformable aircraft. The serial and parallel performances are compared to those of more classical mesh deformation options. Finally in §3.3 the robustness of the algorithm and the quality of the results are benchmarked by tackling a series of test problems of increasing complexity.

Chapter 4

This Chapter is aimed at assessing the credibility of the proposed aeroservoelastic analysis toolbox by tackling a set of static aeroservoelastic problems and comparing the results with reference experimental and numerical data available in literature. In §4.1 the static aeroelastic benchmark test problem of computing the reference equilibrium or "trim" configuration of the HiReNASD wing is presented. Such an example is of particular interest because it was selected as a benchmark test problem for the AIAA Aeroelastic Prediction Workshop series with the objective of providing an impartial forum for assessing state-of-the-art CA methods as practical tools for the prediction of static and dynamic aeroservoelastic phenomena within the transonic regime. More precisely, after providing an overview of the structural and aerodynamic models, we compute the static aeroelastic response of the wing in attached axes by

means of the iterative method and compare the results with reference experimental data. Such a procedure is repeated for different angles of attack $\alpha \in (-1.5°, 4.5°)$ in order to highlight the non-linear phenomena associated with the transonic regime. In §4.2 we present the numerical results for the non-linear aeroservoelastic trim of a free-flying A320 aircraft equipped with innovative passive aeroelastic wing tip devices. More precisely, after providing an overview of the structural and aerodynamic models, we compute the trim parameters and the static aeroelastic response of the aircraft for different configurations and maneuvers and compare the results with those of Nastran, a "de-facto" standard tool within the aeronautical industry, in order to highlight the differences between lower and higher fidelity tools in the transonic regime.

Chapter 5

This Chapter is aimed at assessing the credibility of the proposed aeroservoelastic analysis toolbox by tackling a set of dynamic aeroservoelastic problems and comparing the results with reference experimental and numerical data available in literature. In §5.1 the classical dynamic aeroelastic benchmark test problem of computing the transonic flutter boundary of the AGARD 445.6 wing is presented. More precisely, after providing an overview of the structural and aerodynamic models, we compute the reference equilibrium or "trim" configuration for the (numerical) linearization of the generalized aerodynamic forces. Successively we build the aerodynamic transfer functions matrix and we choose a root-tracking non-linear method for computing the so-called $V_\infty - \omega$ and $V_\infty - g$ diagrams. Such a procedure is repeated for different Mach numbers $M_\infty \in (0.678, 1.140)$ in order to cover the whole transonic regime. In §5.2 we illustrate an example aeroservoelastic problem of how to design a flutter suppression active control system to operate within the highly non-linear transonic regime with a linear, low-fidelity but efficient model and then verify the performances with a non-linear, high-fidelity but expensive model. This strategy yields a significant added value to the workflow since it makes possible to appreciate how important the neglected non-linear effects actually are and therefore the robustness of the designed active control system. More precisely we design a simple Proportional-Integral (PI) active control system by means of a multi-objective optimization strategy based on Genetic Algorithms (GA). Successively we compare the results of a post-flutter direct simulation with control system on and off with both the low and high-fidelity tools.

2

Aeroservoelastic modelling of free-flying deformable aircraft

This Chapter is aimed at providing a theoretical background for the aeroservoelastic modelling of a free-flying deformable aircraft. Despite its intrinsically multidisciplinary nature, it is convenient to study separately the structural and aerodynamic problems, relying on the aeroelastic interface for realizing the closed-loop connection between the sub-systems. In §2.1 the mathematical modelling of the structural sub-system is discussed, focusing on how to choose a convenient reference frame for dealing with a free deformable body. In §2.2 the hierarchy of possible mathematical models of the aerodynamic problem in the transonic regime is surveyed, with the target of striking the best balance between fidelity and costs. The closed-loop interaction between structural and aerodynamic sub-system, suitably linked by means of the aeroelastic interface strategy described in §2.3, is the core of the aeroservoelastic system presented in §2.4, focusing on both static (e.g. non-linear trim of maneuvering flexible aircraft) and dynamic (e.g. flutter) problems.

2.1 Structural sub-system

The structural sub-system can be schematized as shown in Figure 2.1 as a block which receives in input the material properties (e.g. density ρ, Young's modulus E, Poisson's ratio ν) together with the aerodynamic forces suitably interpolated on the structural d.o.f. $\{\boldsymbol{F}_s^a(t)\}$ and returns in output the structural displacements and velocities $\{\dot{\boldsymbol{u}}_s(t)\}$ and $\{\boldsymbol{u}_s(t)\}$. A difficulty when dealing with maneuvering flexible aircraft lies in the contemporary presence of rigid and deformable motions. Moreover the d.o.f. associated with the control surfaces can be treated as additional rigid motions, depending on whether they participate significantly to the deformability of the structure. [56, 89]

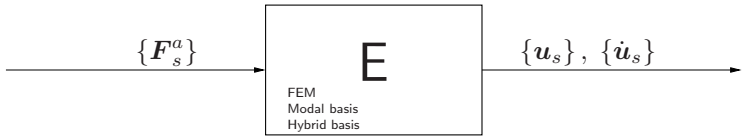

Figure 2.1: Block diagram for the structural sub-system.

2.1.1 Dynamics of a free deformable body

The equations governing the dynamics of a free deformable body can be determined using an energetic principle such as the Principle of Virtual Work (PVW). It states that the necessary and sufficient condition for the static and/or dynamic equilibrium of a free deformable body is that the virtual work made by the elastic, inertial and external (surface and volume) forces, for the corresponding virtual displacements, namely infinitesimal, arbitrary, smooth and in harmony with the given kinematic constraints, must be zero. Of course the equations governing the dynamics of a free rigid body can be derived as a special case. In the general case it is possible to write:

$$\oint_{\mathcal{S}} \delta\boldsymbol{u}^{\mathsf{T}}\boldsymbol{f}\,\mathrm{d}\mathcal{S} + \int_{\mathcal{V}} \delta\boldsymbol{u}^{\mathsf{T}}\boldsymbol{g}\,\mathrm{d}\mathcal{V} - \int_{\mathcal{V}} \delta\boldsymbol{u}^{\mathsf{T}}\rho\boldsymbol{a}\,\mathrm{d}\mathcal{V} - \int_{\mathcal{V}} \delta\boldsymbol{\varepsilon}^{\mathsf{T}}\boldsymbol{\sigma}\,\mathrm{d}\mathcal{V} = 0, \tag{2.1}$$

where $\mathcal{V} \subseteq \mathbb{R}^{N_d}$ is the spatial domain of the problem with boundary $\mathcal{S} = \partial\mathcal{V} \subseteq \mathbb{R}^{N_d-1}$. The external surface $\boldsymbol{f}(\boldsymbol{x},t)$ and volume $\boldsymbol{g}(\boldsymbol{x},t)$ forces together with the inertial forces $\rho(\boldsymbol{x},t)\,\boldsymbol{a}(\boldsymbol{x},t)$ are projected (by means of the transpose operator) onto the virtual increment of the structural displacements $\boldsymbol{u}(\boldsymbol{x},t)$. Similarly for the six independent components of the symmetric Piola-Kirchhoff stress tensor $\boldsymbol{\sigma}(\boldsymbol{x},t)$, to be projected onto the virtual increment of the array of the six independent components of the symmetric Green-Lagrange deformation tensor $\boldsymbol{\varepsilon}(\boldsymbol{x},t)$.

First of all it is necessary to provide a suitable description of the kinematics of a free deformable body. The main idea consists in representing the motion of a free deformable unconstrained body as the sum of the following contributions: a) the motion of a floating reference frame $\mathcal{B}$, with origin in P and orientation unit vectors $(\widehat{\boldsymbol{b}}_1, \widehat{\boldsymbol{b}}_2, \widehat{\boldsymbol{b}}_3)$, with respect to the inertial reference frame $\mathcal{I}$, with origin in O and orientation unit vectors $(\widehat{\boldsymbol{i}}_1, \widehat{\boldsymbol{i}}_2, \widehat{\boldsymbol{i}}_3)$, accounting for the "large" motion of the body and generally-speaking connected with the flight mechanics of the rigid aircraft and b) the relative motion with respect to the floating reference frame $\mathcal{B}$, accounting for the "small" displacements of the body and generally-speaking connected with elasticity. Such a floating reference frame $\mathcal{B}$ is not necessarily fixed to the body. This is one of the main differences with the rigid case. Within such a framework the structural displacements $\boldsymbol{u}(\boldsymbol{x},t)$ can be written in the inertial reference frame $\mathcal{I}$ as follows:

$$\boldsymbol{u} = \boldsymbol{x}_P + \mathbf{R}\,(\boldsymbol{r} + \boldsymbol{s}), \tag{2.2}$$

where $\boldsymbol{x}_P(t)$ identifies the position of the origin of the floating reference frame in the inertial reference frame, $\mathbf{R}(t)$ is the orthogonal tensor representing the rotation transformation from the floating reference frame to the inertial one and finally $\boldsymbol{r}$ and

$\boldsymbol{s}(t)$ correspond to the undeformed position and relative motion respectively within the floating reference frame. The linear operator $\mathbf{R}(t)$ can be written in a number of ways depending on the particular choice of how to express the orientation of the floating reference frame relative to the inertial one. For instance it is possible to resort to the Euler-Rodriguez formula and write:

$$\mathbf{R} = \mathbf{I} + \sin\varphi\,\mathbf{K}_\times + (1-\cos\varphi)\,\mathbf{K}_\times\mathbf{K}_\times \tag{2.3}$$

where $\varphi(t)$ and $\widehat{\boldsymbol{k}}(t)$ are the magnitude and direction of the rotation vector $\boldsymbol{\psi} = \varphi\,\widehat{\boldsymbol{k}}$, while $\mathbf{K}_\times$ is the emisymmetric tensor representing the cross-product operator $\widehat{\boldsymbol{k}}\times$. It is worthwhile to stress that such a formulation does not necessarily lead to a separation of rigid and deformable motions. This depends on how the floating reference frame is defined. However it is possible to identify a subset of generally-speaking rigid coordinates, namely: $\boldsymbol{q}_R = \{\boldsymbol{x}_P,\, \boldsymbol{\psi}\}$. Finally the virtual increment of the structural displacements $\delta\boldsymbol{u}(\boldsymbol{x},t)$ can be written in the inertial reference frame $\mathcal{I}$ as follows:

$$\begin{aligned}
\delta\boldsymbol{u} &= \delta\boldsymbol{x}_P + \delta\boldsymbol{\psi}\times(\boldsymbol{r}+\boldsymbol{s}) + \delta\boldsymbol{s} \\
&\simeq \begin{bmatrix} \mathbf{I} & -\boldsymbol{r}\times \end{bmatrix} \begin{Bmatrix} \delta\boldsymbol{x}_P \\ \delta\boldsymbol{\psi} \end{Bmatrix} + \delta\boldsymbol{s} + \mathcal{O}(\boldsymbol{s}^2) \\
&= [\,\boldsymbol{N}_R(\boldsymbol{x})\,]\,\{\delta\boldsymbol{q}_R(t)\} + \delta\boldsymbol{s}(\boldsymbol{x},t) + \mathcal{O}(\boldsymbol{s}^2),
\end{aligned} \tag{2.4}$$

where the motion of the floating reference frame is written as the product of the matrix of rigid shape functions $[\,\boldsymbol{N}_R(\boldsymbol{x})\,]$ and the array of rigid coordinates $\{\boldsymbol{q}_R(t)\}$. Such a formalism is useful for including additional rigid d.o.f. associated e.g. with control surfaces by adding a column to the matrix of rigid shape functions with the cross product between the distance from the hinge line and the direction of the rotation vector and by padding the array of the rigid coordinates with the control surface deflection.

In order to make explicit the virtual work contribution of the inertia forces, it is necessary to derive twice Eq. (2.2) for the velocity $\boldsymbol{v}(\boldsymbol{x},t)$ and acceleration $\boldsymbol{a}(\boldsymbol{x},t)$ respectively. For flight mechanics applications the choice of a body reference frame is preferable. Therefore the velocity $\boldsymbol{v}(\boldsymbol{x},t)$ and acceleration $\boldsymbol{a}(\boldsymbol{x},t)$ can be written in the floating reference frame $\mathcal{B}$ as follows:

$$\begin{aligned}
\boldsymbol{v} &= \left.\frac{\mathrm{d}\boldsymbol{u}}{\mathrm{d}t}\right|_{\mathcal{B}} = \dot{\boldsymbol{x}}_P + \boldsymbol{\omega}\times(\boldsymbol{r}+\boldsymbol{s}) + \dot{\boldsymbol{s}} \\
\boldsymbol{a} &= \left.\frac{\mathrm{d}\boldsymbol{v}}{\mathrm{d}t}\right|_{\mathcal{B}} = \dot{\boldsymbol{v}}_P + \boldsymbol{\omega}\times\boldsymbol{v}_P + \dot{\boldsymbol{\omega}}\times(\boldsymbol{r}+\boldsymbol{s}) + \boldsymbol{\omega}\times\boldsymbol{\omega}\times(\boldsymbol{r}+\boldsymbol{s}) + 2\boldsymbol{\omega}\times\dot{\boldsymbol{s}} + \ddot{\boldsymbol{s}},
\end{aligned} \tag{2.5}$$

where the linear $\boldsymbol{v}_P(t)$ and angular $\boldsymbol{\omega}(t)$ velocities in the floating reference frame are related to the rigid coordinates by means of the following non-linear kinematics conditions: $\dot{\boldsymbol{\psi}} = \mathbf{S}^{-1}\,\boldsymbol{\omega}$ and $\dot{\boldsymbol{x}}_P = \mathbf{R}\,\boldsymbol{v}_P$. Finally the linear operator $\mathbf{S}(t)$ can written similarly to Eq. (2.3) as follows:

$$\mathbf{S} = \mathbf{I} + \frac{1-\cos\varphi}{\varphi}\,\mathbf{K}_\times + \frac{\varphi-\sin\varphi}{\varphi}\,\mathbf{K}_\times\mathbf{K}_\times \tag{2.6}$$

However it is important to note that such a description of rotations based on the rotation vector has only a finite range of validity: $-2\pi < \varphi < 2\pi$. This is easily verified observing that the determinant $\det \mathbf{S} = 2\,(1 - \cos\varphi)/\varphi^2$ is equal to zero for $\varphi = 2k\pi$ with $k = (1,\, \infty)$.

In order to make explicit the virtual work contribution of the elastic forces, it is necessary to define the constitutive law of the material. The stress tensor $\boldsymbol{\sigma}(\boldsymbol{x}, t)$ can be related to the deformation tensor $\boldsymbol{\varepsilon}(\boldsymbol{x}, t)$ by means of a linear visco-elastic constitutive law. The material, modelled as micromechanical system, returns in output the stress tensor $\boldsymbol{\sigma}(\boldsymbol{x}, t)$ computed as the convolution integral of the impulse response matrix of the material $\mathbf{D}(t)$ and the deformation tensor $\boldsymbol{\varepsilon}(\boldsymbol{x}, t)$ in input:

$$\boldsymbol{\sigma}(\boldsymbol{x}, t) = \int_0^\infty \mathbf{D}(t - \tau)\, \boldsymbol{\varepsilon}(\boldsymbol{x}, \tau)\, \mathrm{d}\tau. \tag{2.7}$$

The choice of the Green-Lagrange tensor to measure the structural deformations guarantees that such a constitutive law is objective, i.e. independent of rigid coordinates. Experimentally the response of the material is much more rapid than the dynamic deformations of the structure within the low frequency range of interest: therefore it is possible to resort to a first order dynamical residualization of the linear visco-elastic constitutive law of Eq. (2.7) with the following quasi-steady approximation:

$$\boldsymbol{\sigma}(\boldsymbol{x}, t) = \mathbf{D}_0\, \boldsymbol{\varepsilon}(\boldsymbol{x}, t) + \mathbf{D}_1\, \dot{\boldsymbol{\varepsilon}}(\boldsymbol{x}, t) \tag{2.8}$$

Remembering that the deformation tensor $\boldsymbol{\varepsilon}(\boldsymbol{x}, t)$ can be written as a function of the structural displacements $\boldsymbol{u}(\boldsymbol{x}, t)$ by means of a suitable derivation operator $\mathscr{D}$, it is now possible to substitute Eq. (2.8) in Eq. (2.1) and rewrite the Principle of Virtual Work as follows:

$$\begin{aligned} \int_{\mathcal{V}} \delta\boldsymbol{u}^{\mathsf{T}} \rho \boldsymbol{a}\, \mathrm{d}\mathcal{V} + \int_{\mathcal{V}} \delta\boldsymbol{u}^{\mathsf{T}} \mathscr{D}^{\mathsf{T}} \mathbf{D}_1\, \mathscr{D}\, \dot{\boldsymbol{u}}\, \mathrm{d}\mathcal{V} + \int_{\mathcal{V}} \delta\boldsymbol{u}^{\mathsf{T}} \mathscr{D}^{\mathsf{T}} \mathbf{D}_0\, \mathscr{D}\, \boldsymbol{u}\, \mathrm{d}\mathcal{V} \\ = \oint_{\mathcal{S}} \delta\boldsymbol{u}^{\mathsf{T}} \boldsymbol{f}\, \mathrm{d}\mathcal{S} + \int_{\mathcal{V}} \delta\boldsymbol{u}^{\mathsf{T}} \boldsymbol{g}\, \mathrm{d}\mathcal{V} \end{aligned} \tag{2.9}$$

The choice of a linear visco-elastic constitutive law yields a linear damping term. However such a simplified model does not provide a high-fidelity representation of the real dynamics of the structural damping which is dominated by non-linear local phenomena, such as the Coulombian dissipation due to friction within joints. As a consequence it is preferable to suitably tune the damping contribution on the basis of experimental data in order to match the real average dissipation.

2.1.2 Mathematical modelling of the structural sub-system

Because of the arbitrariness of the virtual increment of the structural displacements, it is possible to restate Eq. (2.9) from variational to strong form as a system of hybrid equations. The equations governing the rigid body dynamics are Ordinary Differential Equations (ODE), while those connected with generally-speaking elastic coordinates are Partial Differential Equations (PDE). The solution of such a problem is not straightforward, especially when complex cases are considered. [55]

In order to numerically solve the structural problem it is possible to apply the Ritz method, consisting in approximating the unknown structural displacements $\boldsymbol{u}(\boldsymbol{x},t)$ with the technique of separation of variables as the product of a complete basis of suitable shape functions $[\,\boldsymbol{N}(\boldsymbol{x})\,]$, only space-dependent and satisfying a-priori Dirichlet boundary conditions and a set of only time-dependent generalized coordinates $\{\boldsymbol{q}(t)\}$:

$$\boldsymbol{u}(\boldsymbol{x},t) \simeq \sum_{k=1}^{N_s} \boldsymbol{N}_k(\boldsymbol{x})\,\boldsymbol{q}_k(t) = [\,\boldsymbol{N}(\boldsymbol{x})\,]\,\{\boldsymbol{q}(t)\}. \tag{2.10}$$

At the same time it is easy to show integrating by parts the structural problem written in variational form of Eq. (2.9) that the Neumann boundary conditions are automatically satisfied. The complete basis of suitable shape functions must now be specified and truncated to a finite number of structural d.o.f. N_s, chosen as a function of the desired level of accuracy and the convergence properties of the shape functions. More in particular it is possible to list the following strategies:

a) First of all it is possible to choose as shape functions the Lagrangian polynomial basis functions of order p with compact support of the Finite Element (FE) method. In this case the generalized coordinates of the problem correspond to the absolute nodal displacements. However the number of structural d.o.f. necessary to match the desired level of accuracy of the numerical solution is generally very high.

b) Especially in the early design stages when the size and therefore the cost of the structural model is important (e.g. the availability of an efficient model is almost mandatory for the design of active control systems), as an alternative it is possible to choose as shape functions the vibration modes of the structure. The choice of such global shape functions yields a condensed, reduced order model capable of representing accurately the numerical solution with relatively few terms of the complete set of basis functions. In fact, assuming that the external surface and volume forces are suitably smooth, it is possible to prove that vibration modes are a very efficient basis. Moreover the resulting generalized mass and stiffness matrices are diagonal and the same argument is valid for the generalized damping matrix if a proportional model, energetically equivalent to the real (non-linear) dynamics of the structural damping is employed. Another advantage of the choice of a modal basis is the possibility of adding or removing easily the rigid modes associated to the control surfaces. Finally it is possible to validate and tune the structural model benchmarking it with the experimental data of Ground Vibration Tests (GVT).

c) However the convergence properties of a modal basis deteriorate very rapidly in the case of concentrated loads, unless the so-called "inertia relief" method is applied. It is then preferable to broaden the modal basis by adding suitable static deformation global modes. As a consequence of the choice of such a hybrid base, the generalized mass, (proportional) damping and stiffness matrices are not diagonal anymore. However this penalty is not too severe as the key advantage of a modal basis is the reduced size of the resulting structural model and not the resulting possibly diagonal sparsity pattern.

Within such a framework the terms "attached axes" and "mean axes" refer to possible strategies for approximating the motion of a free deformable structure by separating its overall motion into a rigid and a deformable part. Both can be viewed as special cases of the more general concept of Tisserand reference frame and differ only in the representation of generalized external forces and inertia forces, i.e. the mass matrix, without any differences in the internal forces, i.e. the stiffness and damping matrices. For arbitrarily large motions mean axes can produce only a very limited decoupling of the inertia forces associated to the motion of the floating reference frame and those associated to deformable motion only. As a consequence the adoption of mean axes is often criticized. However such criticism is undue when dealing with small displacements of a free structure around a steady straight trajectory, where mean axes yield a significant simplification by fully decoupling inertia forces related to the floating reference frame from deformable motion, in such a way that the equations governing the dynamics of the floating reference frame are the same as those of the related rigid body. [54] Highlighting the subsets of generally-speaking rigid and deformable d.o.f. it is now possible to write the unknown structural displacements $\boldsymbol{u}(\boldsymbol{x},t)$ with the technique of separation of variables as follows:

$$\begin{aligned} \boldsymbol{u}(\boldsymbol{x},t) &= \boldsymbol{x}_P(t) + \mathbf{R}(t)\,[\,\boldsymbol{r} + \boldsymbol{s}(\boldsymbol{x},t)\,] \\ &\simeq \boldsymbol{x}_P(t) - \boldsymbol{r}\times\boldsymbol{\psi}(t) + \boldsymbol{s}(\boldsymbol{x},t) + \mathcal{O}(\boldsymbol{s}^2) \\ &\simeq \left[\begin{array}{cc} \boldsymbol{N}_R(\boldsymbol{x}) & \boldsymbol{N}_D(\boldsymbol{x}) \end{array}\right] \left\{\begin{array}{c} \boldsymbol{q}_R(t) \\ \boldsymbol{q}_D(t) \end{array}\right\}. \end{aligned} \tag{2.11}$$

It is worthwhile to remark that such a partitioning of rigid and deformable d.o.f. does not necessarily imply a description of the deformable motion in terms of the relative displacements within the floating reference frame. Absolute coordinates are also suitable to achieve such a partitioning and the two approaches are identical in the case of small displacements. For instance Finite Element (FE) models differ from their attached and/or mean axes counterparts because the overall motion is described as a function of the absolute nodal displacements within the inertial reference frame. Of course FE models can be easily translated into attached/mean axes ones, albeit at the expense of loosing some, in the case of attached axes, or all, in the case of mean axes, of the sparsity of the resulting system of equations. Therefore attached/mean axes are more suitable when a spatial approximation based on shape functions with global instead than with local support is chosen. In other terms attached/mean axes are a promising option for condensed models, when selected vibration and/or static deformation modes are chosen to build an efficient hybrid base. [70]

To begin with, let us choose attached axes, requiring that the deformable shape functions $[\,\boldsymbol{N}_D(\boldsymbol{x})\,]$ do not contain any rigid body motion. Such a constraint is not strictly needed, as long as the shape functions are independent items of a complete set. Nonetheless we prefer to resort to statically determinate shape functions, from which it follows their qualification as "attached". This implies that the relative displacements within the floating reference frame are identically zero for some points of the structural domain. However such points are not necessarily "attached" to the body.

Substituting Eq. (2.11) in Eq. (2.9) and carrying out all the computations, it is convenient to observe that the array of the generalized displacements, velocities and accelerations $\{\boldsymbol{q}(t)\}$, $\{\dot{\boldsymbol{q}}(t)\}$ and $\{\ddot{\boldsymbol{q}}(t)\}$ are independent by the space variable $\boldsymbol{x}$ and therefore can be taken outside the integral operator. Exploiting the arbitrariness of the virtual increment of the generalized coordinates $\{\delta\boldsymbol{q}\}^{\mathsf{T}}$ it is possible to write the following system of Ordinary Differential Equations (ODE):

$$[\,\mathbf{M}\,]\{\ddot{\boldsymbol{q}}\} + [\,\mathbf{C}\,]\{\dot{\boldsymbol{q}}\} + [\,\mathbf{K}\,]\{\boldsymbol{q}\} = \{\boldsymbol{Q}\}, \tag{2.12}$$

where $[\,\mathbf{M}\,]$, $[\,\mathbf{C}\,]$ and $[\,\mathbf{K}\,] \in \mathbb{R}^{N_s \times N_s}$ with $N_s = N_R + N_D$ are respectively the mass, damping and stiffness matrices, while $\{\boldsymbol{Q}(t)\}$ is the corresponding array of generalized forces, namely:

$$\begin{aligned}
[\,\mathbf{M}\,] &= \begin{bmatrix} \displaystyle\int_{\mathcal{V}} [\,\boldsymbol{N}_R\,]^{\mathsf{T}} \rho\, [\,\boldsymbol{N}_R\,]\, \mathrm{d}\mathcal{V} & \displaystyle\int_{\mathcal{V}} [\,\boldsymbol{N}_R\,]^{\mathsf{T}} \rho\, [\,\boldsymbol{N}_D\,]\, \mathrm{d}\mathcal{V} \\ \displaystyle\int_{\mathcal{V}} [\,\boldsymbol{N}_D\,]^{\mathsf{T}} \rho\, [\,\boldsymbol{N}_R\,]\, \mathrm{d}\mathcal{V} & \displaystyle\int_{\mathcal{V}} [\,\boldsymbol{N}_D\,]^{\mathsf{T}} \rho\, [\,\boldsymbol{N}_D\,]\, \mathrm{d}\mathcal{V} \end{bmatrix} = \begin{bmatrix} \mathbf{M}_{RR} & \mathbf{M}_{RD} \\ \mathbf{M}_{DR} & \mathbf{M}_{DD} \end{bmatrix} \\
[\,\mathbf{C}\,] &= \begin{bmatrix} 0 & 0 \\ 0 & \displaystyle\int_{\mathcal{V}} [\,\boldsymbol{N}_D\,]^{\mathsf{T}} \mathscr{D}^{\mathsf{T}} \mathbf{D}_1 \mathscr{D}\, [\,\boldsymbol{N}_D\,]\, \mathrm{d}\mathcal{V} \end{bmatrix} = \begin{bmatrix} 0 & 0 \\ 0 & \mathbf{C}_{DD} \end{bmatrix} \\
[\,\mathbf{K}\,] &= \begin{bmatrix} 0 & 0 \\ 0 & \displaystyle\int_{\mathcal{V}} [\,\boldsymbol{N}_D\,]^{\mathsf{T}} \mathscr{D}^{\mathsf{T}} \mathbf{D}_0 \mathscr{D}\, [\,\boldsymbol{N}_D\,]\, \mathrm{d}\mathcal{V} \end{bmatrix} = \begin{bmatrix} 0 & 0 \\ 0 & \mathbf{K}_{DD} \end{bmatrix} \\
\{\boldsymbol{Q}\} &= \begin{Bmatrix} \displaystyle\oint_{\mathcal{S}} [\,\boldsymbol{N}_R\,]^{\mathsf{T}} \boldsymbol{f}\, \mathrm{d}\mathcal{S} + \int_{\mathcal{V}} [\,\boldsymbol{N}_R\,]^{\mathsf{T}} \boldsymbol{g}\, \mathrm{d}\mathcal{V} \\ \displaystyle\oint_{\mathcal{S}} [\,\boldsymbol{N}_D\,]^{\mathsf{T}} \boldsymbol{f}\, \mathrm{d}\mathcal{S} + \int_{\mathcal{V}} [\,\boldsymbol{N}_D\,]^{\mathsf{T}} \boldsymbol{g}\, \mathrm{d}\mathcal{V} \end{Bmatrix} = \begin{Bmatrix} \boldsymbol{Q}_R \\ \boldsymbol{Q}_D \end{Bmatrix},
\end{aligned} \tag{2.13}$$

From the expression of $\mathbf{M}_{RR}$ we can see that by representing rigid motions with three pure translations and rotations we have the usual mass matrix layout of a rigid body of mass m, with an emisymmetric static unbalance matrix $\mathbf{S}$, being zero when the origin of the floating reference frame $\boldsymbol{x}_P$ corresponds to the center of mass of the body, and with a symmetric moment of inertia matrix $\mathbf{J}$, being diagonal when the orientation of the floating reference frame $(\widehat{\boldsymbol{b}}_1, \widehat{\boldsymbol{b}}_2, \widehat{\boldsymbol{b}}_3)$ is principal, namely:

$$[\,\mathbf{M}_{RR}\,] = \begin{bmatrix} \lceil m \rfloor & \mathbf{S} \\ \mathbf{S}^{\mathsf{T}} & \mathbf{J} \end{bmatrix}. \tag{2.14}$$

It is remarkable that such a numerical model is formally identical to the case of rigid body, apart from the explicit coupling with the deformable coordinates of course. Simplifications are applied only for the equations governing the rotational dynamics, with second order terms related to deformable motion neglected.

Together with the non-linear kinematic conditions: $\dot{\boldsymbol{\psi}} = \mathbf{S}^{-1}\,\boldsymbol{\omega}$ and $\dot{\boldsymbol{x}}_P = \mathbf{R}\,\boldsymbol{v}_P$ it is straightforward to restate Eq. (2.12) in state-space form as an Initial Value Problem (IVP) and solve it numerically by means of the classical explicit or implicit numerical methods. [64] Viceversa the problem becomes a little bit more involved if a set of n interacting deformable bodies is taken into account, with a set of m additional non-linear kinematic constraints in the form: $\boldsymbol{\varphi}(\{\boldsymbol{q}\}, t) = 0$. Such conditions, modelling the interaction among the deformable bodies, can be included within Eq. (2.12) by means of the technique of Lagrange multipliers as follows:

$$[\,\mathbf{M}\,]\{\ddot{\boldsymbol{q}}\} + [\,\mathbf{C}\,]\{\dot{\boldsymbol{q}}\} + [\,\mathbf{K}\,]\{\boldsymbol{q}\} = \{\boldsymbol{Q}\} - [\,\nabla\boldsymbol{\varphi}\,]^{\mathsf{T}}\{\boldsymbol{\lambda}\}, \tag{2.15}$$

where $[\,\nabla\boldsymbol{\varphi}\,] \in \mathbb{R}^{m\times nN_s}$ is the Jacobian matrix of the constraints with respect to the generalized coordinates of the entire system. Clearly the problem becomes a system of Differential Algebraic Equations (DAE) and more sophisticated numerical methods are needed to successfully tackle it. [57]

2.1.3 Floating reference frames in aeroservoelasticity

Floating reference frames are widely used in flight mechanics for the analysis of free rigid aircraft and for the multibody simulation of the dynamics of free deformable interacting bodies. In order to completely identify the behaviour of a floating reference frame, suitable reference conditions or constraints equations must be specified, e.g. in terms of its origin and orientation. In doing so, the possibility is that some choices may lead to significant advantages in the formulation of the problem, i.e. a reference frame may be built which follows the motion of the deformable body in an "optimal" manner (where optimal conditions are stated by the analyst). For instance, if a fixed inertial reference frame is chosen to describe the motion of a free-flying deformable aircraft, the structural displacements are going to grow large even if deformability is not significant, because of the rigid body translation/rotation motion. The numerical simulation of such a system would require more than a classical first-order analysis. Hence the idea of using a floating reference frame which generally-speaking moves or better floats with the body in such a way that the measured relative displacements are small. The Tisserand and the mean axes reference frames provide such a simplification, minimizing the kinetic and deformation energy within the floating reference frame respectively. Such a property is beneficial when performing multi-fidelity aeroservoelastic analyses, e.g. by significantly reducing the computational overhead associated with mesh deformation and/or by allowing the adoption of the so-called "transpiration" boundary conditions to simulate the body motion without actually deforming the computational grid. [89]

Several choices are available in order to specify such a floating reference frame. For example, its origin can be constrained to lay in the instantaneous center of gravity and its orientation to be parallel to the instantaneous principal axes of the deformable body. An alternative widely used strategy to define a convenient floating reference frame for the analysis of free deformable vehicles is the mean axes approach. The primary motivation lies in the significant simplification of the equations governing the dynamics of the vehicle as mean axes yield a (first-order) inertial decoupling between rigid and deformable d.o.f., which nevertheless remain coupled due to external forces.

Within the more general framework of Tisserand reference frame, it is convenient to resort again to Eq. (2.5) and rewrite the local and instantaneous velocity $\boldsymbol{v}(\boldsymbol{x},t)$ in the floating reference frame $\mathcal{B}$ as the sum of the following rigid translation/rotation and deformable relative contributions:

$$\boldsymbol{v} = \boldsymbol{v}_R + \boldsymbol{v}_D = \boldsymbol{v}_B + \boldsymbol{\omega}_B \times (\boldsymbol{r} + \boldsymbol{s}) + \boldsymbol{v}_D, \tag{2.16}$$

where $\boldsymbol{v}_B(t)$ and $\boldsymbol{\omega}_B(t)$ can be interpreted as the average linear and angular velocities of the deformable body. Actually the separation of rigid and elastic d.o.f. is not fully rigorous since the relative distance is evaluated on the body deformed configuration. Such a rigid-deformable partitioning can be appreciated in the kinetic energy $T(t)$ with the following terms:

$$T = T_{RR} + T_{DD} + T_{RD}, \tag{2.17}$$

representing respectively the classical kinetic energy associated with a free rigid body, the additional kinetic energy associated with the deformable motion only and the mixed contribution of rigid and elastic coordinates. The basic idea of the Tisserand approach consists of looking for a family of floating reference frames with respectively linear and angular velocities $\boldsymbol{v}_B(t)$ and $\boldsymbol{\omega}_B(t)$ in such a way that the deformable kinetic energy $T_{DD}(t)$ is minimized, namely:

$$\begin{aligned} \min_{\boldsymbol{v}_B,\boldsymbol{\omega}_B} T_{DD} &= \min_{\boldsymbol{v}_B,\boldsymbol{\omega}_B} \frac{1}{2}\int_{\mathcal{V}} \rho\, \boldsymbol{v}_D^{\mathsf{T}}\boldsymbol{v}_D \,\mathrm{d}\mathcal{V} \\ &= \min_{\boldsymbol{v}_B,\boldsymbol{\omega}_B} \frac{1}{2}\int_{\mathcal{V}} \rho\, [\boldsymbol{v} - \boldsymbol{v}_B - \boldsymbol{\omega}_B \times (\boldsymbol{r} + \boldsymbol{s})]^{\mathsf{T}}[\boldsymbol{v} - \boldsymbol{v}_B - \boldsymbol{\omega}_B \times (\boldsymbol{r} + \boldsymbol{s})] \,\mathrm{d}\mathcal{V}. \end{aligned} \tag{2.18}$$

Solving such a minimization problem by setting to zero the partial derivatives of the functional with respect to the free parameters it is possible to derive the following conditions for the relative velocity:

$$\begin{aligned} \frac{\partial T_{DD}}{\partial \boldsymbol{v}_B} &= -\int_{\mathcal{V}} \rho\, \boldsymbol{v}_D \,\mathrm{d}\mathcal{V} = -\boldsymbol{l}_D = 0 \\ \frac{\partial T_{DD}}{\partial \boldsymbol{\omega}_B} &= \int_{\mathcal{V}} \rho\, (\boldsymbol{r} + \boldsymbol{s}) \times \boldsymbol{v}_D \,\mathrm{d}\mathcal{V} = \boldsymbol{h}_D = 0. \end{aligned} \tag{2.19}$$

Stated in another way these conditions correspond to setting to zero the linear and angular momenta associated with the deformable motion. Therefore the linear and angular momenta of a deformable body have formally the same expression as in the case of a rigid body. Another important consequence is that the mixed rigid-deformable contribution of the kinetic energy is zero, or in other words the inertial decoupling is achieved:

$$T_{RD} = \int_{\mathcal{V}} \rho\, \boldsymbol{v}_R^{\mathsf{T}}\boldsymbol{v}_D \,\mathrm{d}\mathcal{V} = \boldsymbol{v}_B^{\mathsf{T}} \int_{\mathcal{V}} \rho\, \boldsymbol{v}_D \,\mathrm{d}\mathcal{V} - \boldsymbol{\omega}_B^{\mathsf{T}} \int_{\mathcal{V}} \rho\, (\boldsymbol{r} + \boldsymbol{s}) \times \boldsymbol{v}_D \,\mathrm{d}\mathcal{V} = 0. \tag{2.20}$$

It is also possible to prove that such a family of Tisserand reference frames satisfying Eq. (2.19) has the following interesting property: the average angular velocity is the same and the only difference is a rigid translation.

A Buckens reference frame, usually referred to as mean axes, can be defined as a first-order linearization of the more general Tisserand reference frame in the case of small structural displacements. More in particular with the assumption of constant density it is possible to simplify the condition on the angular momentum of Eq. (2.19) as follows:

$$\begin{aligned}\int_{\mathcal{V}} \rho\,(\boldsymbol{r}+\boldsymbol{s})\times\boldsymbol{v}_D\,\mathrm{d}\mathcal{V} &= \int_{\mathcal{V}} \rho\,\boldsymbol{r}\times\dot{\boldsymbol{s}}\,\mathrm{d}\mathcal{V}+\mathcal{O}(\boldsymbol{s}^2)\\ &\simeq \frac{\mathrm{d}}{\mathrm{d}t}\int_{\mathcal{V}} \rho\,\boldsymbol{r}\times\boldsymbol{s}\,\mathrm{d}\mathcal{V}=0,\end{aligned} \tag{2.21}$$

which is referred to as "practical" mean axes constraint. Substituting it into Eq. (2.20)
it is straightforward to prove that the inertial decoupling of rigid and elastic d.o.f. is achieved once again. It is also remarkable that the definition of mean axes implies that for small motions the resulting overall linear and angular momenta of the deformable structure remain the same of the rigid structure. So, in turn, the center of gravity of a deforming structure and the equations governing the dynamics of the floating reference frame remain the same of the parent rigid body. However mean axes formally differ from Tisserand ones in the sense that they aim at minimizing the $L^2(\mathcal{V})$ norm of the relative displacements rather than the relative kinetic energy, or in other words constraints are set on displacements and not velocities.

Resorting now to Eq. (2.11) for the numerical approximation of the structural displacements with the technique of separation of variables and highlighting the subsets of generally-speaking rigid and deformable d.o.f. the mean axes constraints of Eq. (2.21) can be rewritten as follows:

$$\int_{\mathcal{V}} [\,\boldsymbol{N}_R\,]^{\mathsf{T}}\rho\,[\,\boldsymbol{N}_M\,]\,\mathrm{d}\mathcal{V}=0 \qquad \text{and} \qquad \int_{\mathcal{V}} [\,\boldsymbol{N}_M\,]^{\mathsf{T}}\rho\,[\,\boldsymbol{N}_R\,]\,\mathrm{d}\mathcal{V}=0 \tag{2.22}$$

where the subscript of the deformable shape functions $[\,\boldsymbol{N}_D(\boldsymbol{x})\,]$ is here changed to $[\,\boldsymbol{N}_M(\boldsymbol{x})\,]$ in order to stress that such a basis is compliant with mean axes constraints. It is worthwhile to remark that assembling a complete set of "attached" deformable shape functions for for the numerical analysis of a statically determinate structure as in Eq. (2.11) is a relatively easy task. On the contrary guessing a priori a complete set of "mean axes" deformable shape functions satisfying Eq. (2.22) is a bit more difficult. The vibration modes would be the ideal candidate because of their mutual orthogonality but they are not for free, a lot of calculations being required for their determination. Since any linear combination of the elements of a basis remains a basis, an operative convenient strategy to define a complete set of "mean axes" deformable shape functions $[\,\boldsymbol{N}_M(\boldsymbol{x})\,]$ consists of assembling the following linear combination of already available "attached" deformable $[\,\boldsymbol{N}_D(\boldsymbol{x})\,]$ and rigid $[\,\boldsymbol{N}_R(\boldsymbol{x})\,]$ shape functions:

$$[\,\boldsymbol{N}_M\,]=[\,\boldsymbol{N}_D\,]-[\,\boldsymbol{N}_R\,][\,\mathbf{Z}\,] \tag{2.23}$$

where the matrix $[\,\mathbf{Z}\,]\in\mathbb{R}^{N_R\times R_D}$ implementing the linear combination of deformable and rigid shape functions can be determined by enforcing the constraints of Eq. (2.23):

$$\begin{aligned}\int_{\mathcal{V}} [\,\boldsymbol{N}_R\,]^{\mathsf{T}} \rho\, [\,\boldsymbol{N}_M\,]\, \mathrm{d}\mathcal{V} &= \int_{\mathcal{V}} [\,\boldsymbol{N}_R\,]^{\mathsf{T}} \rho\, [\,\boldsymbol{N}_D\,]\, \mathrm{d}\mathcal{V} - \int_{\mathcal{V}} [\,\boldsymbol{N}_R\,]^{\mathsf{T}} \rho\, [\,\boldsymbol{N}_R\,]\, \mathrm{d}\mathcal{V}\, [\,\mathbf{Z}\,] \\ &= [\,\mathbf{M}_{RD}\,] - [\,\mathbf{M}_{RR}\,]\, [\,\mathbf{Z}\,] = 0,\end{aligned} \tag{2.24}$$

which yields the following solution: $[\,\mathbf{Z}\,] = [\,\mathbf{M}_{RR}\,]^{-1} [\,\mathbf{M}_{RD}\,]$. It is worthwhile to remark that the above recovery of a mean axes set from any given attached set is, algebraically speaking, nothing but the application of the generalized Gram-Schmidt subspace orthogonalization procedure. If we now substitute matrix $[\,\mathbf{Z}\,]$ in Eq. (2.23) and compare the expressions for the unknown structural displacements $\boldsymbol{u}(\boldsymbol{x}, t)$ written as a function of the generalized d.o.f. in both attached $\{\boldsymbol{q}(t)\}$ and in mean $\{\overline{\boldsymbol{q}}(t)\}$ axes, namely:

$$\begin{aligned}\boldsymbol{u}(\boldsymbol{x}, t) &\simeq \left[\begin{array}{cc} \boldsymbol{N}_R & \boldsymbol{N}_M \end{array}\right] \left\{\begin{array}{c} \overline{\boldsymbol{q}}_R \\ \overline{\boldsymbol{q}}_D \end{array}\right\} \\ &= \left[\begin{array}{cc} \boldsymbol{N}_R & \boldsymbol{N}_D \end{array}\right] \left[\begin{array}{cc} \mathbf{I} & -\mathbf{M}_{RR}^{-1}\mathbf{M}_{RD} \\ 0 & \mathbf{I} \end{array}\right] \left\{\begin{array}{c} \overline{\boldsymbol{q}}_R \\ \overline{\boldsymbol{q}}_D \end{array}\right\} \\ &= \left[\begin{array}{cc} \boldsymbol{N}_R & \boldsymbol{N}_D \end{array}\right] \left\{\begin{array}{c} \boldsymbol{q}_R \\ \boldsymbol{q}_D \end{array}\right\},\end{aligned} \tag{2.25}$$

it is possible to infer an linear invertible transformation of the free amplitudes only $\{\overline{\boldsymbol{q}}\} = [\,\mathbf{T}\,]\{\boldsymbol{q}\}$ with $[\,\mathbf{T}\,] \in \mathbb{R}^{N_s \times N_s}$ for efficiently shifting from attached to mean axes:

$$\mathbf{T} = \left[\begin{array}{cc} \mathbf{I} & -\mathbf{M}_{RR}^{-1}\mathbf{M}_{RD} \\ 0 & \mathbf{I} \end{array}\right] \qquad \text{and} \qquad \mathbf{T}^{-1} = \left[\begin{array}{cc} \mathbf{I} & \mathbf{M}_{RR}^{-1}\mathbf{M}_{RD} \\ 0 & \mathbf{I} \end{array}\right]. \tag{2.26}$$

It is remarkable that the differences between the generalized coordinates in both attached and mean axes are related only to the generally-speaking rigid d.o.f. while the generally-speaking deformable d.o.f. are not affected. Moreover it is possible to restate the structural problem of Eq. (2.12) from attached to mean axes simply applying the linear invertible transformation described above to the mass, damping and stiffness matrices and to the generalized forces array already computed in an attached reference frame as shown in Eq. (2.13), without repeating any numerical integration, as follows:

$$\begin{aligned}[\,\overline{\mathbf{M}}\,] &= [\,\mathbf{T}\,]^{\mathsf{T}} [\,\mathbf{M}\,] [\,\mathbf{T}\,] = \left[\begin{array}{cc} \mathbf{M}_{RR} & 0 \\ 0 & \mathbf{M}_{DD} - \mathbf{M}_{RD}^{\mathsf{T}}\mathbf{M}_{RR}^{-1}\mathbf{M}_{RD} \end{array}\right] \\ [\,\overline{\mathbf{C}}\,] &= [\,\mathbf{T}\,]^{\mathsf{T}} [\,\mathbf{C}\,] [\,\mathbf{T}\,] = \left[\begin{array}{cc} 0 & 0 \\ 0 & \mathbf{C}_{DD} \end{array}\right] \\ [\,\overline{\mathbf{K}}\,] &= [\,\mathbf{T}\,]^{\mathsf{T}} [\,\mathbf{K}\,] [\,\mathbf{T}\,] = \left[\begin{array}{cc} 0 & 0 \\ 0 & \mathbf{K}_{DD} \end{array}\right]\end{aligned} \tag{2.27}$$

$$\{\overline{\boldsymbol{Q}}\} = [\,\mathbf{T}\,]^{\mathsf{T}}\{\boldsymbol{Q}\} = \left\{ \begin{array}{c} \boldsymbol{Q}_R \\ \boldsymbol{Q}_D - \mathbf{M}_{RD}^{\mathsf{T}}\mathbf{M}_{RR}^{-1}\boldsymbol{Q}_R \end{array} \right\}.$$

It is worthwhile to remark that such a generalized forces array exciting the deformable d.o.f. corresponds to the inertia relief of the rigid external forces. A similar interpretation can be applied for justifying the additional contribution to the mass matrix, which corresponds to the inertia relief of the rigid-deformable inertia forces. Therefore the inertia relief strategy plays an important role within the framework of mean axes reference frame since it alone is capable of decoupling the generally-speaking rigid and deformable d.o.f. in the left-hand side of the governing equations. [54]

2.2 Aerodynamic sub-system

The aerodynamic sub-system can be schematized as shown in Figure 2.2 as a block which receives in input the current structural displacements and velocities suitably interpolated on the aerodynamic d.o.f. $\{\boldsymbol{u}_a(t)\}$ and $\{\dot{\boldsymbol{u}}_a(t)\}$ and returns in output the aerodynamic forces $\{\boldsymbol{F}_a^a(t)\}$. The gust velocity $\{\boldsymbol{v}_g(t)\}$ is also shown. The typical mission envelope of many modern civil and military aircraft includes long segments of flight in the transonic regime, with Mach numbers varying within the interval $M_\infty \in (0.7,\, 1.3)$. In such a flow regime the numerical solution of the unsteady flow-field around the aircraft and the computation of the aerodynamic loads is a difficult task. In fact it is not possible to use the classical mathematical models relying on a linearization of the flow-field for small perturbances about a reference condition, such as in the Doublet Lattice Method (DLM), because of the poor quality of the numerical results. On the contrary it is necessary to resort to the mathematical models and numerical methods within the framework of Computational Fluid Dynamics (CFD). The (numerical) linearization of the aerodynamic loads can be eventually performed in the post-processing stage.

2.2.1 Transonic flow regime

In order to better understand the difficulties associated to the transonic flow regime it is worthwhile to study what changes within the flow-field of an ideal non-viscous and non-conductive fluid around a generally non-symmetric airfoil as the free-stream Mach number M_∞ increases. With reference to Figure 2.3 it is possible to list the following stages, with significantly different flow features:

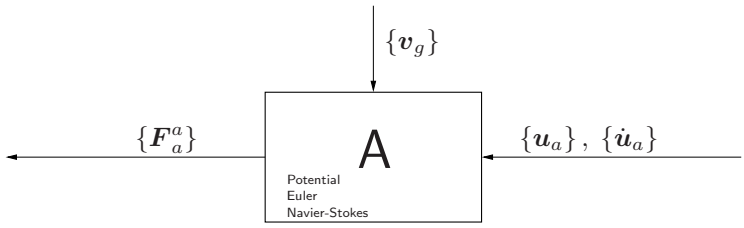

Figure 2.2: Block diagram for the aerodynamic sub-system.

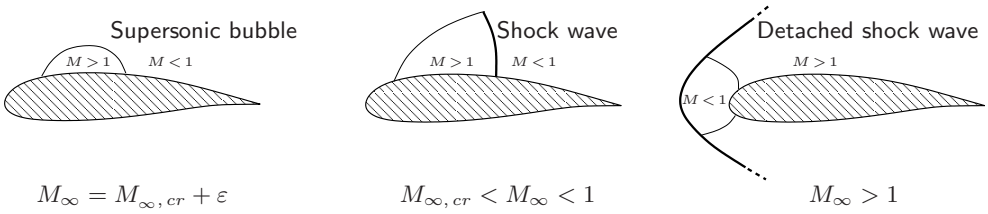

Figure 2.3: Qualitative evolution of transonic flow-field around a non-symmetric airfoil as the free-stream Mach number M_∞ is increased.

a) The lower limit of the transonic flow regime can be identified by means of the critical Mach number $M_{\infty,\,cr}$, defined as the free-stream Mach number such that locally sonic conditions, namely $M_P = 1$, are reached at point P close to the abscissa of maximum thickness of the airfoil. Of course such a parameter depends significantly on the shape of the airfoil and the angle of attack and qualitatively decreases as the maximum thickness of the airfoil and/or the angle of attack are increased.

b) For $M_\infty > M_{\infty,\,cr}$ a locally supersonic region, called "supersonic bubble", begins to grow near-by point P separated by the subsonic flow-field by a sonic line. The diverging exansion waves originating within the accelerating portion of the upper surface of the airfoil are reflected by the sonic line (with uniform pressure) as compression waves. Such mutually converging waves eventually form a shock wave before reaching the airfoil surface.

c) As the free-stream Mach number M_∞ increases, the the supersonic bubble on the upper surface of the airfoil grows bigger and bigger and the corresponding shock wave is intensified as it moves towards the trailing edge. At the same time a supersonic bubble is observed also on the lower surface of the airfoil which grows very rapidly until the corresponding shock waves reaches the trailing edge. The hypotheses of omoentropic and irrotational flow-field are not valid anymore when the intensity and the curvature of the shock waves are significant.

d) Finally for $M_\infty > 1$ the topology of the flow-field changes completely. It is possible to observe a detached curved shock wave with a small subsonic region near-by the leading edge of the airfoil, while the local Mach number is supersonic everywhere else. As the free-stream Mach number increases, such a subsonic region becomes progressively smaller and smaller. However it does not ever disappear completely if the the leading edge of the airfoil is rounded and not sharp.

As a consequence the main distinctive feature of the transonic flow regime is the contemporary presence within the flow-field of locally subsonic and supersonic regions, possibly separated by irreversible phenomena such as shock waves. Within the framework of mathematical modelling, this alone is a big challenge as e.g. the mathematical properties of the governing equations change significantly between the subsonic and supersonic regions, being elliptic and hyperbolic respectively.

Moreover the problem can become more and more complex because of highly non-linear phenomena, such as the interaction of the shock wave with the boundary layer and/or with the structural motion. For instance the shock wave may promote the turbulent transition or even the unsteady separation of the boundary layer (buffeting), inducing significant and potentially dangerous vibrations of the structural sub-system. Moreover the interaction of shock waves with the structural motion may lead to dynamic instabilities of the aeroservoelastic system, such as the self-excited divergent oscillations of the control surfaces (aileron buzz).

2.2.2 Mathematical modelling of the aerodynamic sub-system

Because of the intrinsic difficulties associated with the transonic flow regime, in order to effectively tackle the aerodynamic problem it is necessary to resort to the more sophisticated mathematical models and numerical methods within the fruitful research field of Computational Fluid Dynamics (CFD). [10, 28, 29, 36] Of course this choice implies higher computational costs in terms of run-time and memory with respect to the linearized tools. Therefore the ability of identifying the mathematical model and numerical method providing the best compromise between accuracy of the results and computational efficiency is mandatory. This is especially true within a design and/or verification environment, when a considerable number of configurations must be taken into account. In order to provide a guidance for striking the best balance between quality and costs, it is useful to provide a short survey of the mathematical models and numerical methods commonly adopted within the framework of Computational Aeroservoelasticity (CA). Proceeding with successive simplifications, it is possible to list the following options:

Navier-Stokes equations: The system of mixed non-linear Partial Differential Equations (PDE) governing the dynamics of the flow of a compressible, viscous and conductive fluid can be written within an Eulerian framework in differential conservative form as follows:

$$\frac{\partial \mathbf{u}}{\partial t} + \nabla \cdot \mathbf{f}(\mathbf{u}) = \nabla \cdot \mathbf{d}(\mathbf{u}) \qquad \forall\, (\boldsymbol{x},\, t) \in \mathcal{V} \times \mathcal{T}, \tag{2.28}$$

where $\mathcal{V} \subseteq \mathbb{R}^{N_d}$ and $\mathcal{T} \subseteq \mathbb{R}^{+}$ are the space and time domains of the problem respectively. The array of the conservative variables $\mathbf{u}(\boldsymbol{x}, t)$, inviscid fluxes $\mathbf{f}(\mathbf{u})$ and viscous fluxes $\mathbf{d}(\mathbf{u})$ are defined respectively as follows:

$$\mathbf{u} = \left\{ \begin{array}{c} \rho \\ \rho\, \boldsymbol{v} \\ E^t \end{array} \right\} \qquad \mathbf{f} = \left\{ \begin{array}{c} \rho\, \boldsymbol{v} \\ \rho\, \boldsymbol{v} \otimes \boldsymbol{v} + P[\,\mathbf{I}\,] \\ \boldsymbol{v}\,(E^t + P) \end{array} \right\} \qquad \mathbf{d} = \left\{ \begin{array}{c} 0 \\ \boldsymbol{\tau} \\ \boldsymbol{\tau} \cdot \boldsymbol{v} + \boldsymbol{q} \end{array} \right\}, \tag{2.29}$$

where $\rho(\boldsymbol{x}, t)$, $\boldsymbol{v}(\boldsymbol{x}, t)$ and $E^t(\boldsymbol{x}, t)$ are the density, the velocity and the total specific energy per unit volume, $P(\boldsymbol{x}, t)$, $\boldsymbol{\tau}(\boldsymbol{x}, t)$ and $\boldsymbol{q}(\boldsymbol{x}, t)$ are the pressure, the viscous stresses tensor and the power exchanged by conduction and finally $[\,\mathbf{I}\,] \in \mathbb{R}^{N_d \times N_d}$ is the identity matrix.

The problem is closed when the equation of state for the pressure $P(\boldsymbol{x}, t)$ is specified, together with the constitutive equations for the viscous stresses tensor $\boldsymbol{\tau}(\boldsymbol{x}, t)$ and the power exchanged by conduction $\boldsymbol{q}(\boldsymbol{x}, t)$. Assuming that the air can be approximated by means of the simplest Polytropic Ideal Gas (PIG) thermodynamic model with a constant ratio between the pressure and volume specific heats $\gamma = C_P/C_V$, the equation of state can be written as follows:

$$P = (\gamma - 1)\, E \qquad \text{with} \qquad E = E^t - \frac{1}{2}\rho|\boldsymbol{v}|^2 \tag{2.30}$$

Alternatively it is possible to resort to the more sophisticated thermodynamic models of thermochemical equilibrium and non-equilibrium, more expensive but with a wider validity interval. Adding the hypothesis of Newtonian fluid it is possible to write the symmetric tensor of the viscous stresses as proportional to the deformation velocity and with the Fourier hypothesis the power exchanged by conduction is easily written as aligned to the temperature gradient, namely:

$$\boldsymbol{\tau} = \frac{\mu}{2}\left[(\nabla \otimes \boldsymbol{v}) + (\nabla \otimes \boldsymbol{v})^{\mathsf{T}}\right] + \lambda\, \nabla \cdot \boldsymbol{v}\, [\,\mathbf{I}\,] \qquad \text{and} \qquad \boldsymbol{q} = -\kappa\, \nabla T, \tag{2.31}$$

where $\mu(T)$, $\lambda(T)$ and $\kappa(T)$ are respectively the dynamic viscosity, bulk viscosity and thermal conduction coefficients. [77]

Before solving the problem, it is necessary to define suitable initial and boundary conditions by assigning the value of the solution in the whole domain $\mathcal{V}$ at the initial time $t = 0$, namely: $\mathbf{u}(\boldsymbol{x}, 0) = \mathbf{u}_0(\boldsymbol{x})$ and the value of the solution on the boundary of the domain $\mathcal{S} = \partial\mathcal{V}$ for all times $t \in \mathcal{T}$, namely: $\mathbf{u}(\boldsymbol{x} \in \mathcal{S}, t) = \mathbf{b}(t)$. On a solid/wall boundary, such as the surface of a wing immersed in a fluid flow, it is necessary to enforce the no-slip boundary condition by setting to zero all the components of the local velocity $\boldsymbol{v}|_{\mathcal{S}^w} = 0$.

The numerical results of such a mathematical model agree with the experimental data for both laminar and turbulent fluid flows. However in this latter case a very detailed discretization of the computational domain is mandatory in order to correctly resolve the small scale fluctuations (in space and/or time) of the physical variables within the flow-field. The computational cost of Direct Numerical Simulation (DNS) is still very prohibitive for industrial applications. In order to overcome such a limitation it is convenient to apply a local time averaging operator to the problem, obtaining the Reynolds Averaged Navier-Stokes (RANS) equations. The unknowns of the problem now correspond to the physical variables of the mean flow-field, while the additional diffusion due to the turbulent fluctuations is modelled within the symmetric tensor of the Reynolds stresses $\boldsymbol{\tau}^R(\boldsymbol{x}, t)$. A number of turbulence models, ranging from very simple algebraic models (e.g. mixing length) to more sophisticated differential ones (e.g. Spalart-Allmaras, $\kappa - \omega$) are available to close the problem by making explicit the six independent components of the Reynolds stresses tensor as a function the physical variables of the mean flow-field. Recently even more complex options are being surveyed, such as the enrichment of turbulence models with the so-called Detached Eddy Simulation (DES) in order to predict massively separated flow. [62]

Euler equations: When investigating the flow-field with a high Reynolds number Re around an aerodynamic body at a moderate angle of attack α, it is possible to assume that the dynamic effects associated to the viscous diffusion and thermal conduction are confined within a thin layer close to the body, called boundary layer. In order to solve the flow-field outside the boundary layer it is possible to resort to the simplified model of non-viscous ($\mu = 0$ and $\lambda = 0$) and non-conductive ($\kappa = 0$) fluid. With such an hypothesis it is possible to neglect within the momentum and energy equations the contributions associated with the viscous stress tensor and the exchanged power by conduction. The system of hyperbolic non-linear Partial Differential Equations (PDE) governing the dynamics of the flow of a compressible, non-viscous and non-conductive fluid can be written within an Eulerian framework in differential conservative form as follows:

$$\frac{\partial \mathbf{u}}{\partial t} + \nabla \cdot \mathbf{f}(\mathbf{u}) = 0 \qquad \forall\, (\boldsymbol{x},\, t) \in \mathcal{V} \times \mathcal{T}, \tag{2.32}$$

where $\mathcal{V} \subseteq \mathbb{R}^{N_d}$ and $\mathcal{T} \subseteq \mathbb{R}^{+}$ are the space and time domains of the problem respectively. The array of the conservative variables $\mathbf{u}(\boldsymbol{x}, t)$, inviscid fluxes $\mathbf{f}(\mathbf{u})$ are defined in Eq. (2.29).

A difference with respect to the Navier-Stokes equations is how to deal with boundary conditions. In fact it is necessary to assign the value of the solution only on the "inflow" boundary of the domain that is the subset of the boundary along which: $\boldsymbol{\beta} \cdot \widehat{\boldsymbol{n}} < 0$, where $\boldsymbol{\beta}$ is the local advection velocity while $\widehat{\boldsymbol{n}}$ is the normal unit vector of the boundary (assumed positive if pointing outside the fluid domain). Moreover on a solid/wall boundary, such as the surface of a wing immersed in a fluid flow, it is necessary to enforce the slip boundary condition by setting to zero the normal component of the local velocity $\boldsymbol{v} \cdot \widehat{\boldsymbol{n}}|_{\mathcal{S}^w} = 0$. Alternatively it is possible to assign a non-zero value to the normal component of the local velocity, called "transpiration" velocity, in order to simulate the geometric and kinematic effects of a given displacement law of the boundary without actually deforming the computational grid.

The numerical results of such a mathematical model agree with the experimental data in terms of the pressure distribution on the surface of the body. Therefore it is possible to evaluate the load contributions associated with lift, pressure and induced drag, but not the viscous drag (small for well-designed wings with high efficiency and moderate angle of attacks). Moreover within the framework of aeroservoelastic analysis of conventional wings, neglecting the contribution of viscous drag does not always jeopardize the quality of the design. In fact the operator for assembling the Generalized Aerodynamic Forces (GAF) $\{\boldsymbol{Q}^a(t)\}$ of Eq. (2.13) corresponds to an average operator weighted on the modal shapes and for conventional structural configurations the displacements normal to the chord plane are generally much larger than those within the chord plane.

Full potential equations: If we add the hypotheses that the flow-field is irrotational ($\nabla \times \boldsymbol{v} = 0$) and the domain is singly connected, it is possible to write the velocity $\boldsymbol{v}(\boldsymbol{x}, t)$ as the gradient of a scalar potential $\Phi(\boldsymbol{x}, t)$, namely: $\boldsymbol{v} = \nabla\Phi$.

Resorting to Crocco's equation it is also possible to prove that the flow-field is omoentropic, i.e. irreversible phenomena such as shock waves are not allowed. As a consequence such a mathematical model cannot be rigorously used within the transonic flow regime, featuring locally subsonic and supersonic regions separated by shock waves. However the entropy variation due to a shock wave increases with the cubic power of the local Mach number, namely: $\Delta s = \mathcal{O}(M^3)$. Therefore such a mathematical model is considered from an engineer perspective a valid analysis tool for local Mach numbers up to: $M = 1.3 \div 1.4$. Carrying out all computations it is possible to write the following mixed non-linear Partial Differential Equation (PDE):

$$\frac{\partial^2 \Phi}{\partial t^2} + \frac{\partial (\nabla \Phi)^2}{\partial t} + \nabla \Phi \cdot \nabla \left(\frac{\nabla \Phi \cdot \nabla \Phi}{2} \right) - c^2 \, \nabla^2 \Phi = 0 \qquad \forall \, (\boldsymbol{x}, \, t) \in \mathcal{V} \times \mathcal{T}, \tag{2.33}$$

where $\mathcal{V} \subseteq \mathbb{R}^{N_d}$ and $\mathcal{T} \subseteq \mathbb{R}^+$ are the space and time domains of the problem respectively. The local speed of sound $c(\boldsymbol{x}, t)$ can be written as a function of the scalar potential $\Phi(\boldsymbol{x}, t)$, the free-stream velocity V_∞ and speed of sound c_∞ by means of the following unsteady compressible form of Bernoulli's theorem:

$$\frac{\partial \Phi}{\partial t} + \frac{|\boldsymbol{v}|^2}{2} + \frac{c^2}{\gamma - 1} = \frac{V_\infty^2}{2} + \frac{c_\infty^2}{\gamma - 1}. \tag{2.34}$$

Substituting the classic isoentropic relations $P/P_\infty = (T/T_\infty)^{\frac{\gamma}{\gamma-1}} = (c^2/c_\infty^2)^{\frac{\gamma}{\gamma-1}}$ in Eq. (2.34) and carrying out all the computations it is possible to evaluate the aerodynamic loads as follows:

$$C_p = \frac{\left[1 - \dfrac{\gamma - 1}{c_\infty^2} \left(\dfrac{\partial \Phi}{\partial t} + \dfrac{\|\boldsymbol{v}\|^2 - V_\infty^2}{2} \right) \right]^{\frac{\gamma}{\gamma-1}} - 1}{\dfrac{1}{2} \gamma \, M_\infty^2}. \tag{2.35}$$

Before solving the problem, it is necessary to define suitable initial and boundary conditions. On a solid/wall boundary, such as the surface of a wing immersed in a fluid flow, it is necessary to enforce the slip boundary condition by setting to zero the normal component of the gradient of the scalar potential $\nabla \Phi \cdot \widehat{\boldsymbol{n}}|_{\mathcal{S}^w} = 0$. When dealing with a lifting body it is worthwhile to remark that the wake originating from the the trailing edge of the wing must be taken into account. A discontinuity of the scalar potential $\Delta \Phi$ is advected along such a wake, as it is straightforward to prove by requesting that the resultant of the aerodynamic forces is zero on the wake.

Linear(ized) potential equations: If we add to the hypotheses above the assumption that the flow-field is incompressible ($\nabla \cdot \boldsymbol{v} = 0$) it is easy to show that the scalar potential $\Phi(\boldsymbol{x}, t)$ is governed by the following elliptic Partial Differential Equation (PDE), also known as Laplace equation:

$$\nabla^2 \Phi = 0 \qquad \forall \, (\boldsymbol{x}, \, t) \in \mathcal{V} \times \mathcal{T}. \tag{2.36}$$

Such a mathematical model is much simpler since it is linear (superposition principle holds) and its time dependency is hidden in the boundary conditions. Within the framework of the linear(ized) potential theory, the Doublet Lattice Method (DLM) is a collocation method for calculating the unsteady aerodynamic loads for interfering lifting surfaces oscillating harmonically in a subsonic fluid flow. It has been used over the past 40 years for unsteady aerodynamic prediction and still today continues to be the first choice for routine aeroelastic analyses of subsonic aircraft. The geometry is extremely simplified, consisting of a set of flat lifting surfaces without thickness nor camber, although fuselage, nacelles and external stores can be included as interfering bodies. A linear relationship is assumed between the Generalized Aerodynamic Forces (GAF) $\{\boldsymbol{Q}^a(t)\}$ and the generalized structural d.o.f. $\{\boldsymbol{q}(t)\}$ by means of a so-called Aerodynamic Influence Coefficient (AIC) matrix as follows:

$$\{\boldsymbol{Q}^a\} = [\,\mathbf{AIC}(M_\infty, \kappa)\,]\,\{\boldsymbol{q}\} \tag{2.37}$$

This matrix is computed only once, at supplied Mach numbers M_∞ and reduced frequencies κ, and this feature allows the DLM to be extremely cost-effective for routine analyses. However, to provide reliable information in the transonic regime, a costly correction process based on wind tunnel data is necessary.

2.2.3 Arbitrary Lagrangian Eulerian formulation

A fundamentally important consideration when dealing with the mathematical models and numerical methods to tackle problems with moving boundaries is the choice of an appropriate kinematical description of the continuum. In fact, such a choice determines the relationship between the deforming continuum and the computational grid, and thus conditions the ability of the numerical method to deal with large distortions and to provide an accurate resolution of material interfaces and mobile boundaries. The algorithms within the framework of continuum mechanics usually make use of two classical descriptions of motion: the Lagrangian description and the Eulerian description. The Arbitrary Lagrangian Eulerian (ALE) description is aimed at combining the advantages of the above classical kinematical descriptions, while minimizing the respective drawbacks as far as possible.

Within a Lagrangian framework, mainly used in structural dynamics, each node of the computational grid follows the associated material particle during motion. Such a description allows for an easy tracking of free surfaces and interfaces between different materials. It also facilitates the treatment of e.g. materials with history-dependent constitutive relations. Its weakness is its inability to follow large distortions of the computational domain without resorting to frequent and expensive remeshing. Within an Eulerian framework, mainly used in fluid dynamics, the computational grid is fixed and the continuum moves with respect to it. Such a description allows for a relatively easy handling of large distortions in the continuum motion, but generally at the expense of precise interface tracking and the resolution of flow details. Finally the Arbitrary Lagrangian Eulerian (ALE) kinematical description is a generalization of the classical frameworks, resting upon the introduction of a so-called "referential" domain and on the mapping with the classical material and spatial domains. [22]

Without loss of generality, let us focus on a simple conservation law for a scalar function $f(\boldsymbol{x}, t)$. This study is easily generalized to much more complex problems. A fundamental ingredient within such an Arbitrary Lagrangian Eulerian (ALE) framework is the Reynolds' transport theorem, which yields the following relationship between Lagrangian and Eulerian perspectives:

$$\frac{\mathrm{d}}{\mathrm{d}t}\int_{\mathcal{V}(t)} f\,\mathrm{d}\mathcal{V} = \int_V \left[\frac{\partial f}{\partial t} + \nabla\cdot(f\,\mathbf{v})\right]\mathrm{d}V = \int_V \frac{\partial f}{\partial t}\,\mathrm{d}V + \oint_S f\,\mathbf{v}\cdot\widehat{\boldsymbol{n}}\,\mathrm{d}S \tag{2.38}$$

where $V \subseteq \mathbb{R}^{N_d}$ is a fixed control volume delimited by boundary $S = \partial V \subseteq \mathbb{R}^{N_d-1}$ coincident with the time-varying spatial domain $\mathcal{V}(t) \subseteq \mathbb{R}^{N_d}$ at considered time t. Finally $\mathbf{v}(\boldsymbol{x}, t)$ is the local so-called material velocity. The classical approach to prove Eq. (2.38) relies on the availability of the invertible transformation $\boldsymbol{x} = \boldsymbol{\varphi}(\boldsymbol{X}, t)$ between the set of reference coordinates $\boldsymbol{X}$ and the set of general space coordinates $\boldsymbol{x}$. The Jacobian of such a transformation $J = \det(\partial\boldsymbol{x}/\partial\boldsymbol{X})$ can be also interpreted as the relative volume increment between current and reference configurations, namely: $J\mathrm{d}V = \mathrm{d}\mathcal{V}$. With this in mind Eq. (2.38) can be rewritten as follows:

$$\begin{aligned}
\frac{\mathrm{d}}{\mathrm{d}t}\int_{\mathcal{V}(t)} f\,\mathrm{d}\mathcal{V} &= \frac{\mathrm{d}}{\mathrm{d}t}\int_V f\,J\mathrm{d}V \\
&= \int_V \left[\frac{\mathrm{d}f}{\mathrm{d}t}J + f\frac{\mathrm{d}J}{\mathrm{d}t}\right]\mathrm{d}V \\
&= \int_V \left[\frac{\partial f}{\partial t} + \mathbf{v}\cdot\nabla f + f(\nabla\cdot\mathbf{v})\right] J\mathrm{d}V \\
&= \int_V \left[\frac{\partial f}{\partial t} + \nabla\cdot(f\mathbf{v})\right] J\mathrm{d}V \\
&= \int_{\mathcal{V}(t)} \left[\frac{\partial f}{\partial t} + \nabla\cdot(f\mathbf{v})\right]\mathrm{d}\mathcal{V},
\end{aligned} \tag{2.39}$$

where we employed the chain rule for the derivation of a multivariate function and the following well-known result about the Jacobian: $\mathrm{d}J/\mathrm{d}t = J(\nabla\cdot\mathbf{v})$. An alternative approach to write the Reynolds' transport theorem exploits the so-called "generalized functions". The most widely used generalized functions are the so-called Heaviside step function $H(\boldsymbol{x})$ and the Dirac delta function $\delta(\boldsymbol{x})$. Such functions can be defined as the limits of a sequence of functions. Although the function sequences are not unique, the property of the limit function are. [34, 51] As opposed to the mono-dimensional case, in the multi-dimensional case it is difficult to provide a simple graphical representation of such generalized functions. With reference to Figure 2.4 the following definitions are convenient:

$$H(\boldsymbol{x}, \Omega) : \mathbb{R}^{N_d} \longrightarrow \mathbb{R} \quad \text{s.t} \quad H = \begin{cases} 1 & \text{if} \quad \boldsymbol{x} \in \Omega \\ 0 & \text{if} \quad \boldsymbol{x} \notin \Omega, \end{cases} \tag{2.40}$$

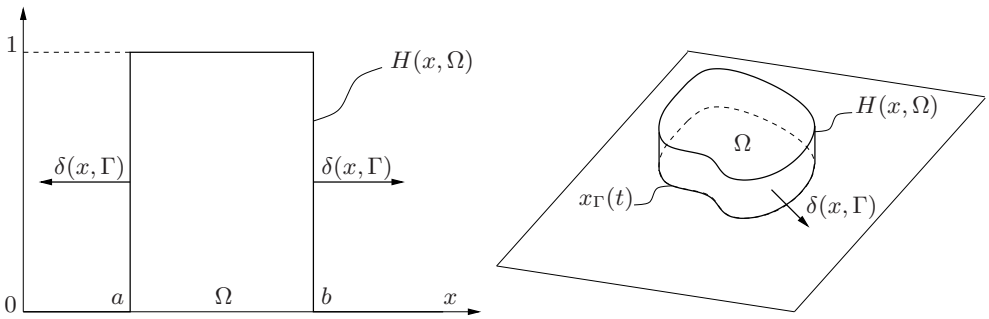

Figure 2.4: Graphical representation of the generalized functions $H(\boldsymbol{x},\Omega)$ and $\delta(\boldsymbol{x},\Gamma)$ in the mono-dimensional (left) and multi-dimensional (right) cases.

$$\delta(\boldsymbol{x},\Gamma) = -\nabla H \cdot \widehat{\boldsymbol{n}} : \mathbb{R}^{N_d} \longrightarrow \mathbb{R} \quad \text{s.t} \quad \delta = \begin{cases} 1 & \text{if} \quad \boldsymbol{x} \in \Gamma = \partial\Omega \\ 0 & \text{if} \quad \boldsymbol{x} \notin \Gamma = \partial\Omega. \end{cases} \tag{2.41}$$

Moreover as the gradient (to be intended in a distributional sense) of the Heaviside function is non-zero only along the direction of the normal unit vector, it is possible to infer the following result: $\nabla H = -\delta\widehat{\boldsymbol{n}}$. It is useful to verify that in the mono-dimensional case the Heaviside function $H(x,\Omega)$ of Eq. (2.40) is different from the usual step function $h(x)$. More precisely it is a combination of suitable step functions in order to "sample" the region $\Omega = [a,b]$, that is: $H(x,\Omega) = h(x-a) - h(x-b)$. Such a property makes it possible to rewrite any definite integral over the interval Ω as the indefinite integral of the argument multiplied (in a distributional sense) by the Heaviside function $H(\boldsymbol{x},\Omega)$. Similarly the indefinite integral of the argument multiplied (in a distributional sense) by the Dirac function $\delta(\boldsymbol{x},\Gamma)$ corresponds to the definite integral of the argument over the boundary Γ. If the interval $\Omega(t)$ is time-varying it is convenient to make explicit the dependence of the Heaviside function on the interval by means of the space coordinates $\boldsymbol{x}_\Gamma(t)$ of the boundary $\Gamma(t)$ as follows: $H(\boldsymbol{x},\Omega) = H(\boldsymbol{x}-\boldsymbol{x}_\Gamma)$. Applying the chain rule for the derivation of a multivariate function it is possible to write the time derivative of the Heaviside function as follows: $\dot{H} = \nabla H \cdot \dot{\boldsymbol{x}}_\Gamma = \delta\widehat{\boldsymbol{n}} \cdot \mathbf{v}$. With such tools available it is finally possible to rewrite the Reynolds' transport theorem as follows:

$$\begin{aligned} \frac{\mathrm{d}}{\mathrm{d}t}\int_{\mathcal{V}(t)} f \,\mathrm{d}\mathcal{V} &= \frac{\mathrm{d}}{\mathrm{d}t}\int f H \,\mathrm{d}V \\ &= \int \frac{\partial f}{\partial t} H \,\mathrm{d}V + \int f \frac{\partial H}{\partial t} \,\mathrm{d}V \\ &= \int \frac{\partial f}{\partial t} H \,\mathrm{d}V + \int f \delta\widehat{\boldsymbol{n}} \cdot \mathbf{v} \,\mathrm{d}V \\ &= \int_V \frac{\partial f}{\partial t} \,\mathrm{d}V + \oint_S f \,\mathbf{v} \cdot \widehat{\boldsymbol{n}} \,\mathrm{d}S. \end{aligned} \tag{2.42}$$

The Reynolds Averaged Navier-Stokes (RANS) equations governing the dynamics of a compressible, viscous and conductive fluid can be rewritten within an Arbitrary Lagrangian Eulerian (ALE) framework in integral conservative form as follows:

$$\frac{\mathrm{d}}{\mathrm{d}t}\int_{\mathcal{V}(t)} \mathbf{u}\,\mathrm{d}\mathcal{V} + \oint_{\mathcal{S}(t)} \left[\mathbf{f}(\mathbf{u}) - \mathbf{u}\,\mathbf{v}\right]\cdot\widehat{\boldsymbol{n}}\,\mathrm{d}\mathcal{S} + \oint_{\mathcal{S}(t)} \mathbf{d}(\mathbf{u})\cdot\widehat{\boldsymbol{n}}\,\mathrm{d}\mathcal{S} = 0, \tag{2.43}$$

where $\mathcal{V}(t) \subseteq \mathbb{R}^{N_d}$ is the time-varying spatial domain, while $\mathcal{S}(t) = \partial\mathcal{V}(t) \subseteq \mathbb{R}^{N_d-1}$ is the boundary with normal unit vector $\widehat{\boldsymbol{n}}(\boldsymbol{x},t)$, assumed positive when pointing outside the fluid domain. Moreover $\mathbf{u}(\boldsymbol{x},t)$, $\mathbf{f}(\mathbf{u})$ and $\mathbf{d}(\mathbf{u})$ are the arrays of conservative variables, inviscid and viscous fluxes already defined in Eq. (2.29) and finally $\mathbf{v}(\boldsymbol{x},t)$ is the local velocity of the moving boundaries (therefore with a negative sign). [30, 31]

2.2.4 Aerodynamic transfer functions matrix

In order to tackle the aeroservoelastic problem it is necessary to compute the unsteady variation of the aerodynamic loads with respect to a reference steady-state solution due to the structural motion. Within the framework of classical aeroservoelasticity the classical linear(ized) numerical methods such as the DLM represent directly in the frequency domain the relation between the array of the generalized aerodynamic forces $\{\boldsymbol{Q}^a(s)\}$ and the generalized displacements $\{\boldsymbol{q}(s)\}$ by means of the so-called aerodynamic transfer functions matrix $[\,\boldsymbol{H}_{am}(p)\,] \in \mathbb{C}^{N_s\times N_s}$ as follows:

$$\{\boldsymbol{Q}^a(s)\} = [\,\boldsymbol{H}_{am}(p, M_\infty, Re)\,]\{\boldsymbol{q}(s)\}, \tag{2.44}$$

where the complex reduced frequency $p = sL_a/V_\infty = h + \boldsymbol{i}k$ depends on the aerodynamic reference length L_a (generally equivalent to half the mean aerodynamic chord) and the velocity V_∞. The dependency on the Mach number M_∞ and the Reynolds number Re is also highlighted. Actually the aerodynamic transfer functions matrix $[\,\boldsymbol{H}_{am}(p)\,] = [\,\boldsymbol{H}_{am}(\boldsymbol{i}k)\,] = [\,\boldsymbol{H}_{am}(k)\,]$ is computed only along the imaginary axis $\mathbb{I}m$ of the complex vector space $\mathbb{C}$ and therefore the availability of dedicated numerical methods to "extrapolate" such data to the whole complex vector space is mandatory.

Assuming that the aerodynamic sub-system is asymptotically stable (as verified experimentally) and is excited only with causal input signals, it is convenient to build a representation equivalent to Eq. (2.44) in the time domain, by writing the array of the generalized aerodynamic forces $\{\boldsymbol{Q}^a(t)\}$ as the convolution integral of the so-called aerodynamic impulse responses matrix $[\,\boldsymbol{h}_{am}(t)\,] \in \mathbb{R}^{N_s\times N_s}$ and the generalized displacements $\{\boldsymbol{q}(t)\}$ as follows:

$$\{\boldsymbol{Q}^a(t)\} = \int_0^\infty [\,\boldsymbol{h}_{am}(t-\tau, M_\infty, Re)\,]\{\boldsymbol{q}(\tau)\}\,\mathrm{d}\tau, \tag{2.45}$$

It is remarkable that, if the d.o.f. associated with the control surfaces $\{\boldsymbol{\delta}\}$ are already included within the array of structural coordinates $\{\boldsymbol{q}\}$, Eq. (2.44) and/or Eq. (2.45) account also for the contribution of the aerodynamic loads associated to the control surfaces deflection.

Viceversa it is convenient to treat separately the unsteady variation of the aerodynamic loads with respect to a reference steady-state solution due to gust or turbulence $\{\boldsymbol{Q}^g(t)\}$, depending on whether the input signal $\{\boldsymbol{v}_g(t)\}$ is modelled with a deterministic or stochastic approach respectively. Such contribution is very important for the certification of the aircraft. In fact current regulations require to survey within the design process the gust and turbulence response of the aircraft as possibly dimensioning load conditions. The approach is similar to the one discussed above and relies on the availability of the so-called gust transfer functions matrix $[\,\boldsymbol{H}_{ag}(p)\,] \in \mathbb{C}^{N_s \times N_{a,\,b}}$ and gust impulse responses matrix $[\,\boldsymbol{h}_{ag}(t)\,] \in \mathbb{R}^{N_s \times N_{a,\,b}}$.

When dealing with the transonic flow regime, highly non-linear because of the contemporary presence within the flow-field of subsonic and supersonic regions separated by irreversible phenomena such as shock waves, such a linear(ized) framework does not appear viable. However, if the flow-field associated with the reference steady-state solution is highly non-linear, the same is not necessarily true for the unsteady variation of the aerodynamic loads due to the structural motion. Assuming that the structural displacements are small, it is remarkable that the numerical results of the mathematical model of Eq. (2.44) and/or Eq. (2.45), linear(ized) about a non-linear reference steady-state solution, fairly agree with the real behaviour of the aerodynamic sub-system. Within such a framework the potential of Computational Fluid Dynamics (CFD) is significant, since it allows: a) to accurately predict the non-linear reference steady-state solution and b) to include within the linear(ized) mathematical the influence of the structural deformability on the shock wave position and intensity.

In order to compute the aerodynamic transfer functions matrix $[\,\boldsymbol{H}_{am}(k)\,]$ with the mathematical models and numerical methods of Computational Fluid Dynamics (CFD), a numerical simulation formally identical to the experimental procedure to identify a Reduced Order Model (ROM) of the aerodynamic loads based on wind tunnel data must be performed. The critical tasks are the following:

a) First of all it is necessary to compute the reference steady-state solution of the aeroservoelastic problem, coupling a steady-state aerodynamic solver with a steady-state structural solver, e.g. by means of the classical iterative method. The set of the steady-state aerodynamic loads and structural displacements at convergence corresponds to the reference equilibrium or "trim" configuration for the (numerical) linearization of the generalized aerodynamic forces. More in particular the following problem classes must be taken into account: restrained and free-flying. For the case of a wind tunnel model attached to the wind tunnel wall, the case is called a restrained case. The attachment provides the balancing forces and moments according to the aerodynamic and inertial loads working on the model. On the other hand for the case of a free-flying object like an aircraft, the inertial and the aerodynamic forces must balance each other. This option is slightly more difficult since it requires the solution of a non-linear problem.

b) It is now possible to compute and store as a "snapshot" the unsteady variation of the array of the generalized aerodynamic forces $\{\boldsymbol{Q}^a(t)\}$ due to a prescribed excitation time history applied only to the j-th generalized displacement $\boldsymbol{q}_j(t)$ while all the other structural d.o.f. are set to zero.

The j-th column of the aerodynamic transfer functions matrix $[\,\boldsymbol{H}_{am}(k)|_j\,]$ can be computed as to the ratio between the Fourier transforms of the output and input signals, namely:

$$[\,\boldsymbol{H}_{am}(k)|_j\,] = \frac{\mathcal{F}_\kappa(\,\{\boldsymbol{Q}^a(t)\}\,)}{\mathcal{F}_\kappa(\,\boldsymbol{q}_j(t)\,)} \tag{2.46}$$

where an efficient numerical implementation of operator $\mathcal{F}_\kappa(\cdot)$ is provided by the Fast Fourier Transform (FFT) algorithm. Repeating such a procedure for all the N_s structural d.o.f. and assembling the columns progressively available, the aerodynamic transfer functions matrix $[\,\boldsymbol{H}_{am}(k)\,]$ is built. It is worthwhile to remark that each column of the aerodynamic transfer functions matrix can be computed independently. Therefore the computational overhead is conveniently minimized by implementing a distributed strategy e.g. on N_s computing nodes, as shown in Figure 2.5. The block TRIM clearly refers to task a) while the blocks GAF and FFT correspond to the two halves (storing the snapshots and post-processing the data) of task b).

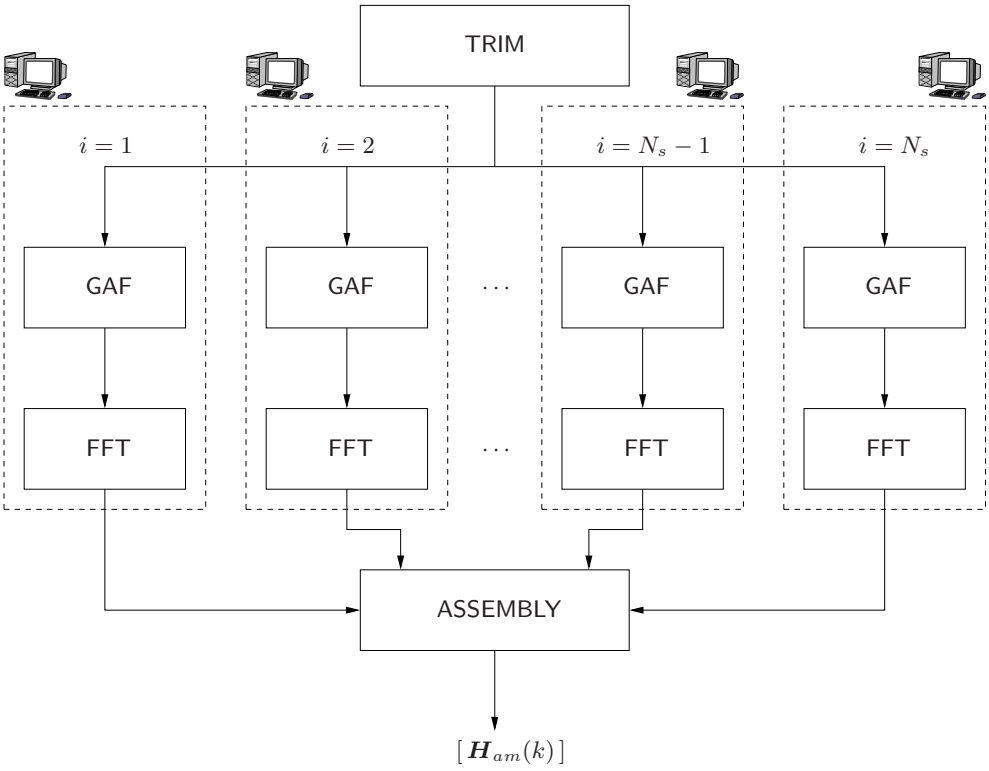

Figure 2.5: Block diagram of the procedure to build the aerodynamic transfer functions matrix $[\,\boldsymbol{H}_{am}(k)\,]$ by means of a (numerical) linearization of the unsteady aerodynamic loads due to the structural motion.

Of course the prescribed excitation time history applied to the j-th generalized displacement $\boldsymbol{q}_j(t)$ must meet a series of multidisciplinary requirements among which: the capability of exciting the frequency interval of interest with a signal amplitude well above the numerical error threshold but without jeopardizing the hypothesis of small perturbations. Within such a framework it is important to precisely define what we mean with "small", performing suitable static and dynamic linearity benchmarks. Moreover the programming effort and computational overhead associated with the numerical implementation of such an input signal must be taken into account. The most widely used options are:

Harmonic input: A classical choice consists in exciting the aerodynamic sub-system with a simple harmonic input signal with reduced frequency k_q and maximum amplitude A_q. Assuming that the system is Linear Time Invariant (LTI) and asymptotically stable, the frequency response theorem states that the output signal is also harmonic with equal reduced frequency k_q. As a consequence it is possible to compute the j-th column of the aerodynamic transfer functions matrix $[\,\boldsymbol{H}_{am}(k_q)|_j\,]$ at reduced frequency k_q. Clearly such a strategy implies a high computational overhead, since it is necessary to repeat the numerical simulation for each reduced frequency of interest.

Impulsive input: Choosing an ideal impulse of infinite amplitude and zero width as input signal for exciting the aerodynamic sub-system, the j-th column of the aerodynamic impulse responses matrix $[\,\boldsymbol{h}_{am}(t)|_j\,]$ would be readily available. Simply applying the Fourier transform operator, the j-th column of the aerodynamic transfer functions matrix $[\,\boldsymbol{H}_{am}(k)|_j\,]$ would also be available. Of course it is not possible to numerically implement an ideal impulse, but only a so-called real impulse of finite amplitude and width suitably chosen in order to excite the frequency interval of interest (a common practice within the framework of experimental structural dynamics). Clearly such a strategy implies a high computational overhead, since a very small timestep must be used in order to satisfactorily approximate the real impulse. Moreover, unless a very wide snapshot time window is chosen, it is difficult to accurately identify the static gain and the low frequency dynamics of the aerodynamic sub-system.

Step input: In order to accurately identify also the static gain and the low frequency dynamics, it is convenient to choose as input signal for exciting the aerodynamic sub-system an ideal step of prescribed maximum amplitude A_q. Such a strategy is promising if we consider only the geometric contribution to the boundary conditions, proportional to the j-th generalized displacement $\boldsymbol{q}_j(t)$. On the other hand the kinematic contribution to the boundary conditions is also proportional to the j-th generalized velocity $\dot{\boldsymbol{q}}_j(t)$, corresponding to an ideal impulse difficult to implement numerically as noted above. Moreover the Fourier transform of the output signal quite often features spurious Gibbs oscillations, jeopardizing the accurate identification of the high frequency dynamics of the aerodynamic sub-system.

In order to to compute the j-th column of the aerodynamic transfer functions matrix $[\,\boldsymbol{H}_{am}(k)|_j\,]$ it is convenient to resort to the so-called "deficiency" of the generalized aerodynamic forces, defined as follows:

$$\{\boldsymbol{D}^a(t)\} = \{\boldsymbol{Q}^a(t)\} - \{\boldsymbol{Q}^a_\infty\}\,, \tag{2.47}$$

where $\{\boldsymbol{Q}^a_\infty\}$ is the array of the steady-state generalized aerodynamic forces. Substituting Eq. (2.47) in Eq. (2.46) and multiplying by $\boldsymbol{i}k$ numerator and denominator it is finally possible to write:

$$[\,\boldsymbol{H}_{am}(k)|_j\,] = \frac{\{\boldsymbol{Q}^a_\infty\} + \boldsymbol{i}k\,\mathcal{F}_k(\,\{\boldsymbol{D}^a(t)\}\,)}{A_q}. \tag{2.48}$$

Blended step input: Finally in order to improve the identification of the Reduced Order Model (ROM) for the unsteady variation of the aerodynamic loads due to the structural motion, it is possible to choose a blended step input signal $q(\tau)$ for exciting the aerodynamic sub-system, namely:

$$q(\tau) = \begin{cases} \dfrac{A_q}{2}\,[1 - \cos(k_q\,\tau)] & \text{if} \quad \tau < \tau_q \\ A_q & \text{if} \quad \tau \geq \tau_q, \end{cases} \tag{2.49}$$

where the adimensional time $\tau = t\,V_\infty/L_a$ can be interpreted as the number of aerodynamic reference lengths travelled per unit time at the flight velocity V_∞. The corresponding time derivative $\dot{q}(\tau)$ can be written as follows:

$$\dot{q}(\tau) = \begin{cases} \dfrac{A_q\,k_q}{2}\,\sin(k_q\,\tau) & \text{if} \quad \tau < \tau_q \\ 0 & \text{if} \quad \tau \geq \tau_q. \end{cases} \tag{2.50}$$

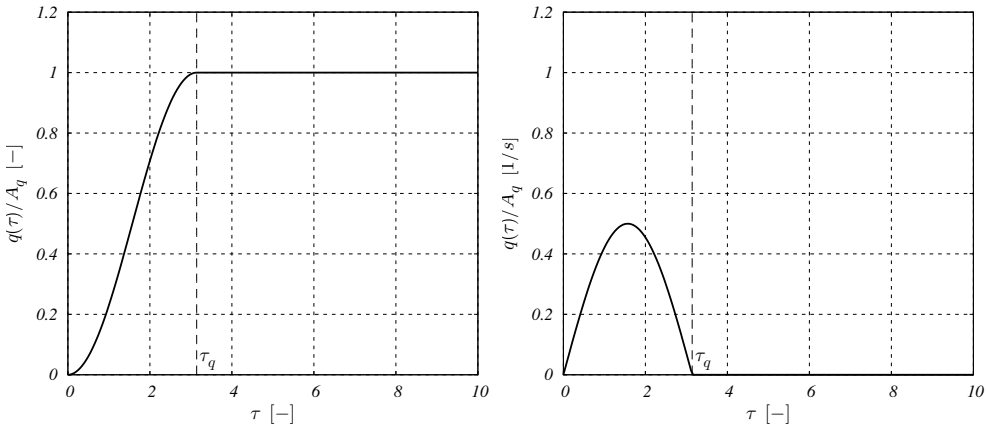

Figure 2.6: Blendend step input $q(\tau)$ and its derivative $\dot{q}(\tau)$ as a function of time τ.

The reduced frequency k_q or equivalently the adimensional time constant τ_q are suitably chosen in order to excite the frequency interval of interest $k \in [0,\, k_\infty]$ and do not depend on the particular coordinate under consideration, namely: $k_q = k_\infty/2$ and $\tau_q = 2\pi/k_\infty$. The maximum amplitude A_q is chosen with the aim of exciting the aerodynamic sub-system with an input signal signal well above the numerical error threshold but without jeopardizing the hypothesis of small perturbations. Suppose that we are dealing with a detailed Finite Element (FE) structural model suitably condensed by means of an efficient modal basis as follows: $\{\boldsymbol{u}_s\} = [\,\boldsymbol{U}\,]\{\boldsymbol{q}\}$, where the matrix $[\,\boldsymbol{U}\,] \in \mathbb{R}^{N_{FEM} \times N_q}$ stores the modal shapes. Within such a framework the maximum nodal velocity should be suitably small if compared with the flight velocity, e.g. $\max(\,\{\dot{\boldsymbol{u}}_s\}\,)/V_\infty = \varepsilon$ with $\varepsilon = \tan(1^\circ)$. Carrying out all the computations it is possible to write the following relation for the maximum amplitude A_q, dependent on the particular coordinate under consideration:

$$A_q = \frac{4\, L_a\, \varepsilon}{\max(\,[\,\boldsymbol{U}|_j\,]\,)\, k_\infty}. \tag{2.51}$$

Finally in order to to compute the j-th column of the aerodynamic transfer functions matrix $[\,\boldsymbol{H}_{am}(k)|_j\,]$ it is convenient to resort to Eq. (2.48), adding to the denominator the contribution of the Fourier transform of the deficiency of the input signal.

2.3 Aeroelastic interface

Within the framework of a closely-coupled partitioned approach to Computational Aeroelasticity (CA) a fundamental ingredient is the so-called aeroelastic interface, with the responsibility of realizing the closed-loop connection between the structural and aerodynamic sub-systems by means of a suitable interpolation strategy. More in particular the aerodynamic forces are translated into a load condition acting on the structural sub-system while the structural displacements and velocities modify the boundary conditions of the aerodynamic sub-system. We immediately see that such a task is not trivial at all. More in particular it is necessary to:

a) interpolate the structural displacements and velocities on the boundary nodes of the aerodynamic mesh. This implies the capability of connecting topologically different domains, e.g. a detailed aerodynamic model with high-fidelity representation of the aircraft geometry together with a simplified beam Finite Element (FE) structural model. This is especially true in the industrial environment, where they usually come from different departments, and are primarily developed for rather different purposes. To this end the availability of knobs for the control of the smoothness of the resulting surfaces is critical.

b) adjust the internal aerodynamic mesh to the newly computed boundary nodes in such a way that grid quality is not degraded significantly, e.g. with non-negative cell volumes, moderate levels of stretching, skewness and non-orthogonality.

This task of moving what can amount up to millions of nodes is to be performed thousands of times during an aeroelastic computation. Therefore the availability of efficient, massively parallel and robust mesh deformation tools and topology modifiers is crucial.

The second half of the problem is particularly challenging, both for its theoretical and practical implications, and in recent years a novel research field is growing specifically dedicated to dynamic mesh handling. If we now focus only on the first half of the problem, the aeroelastic interface scheme can be represented by means of a linear operator $[\,\mathcal{I}(\boldsymbol{x})\,] \in \mathbb{R}^{N_{a,\,b}} \times \mathbb{R}^{N_s}$ which suitably interpolates the structural displacements onto the aerodynamic boundary d.o.f., that is:

$$\{\boldsymbol{u}_a\} = [\,\mathcal{I}\,]\,\{\boldsymbol{u}_s\}. \tag{2.52}$$

The requirements that an accurate, efficient and flexible aeroelastic interface scheme must meet are the following: a) capability of linking models with non-matching spatial domains and numerical grids (e.g. type of discretization elements, d.o.f. number and positioning), b) exact treatment of rigid translations and rotations, c) conservation of the momentum and energy exchanged between the two sub-systems. This last point is particularly important. In fact the introduction or removal of spurious energy by the interface scheme may affect the overall stability properties of the aeroelastic system (as it easy to understand by resorting to Lyapunov energetic stability check $\mathrm{d}V/\mathrm{d}t < 0$, valid for non-linear dynamical systems for which it is possible to define an energy V).

It is then necessary to guarantee the equivalence of the virtual work made by the aerodynamic forces $\{\boldsymbol{F}_a^a(t)\}$ for the structural displacements interpolated on the aerodynamic d.o.f. $\{\boldsymbol{u}_a(t)\}$, with the virtual work made by the aerodynamic forces interpolated on the structural d.o.f. $\{\boldsymbol{F}_s^a(t)\}$ for the structural displacements $\{\boldsymbol{u}_s(t)\}$, namely:

$$\delta\mathcal{L} = \delta\{\boldsymbol{u}_s\}^{\mathsf{T}}\{\boldsymbol{F}_s^a\} = \delta\{\boldsymbol{u}_a\}^{\mathsf{T}}\{\boldsymbol{F}_a^a\}. \tag{2.53}$$

As a consequence the second half of the problem is also taken care of. Substituting Eq. (2.52) in Eq. (2.53) it is easy to show that the linear operator which interpolates the aerodynamic forces onto the structural d.o.f. is:

$$\{\boldsymbol{F}_s^a\} = [\,\mathcal{I}\,]^{\mathsf{T}}\,\{\boldsymbol{F}_a^a\}. \tag{2.54}$$

2.4 Aeroservoelastic system

In order to write the system of integral-differential equations governing the dynamics of the aeroservoelastic system, it is sufficient to make explicit in the system of ordinary differential equations of Eq. (2.12), governing the dynamics of the structural subsystem, the generalized aerodynamic forces $\{\boldsymbol{Q}^a(t)\}$ as a function of the generalized structural displacements $\{\boldsymbol{q}(t)\}$ by means of the linear(ized) reduced order model of Eq. (2.45), namely:

$$[\,\mathbf{M}\,]\,\{\ddot{\boldsymbol{q}}\} + [\,\mathbf{C}\,]\,\{\dot{\boldsymbol{q}}\} + [\,\mathbf{K}\,]\,\{\boldsymbol{q}\} - \int_0^\infty [\,\boldsymbol{h}_{am}(t-\tau)\,]\,\{\boldsymbol{q}(\tau)\}\,\mathrm{d}\tau = \{\boldsymbol{Q}\}. \tag{2.55}$$

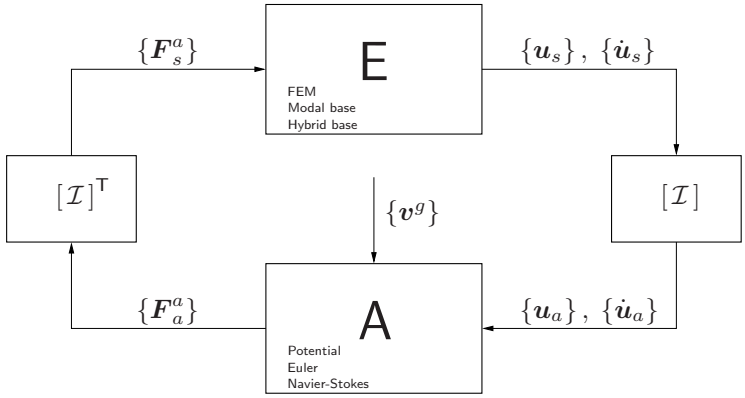

Figure 2.7: Block diagram of the aeroservoelastic system, highlighting the closed-loop connection between the structural E and aerodynamic A sub-systems by means of a suitable interpolation strategy $[\mathcal{I}]$.

Within the framework of classical aeroeservoelasticity it is convenient to rewrite such a problem in the frequency domain, transitioning from a system of integral-differential equations to the following system of algebraic equations:

$$\left(s^2 \left[\mathsf{M} \right] + s \left[\mathsf{C} \right] + \left[\mathsf{K} \right] - \left[\boldsymbol{H}_{am}(p) \right] \right) \{\boldsymbol{q}\} = \{\boldsymbol{Q}\} \,. \tag{2.56}$$

When dealing with problems with a particular focus on the "servo" branch of aeroservoelasticity, it is convenient to make explicit the contribution of the generalized aerodynamic forces due to the control surfaces deflection $\boldsymbol{Q}^{\delta}(t)$. For simplicity let us assume that we are dealing with the restrained case of a wing, equipped e.g. with flaps, slats and ailerons, attached to the wind tunnel wall. If the rigid d.o.f. associated with the control surfaces participate significantly to the deformability of the structure, it is correct that such rigid d.o.f. $\{\boldsymbol{\delta}(t)\}$ are included within the array of the generalized structural displacements $\{\boldsymbol{q}(t)\}$. This case is referred to as "free controls". Viceversa, if the motion of the control surfaces is significantly slower than the characteristic time of the deformable d.o.f. of the structure, it is possible to residualize the high-frequency dynamics, e.g. by neglecting the contribution of the coupling inertia forces. In this case we speak of "restrained controls". More in particular it is convenient to partition Eq. (2.56) by highlighting the rigid d.o.f. associated with control surfaces $\{\boldsymbol{\delta}(t)\}$ and the deformable coordinates $\{\boldsymbol{q}(t)\}$ as follows:

$$\begin{aligned} \left(s^2 \begin{bmatrix} \mathsf{M}_{qq} & \mathsf{M}_{q\delta} \\ \mathsf{M}_{\delta q} & \mathsf{M}_{\delta\delta} \end{bmatrix} + s \begin{bmatrix} \mathsf{C}_{qq} & 0 \\ 0 & 0 \end{bmatrix} + \begin{bmatrix} \mathsf{K}_{qq} & 0 \\ 0 & 0 \end{bmatrix} \right. \\ \left. - \begin{bmatrix} \boldsymbol{H}_{am\,qq}(p) & \boldsymbol{H}_{am\,q\delta}(p) \\ \boldsymbol{H}_{am\,\delta q}(p) & \boldsymbol{H}_{am\,\delta\delta}(p) \end{bmatrix} \right) \begin{Bmatrix} \boldsymbol{q} \\ \boldsymbol{\delta} \end{Bmatrix} = \begin{Bmatrix} \boldsymbol{Q} \\ \boldsymbol{H} \end{Bmatrix}, \end{aligned} \tag{2.57}$$

where $\{\boldsymbol{H}(s)\}$ is the Fourier transform of the generalized hinge moments associated to the control surfaces. If we now neglect the contribution of the inertia forces: $[\,\mathbf{M}_{q\delta}\,]\{\ddot{\boldsymbol{\delta}}\} \ll 1$, an appropriate approximation for statically balanced control surfaces, it is possible to rewrite the equations governing the dynamics of the deformable d.o.f. of the structure as follows:

$$\left(\, s^2\,[\,\mathbf{M}_{qq}\,] + s\,[\,\mathbf{C}_{qq}\,] + [\,\mathbf{K}_{qq}\,] - [\,\boldsymbol{H}_{am\,qq}(p)\,]\,\right)\{\boldsymbol{q}\} = \{\boldsymbol{Q}\} + [\,\boldsymbol{H}_{am\,q\delta}(p)\,]\,\{\boldsymbol{\delta}\}\,, \quad (2.58)$$

in a more convenient form from the point of view of the active control systems designer. The equations governing the dynamics of the rigid d.o.f. associated with control surfaces can be neglected for the solution of the aeroservoelastic problem. However such a model must be readily recovered within the dimensioning stage of the aircraft systems in order to assess the feasibility of the control surfaces displacement laws.

Similarly, if the aerodynamic characteristic time $T_a = L_a/V_\infty$ is significantly smaller than the characteristic time of the deformable dynamics of the structure $T_s = 2\pi/\omega$, it is convenient to resort to a suitable quasi-steady approximation of the real dynamics of the aerodynamic sub-system. Assuming that the flight condition is constant (thus removing the dependence on Reynolds Re and Mach M_∞ numbers) and that the aerodynamic transfer functions matrix is analytical in $p = 0$, it is possible to expand Eq. (2.44) in Taylor series as follows:

$$\begin{aligned}
\{\boldsymbol{Q}^a(s)\} &= [\,\boldsymbol{H}_{am}(p)\,]\{\boldsymbol{q}(s)\} \\
&\simeq \left(\,[\,\boldsymbol{H}_{am}(0)\,] + p[\,\boldsymbol{H}'_{am}(0)\,] + \frac{p^2}{2}[\,\boldsymbol{H}''_{am}(0)\,]\right)\{\boldsymbol{q}(s)\} + \mathcal{O}(p^3) \\
&\simeq \left(\,[\,\mathbf{K}_a\,] \quad + s\frac{L_a}{V_\infty}[\,\mathbf{C}_a\,] \quad + s^2\frac{L_a^2}{V_\infty^2}[\,\mathbf{M}_a\,] \quad\right)\{\boldsymbol{q}(s)\} + \mathcal{O}(s^3),
\end{aligned} \quad (2.59)$$

where $[\,\mathbf{M}_a\,]$, $[\,\mathbf{C}_a\,]$ and $[\,\mathbf{K}_a\,] \in \mathbb{C}^{N_s \times N_s}$ are the aerodynamic mass, damping and stiffness matrices respectively. It is convenient to consider no more than three terms in the Taylor series expansion in order not to break the symmetry between the aerodynamic and structural sub-systems. If the aerodynamic transfer functions matrix $[\,\boldsymbol{H}_{am}(p)\,]$ is analytical, it is possible to compute its derivative along any direction, e.g. the imaginary axis $\mathbb{I}m$ of the complex vector space $\mathbb{C}$. More in particular, if we resort to a Finite Differences (FD) centered approximation scheme, only $[\,\boldsymbol{H}_{am}(0)\,]$ and $[\,\boldsymbol{H}_{am}(\Delta k)\,]$ with $\Delta k \ll 1$ are needed.

It is worthwhile to remark that the quasi-steady approximation yields a significant simplification of the aeroservoelastic problem written in the time domain. In fact the system of integro-differential equations of Eq. (2.55) becomes the following much simpler to tackle system of ordinary differential equations:

$$\left([\,\mathbf{M}\,] - \frac{L_a^2}{V_\infty^2}[\,\mathbf{M}_a\,]\right)\{\ddot{\boldsymbol{q}}\} + \left([\,\mathbf{C}\,] - \frac{L_a}{V_\infty}[\,\mathbf{C}_a\,]\right)\{\dot{\boldsymbol{q}}\} + \left([\,\mathbf{K}\,] - [\,\mathbf{K}_a\,]\right)\{\boldsymbol{q}\} = \{\boldsymbol{Q}\}. \quad (2.60)$$

2.4.1 Static applications

With reference to Figure 2.8 two types of static aeroelastic simulation can be carried out, i.e. restrained and free-flying. For the case of a wind tunnel model attached to the wind tunnel wall, the case is called a restrained case. The attachment provides the balancing forces and moments according to the aerodynamic and inertial loads working on the model. The modelling of such a problem in static aeroelastic simulations is straightforward.

For the case of a free-flying object like an aircraft, the inertial and the aerodynamic forces must balance each other. This implies that when the aerodynamic forces are frozen, e.g. by specifying Mach number M_∞, angle of attack α and control surface deflection δ, the acceleration of the aircraft may not be specified separately. Instead, the acceleration should be calculated from the aerodynamic forces by means of the so-called inertial relief method. [54] On the contrary, when the acceleration of the aircraft is frozen, e.g. by specifying load factor n, the aerodynamic configuration should be sought at which the aerodynamic forces will balance the resulting inertial forces. This option is slightly more difficult since it requires the solution of a non-linear problem.

It is convenient to formulate the trim problem into a mean axes reference frame in order to eliminate (by definition) the inertial coupling between rigid/flight-mechanics and deformable motions. This favorable property is automatically embedded into the choice of free-free normal modes of vibration basis. However the coupling still appears on the right hand side with the aerodynamic forces. Without loss of generality, if we now focus on the longitudinal trim problem we have the following set of rigid and elastic conditions:

$$F_z(M_\infty, \alpha, \delta, \{\boldsymbol{q}\}) = n\,W \tag{2.61a}$$

$$M_{y,\,CG}(M_\infty, \alpha, \delta, \{\boldsymbol{q}\}) = 0 \tag{2.61b}$$

$$[\overline{\mathbf{K}}]\{\boldsymbol{q}\} = \{\boldsymbol{Q}_a(M_\infty, \alpha, \delta, \{\boldsymbol{q}\})\}, \tag{2.61c}$$

assuming that the available engine thrust is sufficient for the equilibrium along the x-direction to be satisfied a-priori and neglecting the engine thrust contribution to the pitching moment (small for conventional aircraft).

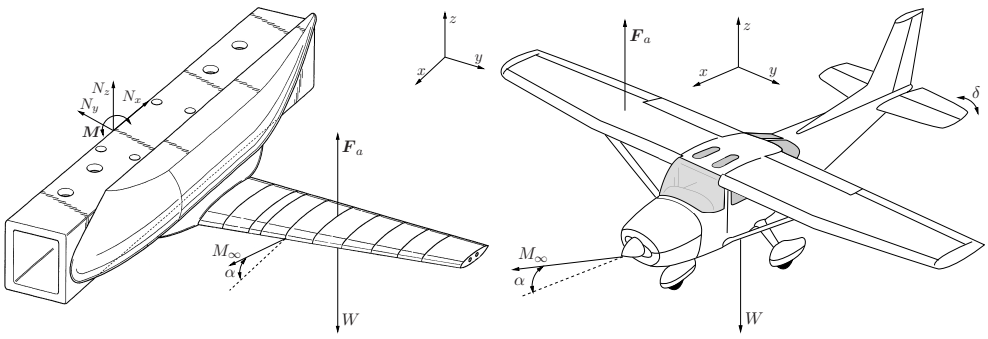

Figure 2.8: Longitudinal trim problem for restrained vs. free-flying aircraft

With reference to the block diagram of Figure 2.9, the numerical procedure to solve the non-linear aeroelastic trim problem (which can also be interpreted as an optimization problem with forces and moments as the objectives, trim parameters as the free variables and limits as the constraints) can be summarized as follows:

a) The procedure starts with the computation of the aerodynamic steady-state solution in the undeformed reference configuration, that is with the rigid $\{q_r\}$ and elastic $\{q_e\}$ d.o.f set to zero. In the longitudinal case this implies setting to zero the rigid pitch α, the elevator deflection δ and modal amplitudes $\{q\}$. Then it is necessary to build an approximation of the Jacobian matrix $[\,J_r\,]$ of the rigid trim conditions, to solve the non-linear rigid trim problem e.g. by means of a modified Newton-Raphson method, that is without updating the Jacobian matrix with significant time savings. The easiest strategy to build such a matrix consists of applying a small perturbation on each k-th active d.o.f., computing the corresponding aerodynamic steady-state solution and then assembling each k-th column of $[\,J_r\,]$ by means of Finite Differences (FD). To further maximize computational efficiency the aerodynamic solution is not driven to steady-state but an inner iterations limit is set. By employing all the convergence acceleration techniques available an inner iterations limit of $I = 100$ is effective. Such a Jacobian matrix $[\,J_r\,]$ is only an approximation of the real stability derivatives matrix of the rigid aircraft, because the aerodynamic solution is not completely converged within the inner iterations limit and the active d.o.f. are perturbed non-independently. However the quality of the approximation of the Jacobian matrix only affects and to a lesser extent the convergence speed of modified Newton-Raphson method without any impact of the accuracy of the results. Therefore the user can also choose to skip this step and to import the stability derivatives predicted bt lower-fidelity methods such as DLM.

b) When the Jacobian matrix $[\,J_r\,]$ is available it is possible to start the outer iterations for the rigid trim. At each k-th outer iteration of the modified Newton-Raphson method the resultant rigid-body aerodynamic forces and moments are computed and the residuals of the rigid trim conditions are assembled. The rigid subset of the active d.o.f. is then updated with a suitable relaxation factor $\omega \leq 1$ for increased robustness. After checking that the rigid d.o.f. are within the user-defined saturation limits, the configuration of the aircraft is deformed accordingly. If no elastic d.o.f. are active these steps are repeated until convergence to the non-linear trim of a rigid aircraft of Eq. (2.61a-2.61b).

c) After the first $1/\omega$ outer iterations during which only rigid d.o.f. are updated while elastic d.o.f are set to zero, it is possible to to start the outer iterations for the elastic trim. This delayed start is due to robustness issues. It is better to first drive the rigid d.o.f. close to convergence and then superimpose the elastic deformation onto a configuration almost satisfying the inertial relief condition. At each k-th outer iteration the Generalized Aerodynamic Forces (GAF) are computed and the linear system of Eq. (2.61c) is solved for the corresponding generalized displacements as in the classical iterative method. These steps are repeated until convergence to the non-linear trim of an elastic aircraft.

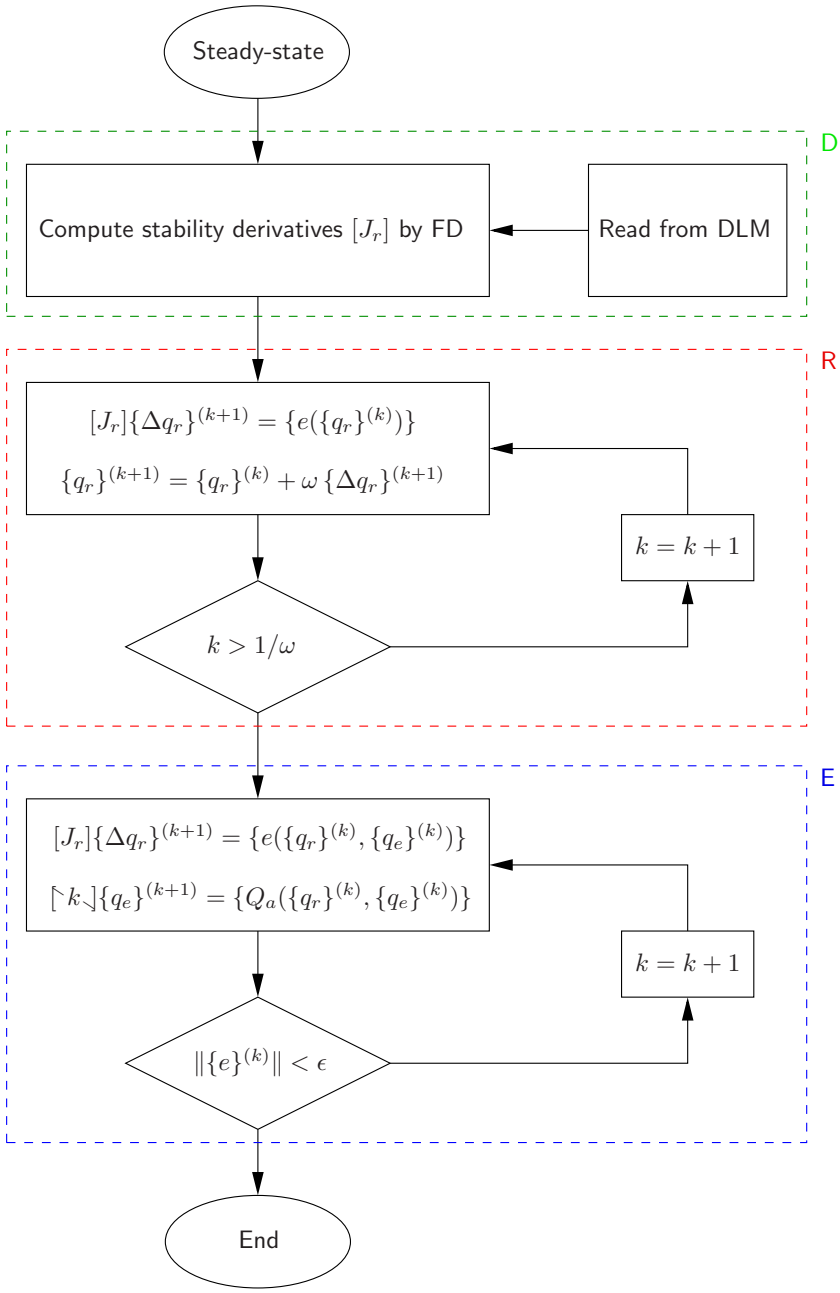

Figure 2.9: Block diagram for the proposed non-linear aeroelastic trim procedure. We also highlight the blocks responsible for computing the stability derivatives (D), for approaching to the trim conditions of the rigid aricraft (R) and for converging to the trim conditions of the elastic aircraft (E).

2.4.2 Dynamic applications

Probably the most important or at least notorious aeroservoelastic dynamic problem is "flutter". Its relevance stems from the potential catastrophic consequences on the structural integrity of the aircraft and from the prominence given to flutter clearance testing in order to open the flight envelope of the aircraft during the qualification of the vehicle against the regulatory standards of EASA/FAA.

From a physical perspective flutter corresponds to the occurrence of self-excited divergent oscillations e.g. of the wing or horizontal and vertical tail surfaces with the aforementioned potential catastrophic consequences on the structural integrity of the aircraft, whereas from a mathematical perspective it corresponds to the analysis of the stability properties of the locally Linear(ized) Time Invariant (LTI) aeroservoelastic system for small perturbations of a reference equilibrium condition. As a consequence of the closed-loop interaction with the aerodynamic sub-system, the eigenvalues of the structural sub-system may shift in the unstable half with positive real part $\mathbb{R}e > 0$ of the complex vector space $\mathbb{C}$. Viceversa experiments show that the eigenvalues of the aerodynamic sub-system are always stable. Within such a framework flutter corresponds to the limit dynamic stability condition, i.e. at least one eigenvalue of the aeroservoelastic system crosses the imaginary axis $\mathbb{I}m$ of the complex vector space $\mathbb{C}$ or in other terms the associated damping is zero. As discussed above such an approximation is justified also when dealing with highly non-linear aeroservoelastic phenomena such as transonic flutter, buffeting and aileron buzz within the framework of Computational Aeroservoelasticity (CA).

Besides the the analysis of the stability properties of the locally linear(ized) aeroservoelastic system, it is often necessary to run a numerical simulation formally identical to a wind-tunnel or in-flight experimental campaign, by solving the non-linear equations governing the dynamics of the structural and aerodynamic sub-system suitably coupled by means of the aeroelastic interface. Such a "direct simulation" procedure is very expensive but it paves the way for e.g. the investigation of the post-flutter behaviour of the aircraft and it is particularly suited for the verification of critical configurations.

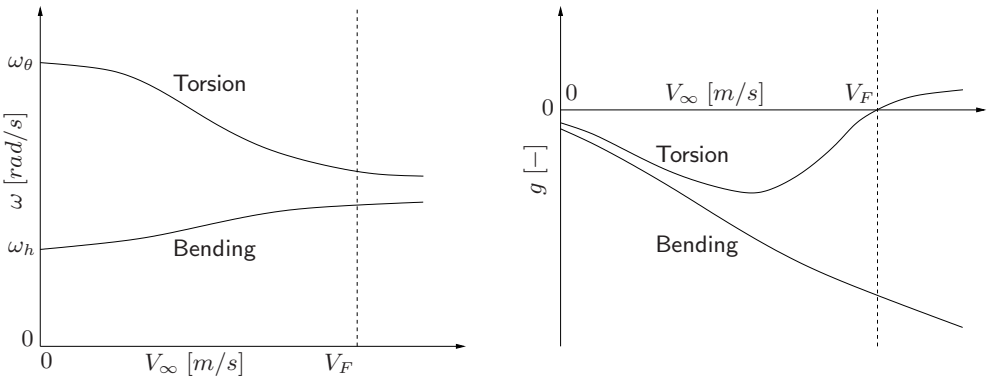

Figure 2.10: Qualitative $V_\infty - \omega$ (left) and $V_\infty - g$ (right) diagrams for an aeroservoelastic system with 2 d.o.f. (bending h and torsion θ).

In order to tackle the flutter problem in the frequency domain, or in other terms within the framework of "classical" aeroservoelasticity, it is sufficient to re-evaluate Eq. (2.56) on the imaginary axis $\mathbb{I}m$ of the complex vector space $\mathbb{C}$ with $s = \boldsymbol{i}\omega$ and neglect external forces. It is then necessary to solve the following homogeneous system of algebraic equations:

$$\left(-\omega^2 \, [\, \mathbf{M} \,] + \boldsymbol{i}\omega \, [\, \mathbf{C} \,] + [\, \mathbf{K} \,] - [\, \boldsymbol{H}_{am}(k) \,] \right) \{\boldsymbol{q}\} = 0, \tag{2.62}$$

with non-trivial solutions only if matrix $[\, \mathbf{A}(\omega, V_\infty) \,]$ is singular. By requiring that the real and imaginary parts of the determinant of matrix $\det([\, \mathbf{A}(\omega, V_\infty) \,])$ are zero, it is relatively easy to compute the flutter frequency ω_F and the flutter velocity V_F. Successively it is also possible to solve for the associated eigenvectors $\{\boldsymbol{q}(\omega_F, V_F)\}$. This information provides a useful guidance for understanding which structural d.o.f. participate more significantly to the flutter mechanism and therefore are more critical for the stability of the aeroservoelastic system.

More in general it is convenient to investigate the behaviour of the eigenvalues of the aeroservoelastic system $s = \sigma + \boldsymbol{i}\omega$ as a function of a parameter defining the flight condition, e.g. the flight velocity V_∞. It is then necessary to solve the following homogeneous system of algebraic equations:

$$\left(s^2 \, [\, \mathbf{M} \,] + s \, [\, \mathbf{C} \,] + [\, \mathbf{K} \,] - [\, \boldsymbol{H}_{am}(p) \,] \right) \{\boldsymbol{q}\} = 0, \tag{2.63}$$

with non-trivial solutions only if matrix $[\, \mathbf{A}(s, V_\infty) \,]$ is singular. Such a problem is closed in the unknowns σ and ω provided that flight velocity V_∞ is assigned a priori. By means of a suitable root-tracking procedure, which is easily initialized at $V_\infty = 0$ when the frequencies, dampings and corresponding eigenvectors correspond to those of the structural sub-system alone, it is possible to build/draw the root locus of the aeroservoelastic system as a function of the free parameter V_∞. Conventionally such information is summarized in $V_\infty - \omega$ and $V_\infty - g$ diagrams shown in Figure 2.10 where the damping factor g is defined as follows: $g = 2\xi = 2\sigma/\sqrt{\omega^2 + \sigma^2}$.

The primary challenge associated with flutter analysis is that, unless a quasi-steady approximation is considered viable, the aerodynamic transfer functions matrix $[\, \boldsymbol{H}_{am}(p) \,] = [\, \boldsymbol{H}_{am}(\boldsymbol{i}k) \,] = [\, \boldsymbol{H}_{am}(k) \,]$ is computed numerically along the imaginary axis $\mathbb{I}m$ of the complex vector space $\mathbb{C}$ and it is not known as an analytical function of the complex reduced frequency p. Therefore Eq. (2.63) is not a classical eigenvalues-eigenvectors problem but it is necessary to resort to the following dedicated numerical methods:

PK method: As discussed above the aerodynamic transfer functions matrix $[\, \boldsymbol{H}_{am}(p) \,]$ is computed numerically along the imaginary axis $\mathbb{I}m$ of the complex vector space $\mathbb{C}$ for $p = \boldsymbol{i}k$. However it yields a satisfactory approximation also for small dampings, namely for $p = \varepsilon + \boldsymbol{i}k$ with $\varepsilon \ll 1$. Such an argument holds near-by the flutter velocity V_F. If we now assume that the aerodynamic transfer functions matrix $[\, \boldsymbol{H}_{am}(p) \,]$ is analytical in $p = 0$, it is possible to expand it in Taylor series about $p_0 = \boldsymbol{i}k_0$ as follows:

$$[\, \boldsymbol{H}_{am}(p) \,] \simeq [\, \boldsymbol{H}_{am}(k_0) \,] + [\, \boldsymbol{H}'_{am}(k_0) \,](p - \boldsymbol{i}k_0) + [\, \boldsymbol{H}''_{am}(k_0) \,] \frac{(p - \boldsymbol{i}k_0)^2}{2} \tag{2.64}$$

It is convenient to consider no more than three terms in the Taylor series expansion in order not to break the symmetry between the aerodynamic and structural sub-systems. Such a procedure is similar to the quasi-steady approximation of the aerodynamic sub-system and solves the problem of how to "extrapolate" the aerodynamic database from the imaginary axis $\mathbb{I}m$ to the whole complex vector space $\mathbb{C}$ (or in other terms how to "translate" k to p). Therefore Eq. (2.63) becomes a classical eigenvalues-eigenvectors problem. However it is important to carefully monitor the so-called "alignment", e.g. by means of an iterative procedure for re-evaluating the Taylor series expansion until the mean value of the eigenvalues of the aeroservoelastic system is suitably close to the reference reduced frequency k_0.

Non-linear method: The flutter problem of Eq. (2.63) can be interpreted as a system of N_s non-linear homogeneous equations with the N_s elements of the eigenvector $\{\boldsymbol{q}\}$ and the 1 eigenvalue s as unknowns. Since the eigenvectors are defined up to a multiplicative constant, it is possible to add 1 normalization equation (suitably weighted by means of the matrix $[\,\mathbf{W}\,] \in \mathbb{R}^{N_s \times N_s}$) in order to close the problem, namely:

$$\begin{cases} [\,\mathbf{A}(s, V_\infty)\,]\{\boldsymbol{q}\} = 0 \\ \dfrac{1}{2}\{\boldsymbol{q}\}^{\mathsf{T}}[\,\mathbf{W}\,]\{\boldsymbol{q}\} = 1. \end{cases} \tag{2.65}$$

Such a system of non-linear equations can be efficiently solved by means of the modified Newton-Raphson numerical method. Performing the linearization of Eq. (2.65) about the reference solution $\{\boldsymbol{q}_0\}$ and s_0 and carrying out all the computations it is finally possible to write:

$$\begin{bmatrix} [\,\mathbf{A}(s_0, V_\infty)\,] & \left.\dfrac{\partial[\,\mathbf{A}(s, V_\infty)\,]}{\partial s}\right|_{s_0}\{q_0\} \\ \{\boldsymbol{q}_0\}^{\mathsf{T}}[\,\mathbf{W}\,] & 0 \end{bmatrix} \begin{Bmatrix} \{\Delta\boldsymbol{q}\} \\ \Delta s \end{Bmatrix} = \begin{Bmatrix} -[\,\mathbf{A}(s_0, V_\infty)\,]\{\boldsymbol{q}_0\} \\ 1 - \dfrac{1}{2}\{\boldsymbol{q}_0\}^{\mathsf{T}}[\,\mathbf{W}\,]\{\boldsymbol{q}_0\} \end{Bmatrix}.$$

The present numerical method returns in output both the eigenvector $\{\boldsymbol{q}\}$ and the eigenvalue s of the aeroservoelastic system for any input flight velocity V_∞. It is straightforward to assembly a root-tracking procedure, which is initialized at $V_\infty = 0$ when the frequencies, dampings and corresponding eigenvectors correspond to those of the structural sub-system alone, in order to automatically build/draw the $V_\infty - \omega$ and $V_\infty - g$ diagrams without issues at intersections between different curves.

In order to tackle more challenging aeroservoelastic dynamic problems, such as the design of active control systems e.g. for flutter suppression or gust/turbulence loads alleviation, it is convenient to resort to the state-of-the-art analysis and design tools within the framework of Control Theory (CT). Therefore the availability of a state-space representation in the time domain of the aerodynamic sub-system is highly desirable. We speak of "modern" aeroservoelasticity in order to stress the recent shift from the frequency domain to the time domain. For instance the flutter problem is easily solved with the command `eig` in MatLab or equivalently SciLab syntax.

Focusing for simplicity only the contribution of the generalized aerodynamic forces due to the structural displacements, it is possible to write the following Linear Time-Invariant (LTI) state-space representation of the aerodynamic sub-system in the time domain:

$$\begin{cases} \{\dot{\boldsymbol{x}}_a\} &= [\,\mathbf{A}_a\,]\{\boldsymbol{x}_a\} + [\,\mathbf{B}_a\,]\{\boldsymbol{q}\} \\ \{\boldsymbol{Q}^a\} &= [\,\mathbf{C}_a\,]\{\boldsymbol{x}_a\} + [\,\mathbf{D}_a\,]\{\boldsymbol{q}\}, \end{cases} \tag{2.66}$$

where the matrices $[\,\mathbf{A}_a\,]$, $[\,\mathbf{B}_a\,]$, $[\,\mathbf{C}_a\,]$ and $[\,\mathbf{D}_a\,] \in \mathbb{R}^{N_s \times N_s}$ are a possible realization of the aerodynamic sub-system (the matrices are square in this particular case, assuming without more information available the order of the aerodynamic sub-system to be equal to the number of structural d.o.f.) and $\{\boldsymbol{x}_a(t)\}$ is the array of the state variables. Such a state-space representation of the aerodynamic sub-system is not strictly proper because of the residualization of the high-frequency dynamics. The quality of the results is conveniently increased by broadening the dynamical residualization up to three terms (and no more in order not to break the symmetry with the structural sub-system) as follows:

$$\{\boldsymbol{Q}^a\} = [\,\mathbf{C}_a\,]\{\boldsymbol{x}_a\} + [\,\mathbf{D}_{a,\,0}\,]\{\boldsymbol{q}\} + \frac{L_a}{V_\infty}[\,\mathbf{D}_{a,\,1}\,]\{\dot{\boldsymbol{q}}\} + \frac{L_a^2}{V_\infty^2}[\,\mathbf{D}_{a,\,2}\,]\{\ddot{\boldsymbol{q}}\}. \tag{2.67}$$

The unknown matrices $[\,\mathbf{A}_a\,]$, $[\,\mathbf{B}_a\,]$, $[\,\mathbf{C}_a\,]$, $[\,\mathbf{D}_{a,\,0}\,]$, $[\,\mathbf{D}_{a,\,1}\,]$, $[\,\mathbf{D}_{a,\,2}\,]$ are computed by means of a suitable model identification/updating strategy, with the objective of minimizing the norm of the matrix $[\,\boldsymbol{\varepsilon}\,]$ of the residuals between the the transfer functions matrix of the state-space representation of Eq. (2.67) and the aerodynamic database already available from numerical simulations or experimental campaigns, namely:

$$[\,\boldsymbol{\varepsilon}\,] = [\,\mathbf{C}_a\,]\,(\,[\,\mathbf{I}\,]p - [\,\mathbf{A}_a\,]\,)^{-1}\,[\,\mathbf{B}_a\,] + [\,\mathbf{D}_{a,\,0}\,] + [\,\mathbf{D}_{a,\,1}\,]p + [\,\mathbf{D}_{a,\,2}\,]p^2 - [\,\boldsymbol{H}_{am}(p)\,]. \tag{2.68}$$

Assuming that the aerodynamic sub-system is asymptotically stable and with non-oscillatory outputs (as verified experimentally), it is possible to significantly simplify the model identification/updating problem by assigning a priori a diagonal structure with purely real stable eigenvalues $s \in \mathbb{R}^-$ to the matrix $[\,\mathbf{A}_a\,]$. Other parametrization strategies (with different trade-offs between accuracy and computational overhead) are also available. Finally it is worthwhile to remark that the time domain is the ideal framework for investigating and/or identifying model non-linearities. Under the assumption of weak non-linearities a general non-linear input is approximated with its Taylor series expansion. This corresponds to assigning a priori the structure of the non-linearities.

3

Dynamic mesh handling

This Chapter provides an overview of the background for dynamic mesh handling within the framework of OpenFOAM software and then illustrates the motivation for designing and implementing a novel mesh deformation strategy, particularly suited for the aeroservoelastic analysis of free-flying deformable aircraft. More in particular in §3.1 some challenging applications closely related to mesh deformation are surveyed, together with the tools already available within the framework of OpenFOAM software to tackle such problems. Particular focus is dedicated to the Geometric Conservation Law (GCL) which can be interpreted as a link between mathematical models and numerical methods (and therefore programming tools). Successively in §3.2 a novel mesh deformation strategy is presented, stressing the hierarchical nature of the algorithm and the advantages when dealing with the aeroservoelastic analysis of free-flying deformable aircraft. The serial and parallel performances are compared to those of more classical mesh deformation options. Finally in §3.3 the robustness of the algorithm and the quality of the results are benchmarked by tackling a series of test problems of increasing complexity.

3.1 Background

In many challenging applications within the framework of continuum mechanics, one or many of the boundaries delimiting the physical domain of the problem move in time. When such moving boundaries experience large displacements and rotations, or when they undergo large deformations, it becomes necessary to solve the flow problem on a moving and possibly deforming grid. Such a grid is often referred to in literature as a "dynamic mesh". [27] Maybe the most obvious examples include Fluid-Structure Interaction (FSI) problems such as: the aeroservoelastic analysis of maneuvering aircraft with particular focus on transonic flutter, aileron buzz and buffeting phenomena and/or the study of the unsteady blood flow in the deformable or aging arteries and veins of the human body in order to assist the hands of modern surgeons.

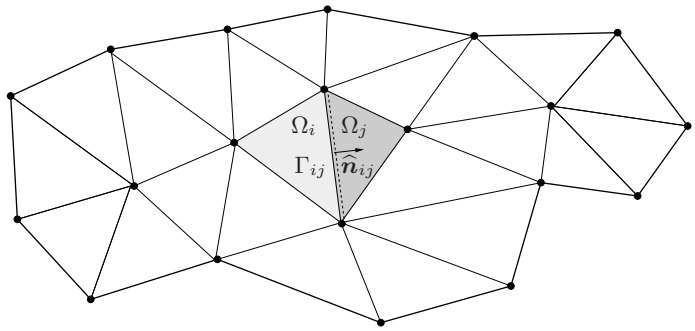

Figure 3.1: Example of a conformal triangular mesh $\mathcal{M}$.

Other "hot" topics include the simulation of ice accretion on the wings of aircraft flying through rain, with the aim of better understanding the hazards associated with the dynamically changing shape of the airfoil because of ice, and the design of innovative "optimal" sails. Finally the availability of efficient, flexible and robust mesh deformation tools is an important asset when dealing with morphing and/or shape optimization problems since deforming the mesh may deliver significant time savings with respect to remeshing. Another non-conventional example stems from Computer Generated Imaginery (CGI) and videogames: in such a case the mesh deformation algorithm must meet the efficiency requirements of real-time simulations.

In order to numerically solve a problem governed by a system of Partial Differential Equations (PDE), e.g. the mathematical models for the structural and aerodynamic sub-systems presented in Chapter 2, first of all it is necessary to discretize the physical domain of the problem. Such a task is straightforward when dealing with the time domain $\mathcal{T} \subseteq \mathbb{R}^+$, which is conveniently approximated by means of a set of time instants, e.g. $t^{(n)} = n\,\Delta t$ in the case of constant timestep Δt. On the contrary for the approximation of the space domain $\mathcal{V} \subseteq \mathbb{R}^{N_d}$ it is necessary to build a so-called mesh, that is a set of geometrical points and topological entities such as edges, faces and cells (also referred to as connectivity). A number of algorithms are available within the fruitful research field of automatic mesh generation to efficiently and automatically perform such a complex task, e.g. structured or unstructured and more recently castellated mesh generation algorithms. [38, 68, 93] With reference to Figure 3.1 the mesh $\mathcal{M}$ must satisfy the following requirements:

a) $\overline{\mathcal{V}}_h = \bigcup_{\Omega_i \in \mathcal{M}} \Omega_i$ where $\overline{\mathcal{V}}_h$ is the closure of the approximated space domain $\mathcal{V}_h$;

b) $\mathring{\Omega}_i \neq \emptyset \quad \forall\, \Omega_i \in \mathcal{M}$ where $\mathring{\Omega}_i = \Omega_i \backslash \partial\Omega_i$, i.e. there are no cells of zero measure;

c) $\mathring{\Omega}_i \cap \mathring{\Omega}_j = \emptyset \quad \forall\, \Omega_i,\, \Omega_j \in \mathcal{M}$ where $\Omega_i \neq \Omega_j$, i.e. different cells cannot overlap;

d) if $\Gamma_{ij} = \Omega_i \cap \Omega_j \neq \emptyset$ where $\Omega_i \neq \Omega_j$ then Γ_{ij} must correspond to a point or to an edge or to a face shared by cells Ω_i e Ω_j, i.e. such a mesh is called conformal.

Finally it is useful to define the measure operator $|\cdot|$ which applied to a cell Ω_i returns in output its volume $|\Omega_i|$ and applied to a face Γ_{ij} returns in output its area $|\Gamma_{ij}|$. Another important metric quantity is the normal unit vector $\widehat{\boldsymbol{n}}_{ij}$ associated with each face Γ_{ij}. On the boundary such a normal unit vector is conventionally assumed positive when pointing outside the fluid domain.

Within the framework of an Arbitrary Lagrangian Eulerian (ALE) kinematical description of the continuum, the mesh is not constant with time but it is subject to a general translation-rotation and deformation displacement field. The motion of the fluid domain can be either known a priori (such as in the case of forced pitch/plunge oscillations of an airfoil) or it can be the output returned by the structural subsystem (such as in the case of FSI problems). With reference to Figure 3.2 the mesh deformation problem can be stated very simply as follows: given a general displacements field between the reference and current configurations on each j-th boundary node $\Delta\boldsymbol{x}_{b,\,j}$ with $j \in [1,\, N_{a,\,b}]$, compute the corresponding displacements field of each k-th volume node $\Delta\boldsymbol{x}_{v,\,k}$ with $k \in [1,\, N_{a,\,v}]$. It is worthwhile to remark that the overall mesh quality, the computational cost and the parallel scalability are Key Performance Indicators (KPI) to assist the user in the choice of the most suitable mesh deformation strategy.

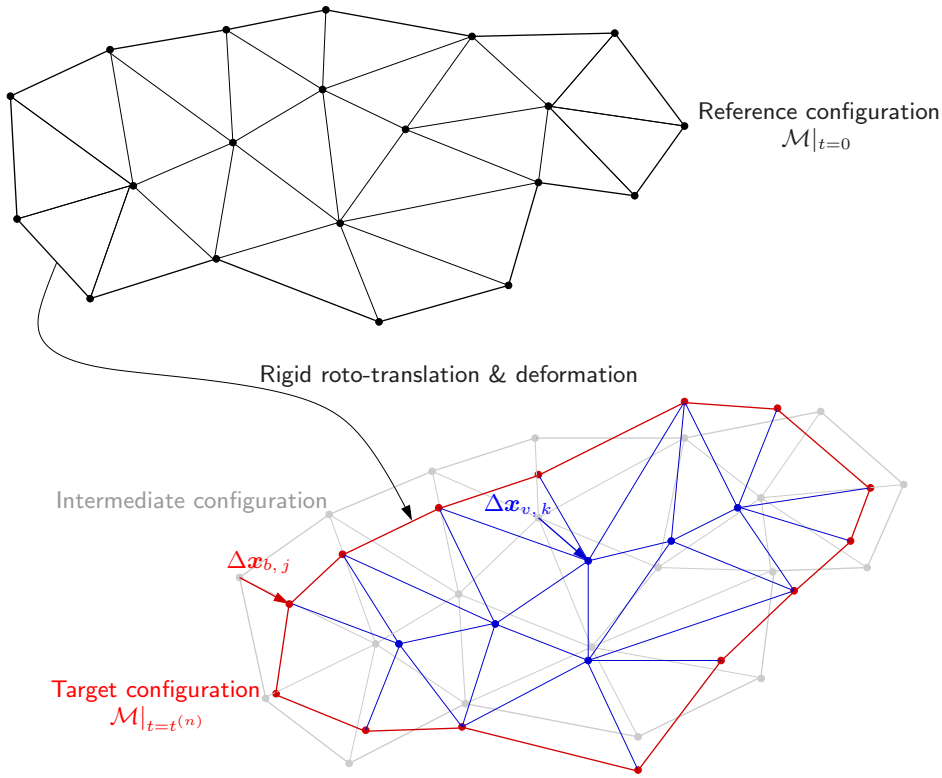

Figure 3.2: Mesh deformation problem with focus on the rigid and deformative components.

A significant body of research has been performed in the area of grid motion schemes, e.g. for aeroservoelastic analysis. These range from simple algebraic shearing methods to those that model the vehicle and the surrounding grid as a physical field equation that can be coupled with the analysis. [76] Some of the most appealing strategies are: explicit or implicit laplacian smoothing [42], numerical methods based on the continuum analogy between the computational grid and an elastic solid [16] and multivariate interpolation schemes ranging from Radial Basis Functions (RBF) [11] to Inverse Distance Weighting (IDW). [91] Moreover, when dealing with e.g. the relative motion between rotor blades and fuselage in a complete helicopter configuration, dedicated numerical techniques such as the overlapping grid Chimera method [6, 8] or the Generic Grid Interface (GGI) approach are required. [79] In cases of extreme shape change mesh motion alone is not sufficient to accommodate boundary deformation. Mesh topology, connectivity and resolution needs to be adapted, e.g. by means of an automatic tetrahedral edge/face swapping technique or the mesh needs to be locally regenerated. [43] However all these options differ significantly in terms of accuracy, robustness and (parallel) efficiency.

3.1.1 Geometric Conservation Law

Within the framework of an Arbitrary Lagrangian Eulerian (ALE) kinematical description of the continuum, a numerical scheme designed for solving the flow equations on moving grids typically incurs in the computation of metric quantities involving the grid points positions and velocities. When using the cell-centered space discretization operators of the Finite-Volume (FV) method, possible examples of metric quantities depending on the grid point positions are the cell volumes $|\Omega_i|^{(n)}$, face areas $|\Gamma_{ij}|^{(n)}$ and normal unit vectors $\widehat{\boldsymbol{n}}_{ij}^{(n)}$ associated to the deformed configuration at time $t^{(n)}$. Moreover it is necessary to suitably evaluate the local face velocities $\mathbf{v}_{ij}^{(n)}$.

The time integration between time instants $t^{(n)}$ and $t^{(n+1)}$ raises the issue of where or better when to evaluate the metric quantities and fluxes: on the mesh configuration at $t = t^{(n)}$, or on that at $t = t^{(n+1)}$, or in between these two configurations, or outside these two configurations, or using a combination of all these mesh configurations? A useful guideline for evaluating these quantities as well as time-integrating fluxes on moving grids is provided by the enforcement of the Geometric Conservation Law (GCL) or its Discrete counterpart (DCGL). This law states that the computation of the metric quantities depending on the grid points positions and velocities must be performed in such a way that, independently of the mesh motion, the resulting numerical scheme preserves the state of a constant and uniform flow. [27]

There has been sufficient numerical evidence showing that satisfying the DGCL improves considerably the time-accuracy of numerical computations on moving grids. However, for some applications, it has also been reported that respecting or violating the DGCL produced the same numerical results and delivered the same computational performance. For this reason the following questions have been frequently asked: a) why should one pay special attention to a uniform flow field and b) why should a scheme compute exactly such a particular solution when it only approximates the real flow-field? In order to answer the above two questions, a theoretical investiga-

tion of the DGCL has been carried out with the important proof that, for a given scheme that is p-order time-accurate on a fixed mesh, satisfying the corresponding p-discrete geometric conservation law is a sufficient condition for this scheme to be at least first-order time-accurate on a moving mesh. In other terms the requirement of computing exactly a uniform field on a moving grid is closely related to an accuracy condition, or at least a consistency condition. Moreover it is possible to prove that the DGCL requirement corresponds to a necessary and sufficient condition for a numerical scheme to preserve the non-linear stability properties of its fixed grid counterpart. It is worthwhile to remark that we define stability mainly in terms of spurious oscillations and overshoots. In that sense, nonlinear stability becomes especially vital at shocks and contact discontinuities, which tend to create large spurious oscillations in otherwise stable and monotone solutions.

Eventually the Geometric Conservation Law (GCL) can be interpreted as the following relationship between the rate of change of the volume of the spatial domain $\mathcal{V}(t) \subseteq \mathbb{R}^{N_d}$ and the velocity $\mathbf{v}(\boldsymbol{x}, t)$ of its moving boundary $\mathcal{S}(t) = \partial\mathcal{V}(t) \subseteq \mathbb{R}^{N_d-1}$ with the normal unit vector $\widehat{\boldsymbol{n}}(\boldsymbol{x}, t)$ pointing outside the fluid domain:

$$\frac{\mathrm{d}}{\mathrm{d}t} \int_{\mathcal{V}(t)} \mathrm{d}\mathcal{V} = \oint_{\mathcal{S}(t)} \mathbf{v} \cdot \widehat{\boldsymbol{n}} \, \mathrm{d}\mathcal{S}. \tag{3.1}$$

Within the framework of Finite-Volume (FV) space discretization operators, if we now choose without loss of generality a forward Euler explicit time integration scheme, it is possible to derive the discrete counterpart of Eq. (3.1) focusing on the i-th cell $\Omega_i(t)$ delimited by the boundary faces $\Gamma_{ij}(t)$ as follows:

$$\frac{|\Omega_i|^{(n+1)} - |\Omega_i|^{(n)}}{\Delta t} = \sum_{j \in \mathscr{B}(\Omega_i)} \mathsf{v}_{ij}^{(n)} \, |\Gamma_{ij}|^{(n)}, \tag{3.2}$$

where $\mathscr{B}(\Omega_i)$ is the bubble of each j-th cell Ω_j sharing the face Γ_{ij} with i-th cell Ω_i (or from a programmer's perspective the i-th row of the cell-cell connectivity matrix) and $\mathsf{v}_{ij}^{(n)}$ is the normal component of the velocity associated with face Γ_{ij} at time $t^{(n)}$. Eq. (3.2) is an operative way to derive a DGCL-compliant form of the mesh velocity, namely:

$$\mathsf{v}_{ij}^{(n)} = \frac{|\Delta\Omega_{ij}|}{|\Gamma_{ij}|^{(n)} \, \Delta t}, \tag{3.3}$$

where $|\Delta\Omega_{ij}|$ is the volume swept by face Γ_{ij} between time instants $t^{(n)}$ and $t^{(n+1)}$ and it can be easily evaluated numerically. It is possible to prove that the same argument is valid for a more general first and second order explicit as well as implicit time integration scheme such as the θ-method, recovering the first order forward Euler explicit scheme for $\theta = 0$, the first order backward Euler implicit scheme for $\theta = 1$ and the second order Crank-Nicolson implicit scheme for $\theta = 1/2$. For arbitrary time integration schemes a similar procedure is followed. The problem becomes much more complex when topological mesh changes (e.g. those associated with tetrahedral face/edge swapping) are also taken into account. [39]

3.2 A hierarchy of mesh deformation tools

Once the structural displacements and velocities are suitably interpolated by means of the aeroelastic interface operator, it is necessary to tackle the problem of adjusting the internal aerodynamic mesh to the newly computed boundary nodes in such a way that grid quality is not degraded significantly, e.g. with non-negative cell volumes, moderate levels of stretching and non-orthogonality. This task of moving what can amount up to millions of nodes is to be performed thousand of times during an aeroservoelastic computation. Therefore the availability of efficient, massively parallel and robust mesh deformation tools and topology modifiers is crucial.

In order to achieve the best compromise between the opposing requirements of accuracy, robustness and (parallel) efficiency we propose a novel hierarchical mesh deformation strategy, based on a modified version of the Inverse Distance Weighting (IDW) multivariate interpolation kernel, and particularly suited for aeroservoelastic static and dynamic simulation of free flying aircraft.

The basic idea consists of adding in the kinematical description of the grid motion a convenient intermediate frame between the reference and target configurations. As shown in Figure 3.2 the problem can be decomposed in the identification of the generally-speaking "big" rigid rotation-translation contribution between the reference and intermediate configurations and in update of the internal aerodynamic mesh to the residual generally-speaking "small" elastic displacement field of the boundary nodes with a small effort and improved robustness. Such a procedure is somehow similar to the approach for rewriting the structural problem in a mean axes floating reference frame by decoupling the rigid and elastic d.o.f. associated with flight mechanics and aeroservoelasticity respectively. More in particular it is possible to subdivide the grid motion process in the following steps:

a) Using the information about the interpolated structural displacements field $\Delta\boldsymbol{x}_j$ relative to the reference undeformed configuration $\boldsymbol{x}_j$ of each j-th solid boundary d.o.f. we first identify by means of a Weighted Least Squares (WLS) strategy (e.g. using the boundary face areas as normalization factors) only the "rigid" translation-rotation part of the overall general big displacements field as follows:

$$\Delta\boldsymbol{x}_j = \mathbf{s} + \mathbf{T}\,\boldsymbol{x}_j + \boldsymbol{\varepsilon}_j = \mathbf{s} + (\mathbf{R} - \mathbf{I})\,\boldsymbol{x}_j + \mathbf{D}\,\boldsymbol{x}_j + \boldsymbol{\varepsilon}_j \qquad \forall \quad j \in [1,\, N_{a,\,b}] \quad (3.4)$$

Actually with Eq. (3.4) we identify the mean translation vector $\mathbf{s}$ and linear map tensor $\mathbf{T}$. In fact this choice leads to a much more easier implementation with respect to the identification of the mean rotation tensor $\mathbf{R}$ since it is not necessary to include within the formulation the orthogonality constraints $\mathbf{R}^{\mathsf{T}}\,\mathbf{R} = \mathbf{I}$ by means of Lagrange multipliers. This would imply a non-linear problem unnecessarily more costly to solve. The same result can be retrieved a posteriori using the Euler-Rodriguez formula to split the mean rotation tensor $\mathbf{R}$ in an emisymmetric contribution $\mathbf{E}$ and in a symmetric contribution $\mathbf{S}$:

$$(\mathbf{R} - \mathbf{I}) = \sin\varphi\,\mathbf{K}_\times + (1 - \cos\varphi)\,\mathbf{K}_\times\mathbf{K}_\times = \mathbf{E} + \mathbf{S}, \quad (3.5)$$

where φ and $\widehat{\boldsymbol{k}}$ are respectively the magnitude and the direction of the rotation vector $\boldsymbol{\psi} = \varphi\,\widehat{\boldsymbol{k}}$ while $\mathbf{K}_\times$ is the emisymmetric tensor representing the linear cross-product operator $\widehat{\boldsymbol{k}}\times$. If we now require that the emisymmetric part of the linear map tensor $\mathbf{T}$ matches $\mathbf{E}$, that is: $\mathbf{E} = (\mathbf{T}-\mathbf{T}^\mathsf{T})/2$, it is straightforward to retrieve $\boldsymbol{\psi}$ and assembly $\mathbf{R}$ with Eq. (3.5). The limit of such a procedure lies in the fact that the residual linear deformation tensor $\mathbf{D} = \mathbf{T} - (\mathbf{R} - \mathbf{I})$ is always symmetric, that is in the case of a pure shear deformation we would identify a dummy mean rotation with a symmetric deformation about it. However this does not affect the accuracy of the results. Such a WLS identification procedure is very flexible and its credibility as a stand-alone mesh deformation tool can be significantly increased by adding a set of higher-order kernels or global shape function to describe the mesh motion, namely:

$$\Delta\boldsymbol{x}_j = \mathbf{s} + \mathbf{T}\,\boldsymbol{x}_j + \sum_{k=1}^{N_h} \mathbf{H}_k\,\psi_k(\boldsymbol{x}_j)\,\boldsymbol{x}_j + \boldsymbol{\varepsilon}_j \qquad \forall \quad j \in [1,\, N_{a,\,b}], \tag{3.6}$$

where $\mathbf{H}_k$ is the k-th higher-order tensor and $\psi_k(\boldsymbol{x})$ is the corresponding global shape function. The global shape functions are in the form: $\psi_k(\boldsymbol{x}) = \|\boldsymbol{x}-\boldsymbol{p}_k\|^{q_k}$, where $\boldsymbol{p}_k$ is the k-th control point and q_k is the order of the selected polynomial kernel. Such an add-on yields an exact identification (i.e. with zero residuals) of a weakly non-linear deformation displacement field. In order not to incur into stability issues it is recommended to limit the maximum order of the global shape functions.

It is worthwhile to remark that only boundary nodes belonging to solid walls are used for the identification procedure. Therefore all the other nodes such as those belonging to asymptotic/freestream boundaries are not constrained but follow the "big" displacements of the rigid aircraft, e.g. those generally-speaking connected with flight mechanics.

b) As a result of the identification procedure the internal aerodynamic mesh must be adjusted only to the smaller residual $\boldsymbol{\varepsilon}_j$ of each j-th boundary d.o.f., with a computational effort which can also be expected to be significantly smaller. In the case of a posteriori recovery of the mean rotation tensor $\mathbf{R}$ the linear deformation tensor contribution $\mathbf{D}\,\boldsymbol{x}_j$ must also be accounted for. This "small" contribution is that generally-speaking connected with aeroelasticity. Rather than using algorithms that require solving a system of equations (expensive in terms of computational cost and memory occupation for realistic simulations), we choose an explicit mesh deformation technique based on the Inverse Distance Weighting (IDW) multivariate interpolation scheme. For each k-th internal d.o.f. the displacement $\Delta\boldsymbol{x}_k$ relative to the reference undeformed configuration $\boldsymbol{x}_k$ can be evaluated by performing the following matrix-array multiplication:

$$\Delta\boldsymbol{x}_k = \sum_{j=0}^{N_{a,\,b}} \frac{\mathbf{IDW}_{(k,\,j)}}{|\mathbf{IDW}_{(k,\,:)}|}\,\boldsymbol{\varepsilon}_j \qquad \forall \quad k = [1,\, N_{a,\,v}], \tag{3.7}$$

with the interpolation kernel $\mathbf{IDW}_{(k,\,j)} = \|\boldsymbol{x}_k - \boldsymbol{x}_j\|^{-p}$. The parameter p can be used as a knob to adjust the size of the computational stencil and therefore the smoothness of the results. As it is, this strategy can be either time-efficient or memory-efficient, depending on whether matrix $\mathbf{IDW}$ is computed only once in the pre-processing stage and then stored with a large memory overhead. In order to achieve the best trade-off we propose a simple and effective modification to the original interpolation algorithm called Sparse Inverse Distance Weighting (SIDW) in which matrix $\mathbf{IDW}$ is stored in Compressed Sparse Column (CSC) format as follows:

$$\mathbf{SIDW}_{(k,\,j)} = \mathbf{IDW}_{(k,\,j)} \qquad \text{if} \qquad \frac{\mathbf{IDW}_{(k,\,j)}}{|\mathbf{IDW}_{(k,\,:)}|} > \xi \tag{3.8}$$

where ξ is a threshold parameter to be set by the user. However if its value is too large and there is not any active j-th column for k-th row, it is iteratively doubled until a safe number of active columns per row is reached. This is somehow similar to modified Sheperd's method but it is simpler to implement since it does not require any fast spatial search structure. [78] This method is very powerful also because it dos not require any knowledge of the connectivity of the mesh and it is especially suited for a straightforward parallelization as it is not susceptible to implementation issues such as in the case of shared nodes among many processors.

c) An alternative, less general but efficient strategy relies on a modification of the non-compenetration boundary conditions $\boldsymbol{v} \cdot \widehat{\boldsymbol{n}} = 0$ on solid walls for the mathematical model of the Euler equations. The geometric and kinematic effects of a given, both rigid and deformative, small displacement law can be simulated simply adding the so-called "transpiration" velocity parallel to the boundary normal unit vector, without deforming the mesh at all. Let us suppose that the following parametric description of the body deformed configuration $\boldsymbol{x}(\xi, \eta, t)$ and velocity $\boldsymbol{v}(\xi, \eta, t)$ are available as functions of the reference undeformed configuration $\boldsymbol{x}_0(\xi, \eta)$, flight velocity $\boldsymbol{V}_\infty$ and small structural displacements $\boldsymbol{s}(\xi, \eta, t)$, namely:

$$\boldsymbol{x} = \boldsymbol{x}_0 - \boldsymbol{V}_\infty\, t + \boldsymbol{s} \qquad \text{and} \qquad \boldsymbol{v} \equiv \frac{\mathrm{d}\boldsymbol{x}}{\mathrm{d}t} = -\boldsymbol{V}_\infty + \dot{\boldsymbol{s}}. \tag{3.9}$$

Again let us write the following first order expansion of the deformed normal unit vector $\widehat{\boldsymbol{n}}(\xi, \eta, t)$ about the reference undeformed normal unit vector $\widehat{\boldsymbol{n}}_0(\xi, \eta, t)$, namely:

$$\widehat{\boldsymbol{n}} \equiv \frac{\boldsymbol{x}_{/\xi} \times \boldsymbol{x}_{/\eta}}{\|\boldsymbol{x}_{/\xi} \times \boldsymbol{x}_{/\eta}\|} = \widehat{\boldsymbol{n}}_0 + \Delta\widehat{\boldsymbol{n}} + \mathcal{O}(\boldsymbol{s}^2). \tag{3.10}$$

Setting to zero the local velocity vector projected along the deformed normal unit vector and highlighting all the terms depending on the small structural displacements we finally obtain the following linear(ized) formulation of the transpiration velocity:

$$\mathsf{v} = -\boldsymbol{V}_\infty \cdot \Delta\widehat{\boldsymbol{n}} \,+\, \dot{\boldsymbol{s}} \cdot \widehat{\boldsymbol{n}}_0 + \mathcal{O}(\boldsymbol{s}^2). \tag{3.11}$$

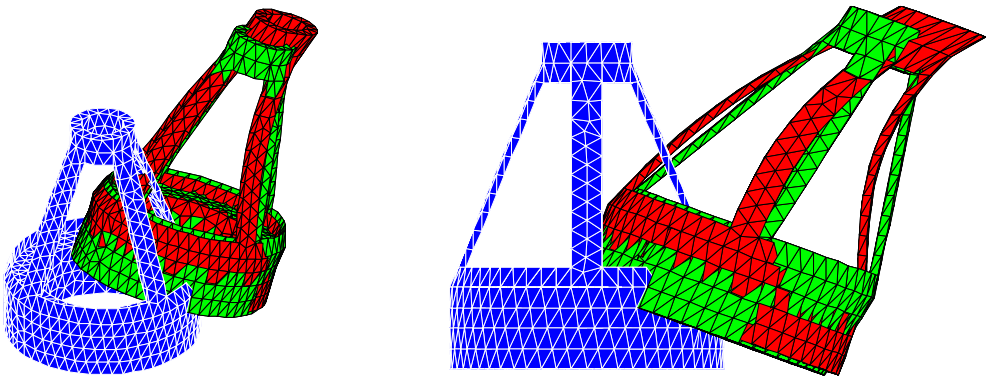

a) WLS identification of the translation vector **s** and the linear map tensor **T**.

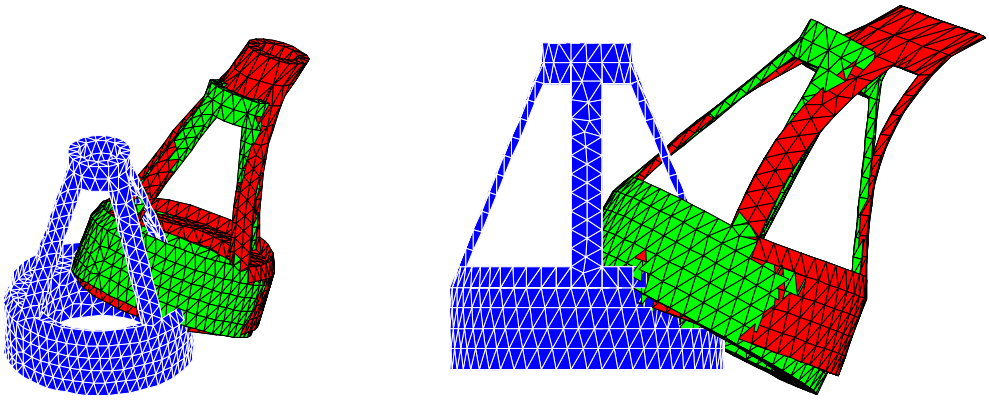

b) A-posteriori recovery of the rotation tensor **R** using the Euler-Rodriguez formula.

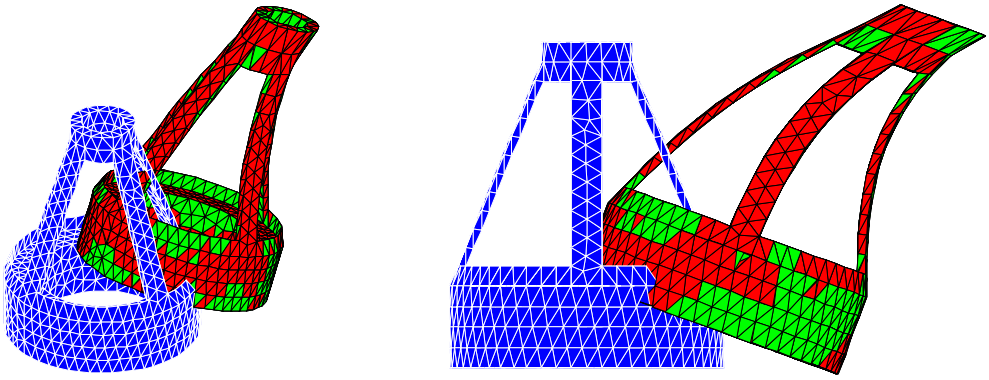

c) SIDW contribution from intermediate to target configurations with $\xi = 0.005$.

Figure 3.3: Example application to illustrate the algorithm of the proposed hierarchical mesh deformation toolbox: the reference (●) and target (●) configurations are highlighted, together with the intermediate (●) one.

This approach is equivalent to small perturbation boundary conditions often implemented by linear numerical methods and it has been successfully used also in the framework of high-fidelity mathematical models under the assumption of small displacements in order to relieve the effort of deforming the mesh. [80] Actually we implemented a modified non-linear formulation, in which the normal unit vector deformation is not computed analytically as in Eq. (3.10) but with a Finite Differences (FD) method and the mixed geometric-kinematic non-linear contribution $\dot{\boldsymbol{s}} \cdot \Delta\widehat{\boldsymbol{n}}$ is retained. Such a modification yields a wider validity interval in terms of free-stream Mach numbers M_∞, angles of attack α and thickness ratios t/c. [74]

It is remarkable that transpiration boundary conditions were first conceived by aeronautical engineers as a practical tool to overcome the drawbacks of ALE formulation (i.e. how to deform the mesh and compute the corresponding interface velocities and how to add such a contribution within the numerical fluxes) without modifying the source code of the aerodynamic solver but involving only modifications of the boundary conditions. [50] However it is possible to provide a solid mathematical justification to such a brilliant idea, by showing that adequate asymptotic expansions can reduce the problem to a standard one written on a fixed configuration, but using specific transpiration boundary conditions. [25] More in particular we want to show that such a formulation can be interpreted as a first-order linearization of the problem written in ALE form. Without loss of generality let us focus on the Euler equations governing the dynamics of a compressible, ideal fluid written within an Arbitrary Lagrangian Eulerian (ALE) framework in integral conservative form as follows:

$$\frac{\mathrm{d}}{\mathrm{d}t}\int_{\mathcal{V}(t)} \mathbf{u}\,\mathrm{d}\mathcal{V} + \oint_{\mathcal{S}(t)} \left[\mathbf{f}(\mathbf{u}) - \mathbf{u}\,\mathbf{v}\right] \cdot \widehat{\boldsymbol{n}}\,\mathrm{d}\mathcal{S} = 0 \tag{3.12}$$

just as in Eq. (2.43) but stripping out the viscous fluxes and with the usual non-compenetration boundary conditions on solid walls $\boldsymbol{v} \cdot \widehat{\boldsymbol{n}}|_{\mathcal{S}^w} = \mathbf{v} \cdot \widehat{\boldsymbol{n}}|_{\mathcal{S}^w} = \dot{\boldsymbol{s}} \cdot \widehat{\boldsymbol{n}}$. If we now assume that the motion of the boundary is small both in terms of displacements and velocities it is possible to rewrite the normal unit vector and the interface velocity associated with the deformed configuration as follows: $\widehat{\boldsymbol{n}} = \widehat{\boldsymbol{n}}_0 + \varepsilon\,\widehat{\boldsymbol{n}}_1 + \mathcal{O}(\varepsilon^2)$ and $\mathbf{v} = \dot{\boldsymbol{s}}_0 + \varepsilon\,\dot{\boldsymbol{s}}_1 + \mathcal{O}(\varepsilon^2)$ as functions of the undeformed configuration and a first-order variation multiplied by a small book-keeping parameter ε. Obviously in the undeformed configuration we have: $\dot{\boldsymbol{s}}_0 \equiv 0$. The infinitesimal volume and surface can be written as follows: $\mathrm{d}\mathcal{V} = \mathrm{d}\mathcal{V}_0 + \varepsilon\,\mathrm{d}\mathcal{V}_1$ and $\widehat{\boldsymbol{n}}\,\mathrm{d}\mathcal{S} = \widehat{\boldsymbol{n}}_0\,\mathrm{d}\mathcal{S}_0 + \varepsilon\,\widehat{\boldsymbol{n}}_1\,\mathrm{d}\mathcal{S}_1$ respectively. With a similar argument it is possible to expand the array of conservative variables as follows: $\mathbf{u} = \mathbf{u}_0 + \varepsilon\mathbf{u}_1 + \mathcal{O}(\varepsilon^2)$ and as a consequence we have: $\mathbf{f}(\mathbf{u}) = \mathbf{f}(\mathbf{u}_0) + \varepsilon\nabla\mathbf{f}(\mathbf{u}_0)\,\mathbf{u}_1 + \mathcal{O}(\varepsilon^2)$. If we now substitute in Eq. (3.12) and gather terms with equal orders of the book-keeping parameter ε, the problem becomes:

$$\begin{aligned}
\varepsilon^0 :&\quad \frac{\mathrm{d}}{\mathrm{d}t}\int_{\mathcal{V}_0} \mathbf{u}_0\,\mathrm{d}\mathcal{V}_0 + \oint_{\mathcal{S}_0} \mathbf{f}(\mathbf{u}_0) \cdot \widehat{\boldsymbol{n}}_0\,\mathrm{d}\mathcal{S}_0 = 0 \\
\varepsilon^1 :&\quad \frac{\mathrm{d}}{\mathrm{d}t}\int_{\mathcal{V}_0} \mathbf{u}_1\,\mathrm{d}\mathcal{V}_0 + \oint_{\mathcal{S}_0} \mathbf{u}_1\mathbf{A}(\mathbf{u}_0) \cdot \widehat{\boldsymbol{n}}_0\,\mathrm{d}\mathcal{S}_0 + \mathbf{R}(\mathbf{u}_0) = 0.
\end{aligned} \tag{3.13}$$

The equations of order $\mathcal{O}(\varepsilon^0)$ correspond to the Euler equations written in a fixed domain for the unknown mean flow-field $\mathbf{u}_0(\boldsymbol{x}, t)$, while the equations of order $\mathcal{O}(\varepsilon^1)$ represent a linear advection-reaction problem for the unknown perturbation flow-field $\mathbf{u}_1(\boldsymbol{x}, t)$ with the following given (i.e. the perturbation problem is addressed after the baseline one) advection and reaction fields:

$$\begin{aligned} \mathbf{A}(\mathbf{u}_0) &= \nabla \mathbf{f}(\mathbf{u}_0) \\ \mathbf{R}(\mathbf{u}_0) &= \frac{\mathrm{d}}{\mathrm{d}t} \int_{\mathcal{V}_1} \mathbf{u}_0 \, \mathrm{d}\mathcal{V}_1 + \oint_{\mathcal{S}_1} \mathbf{f}(\mathbf{u}_0) \cdot \widehat{\boldsymbol{n}}_1 \, \mathrm{d}\mathcal{S}_1 - \oint_{\mathcal{S}_0} \mathbf{u}_0 \, \dot{\boldsymbol{s}}_1 \cdot \widehat{\boldsymbol{n}}_0 \, \mathrm{d}\mathcal{S}_0. \end{aligned} \tag{3.14}$$

If we substitute the asymptotic expansions in the boundary conditions and gather terms with equal orders of the book-keeping parameter ε, it is possible to write:

$$\begin{aligned} \varepsilon^0 : &\qquad \boldsymbol{v}_0 \cdot \widehat{\boldsymbol{n}}_0|_{\mathcal{S}^w} = 0 \\ \varepsilon^1 : &\qquad \boldsymbol{v}_1 \cdot \widehat{\boldsymbol{n}}_0|_{\mathcal{S}^w} = \dot{\boldsymbol{s}} \cdot \widehat{\boldsymbol{n}}_0 - \boldsymbol{v}_0 \cdot \widehat{\boldsymbol{n}}_1. \end{aligned} \tag{3.15}$$

In conclusion it is possible to remark that the so-called transpiration approach is equivalent to mixing the problem of order $\mathcal{O}(\varepsilon^0)$ with the boundary conditions of order $\mathcal{O}(\varepsilon^1)$ by means of a suitable residualization of the dynamics of the perturbation solution.

Presently transpiration boundary conditions are automatically switched on to deal with residuals (if any) following to steps a) and b). For instance this is the case of control surfaces deflection which cannot always be reproduced accurately by means of mesh deformation techniques especially at the interface between moving and fixed components, e.g. at the interface between stabilator and fuselage. This small correction is favorable for the numerical prediction of control stability derivatives. [21]

With reference to Figure 3.3 the algorithm of the proposed hierarchical mesh deformation toolbox can be summarized by tackling the simple but representative test problem of adjusting the internal mesh of an arbitrary object given the reference configuration and the newly computed boundary nodes in the target configuration. The prescribed displacement field is made of both "big" rigid rotation-translation and "small" deformative (bending and stretching) contributions. It is worthwhile to compare the results of the Weighted Least-Squares (WLS) identification of the mean translation vector $\mathbf{s}$ and linear map tensor $\mathbf{T}$ with those of the a-posteriori recovery of the rotation tensor $\mathbf{R}$ using the Euler-Rodriguez formula. Not only the identification of the mean linear map tensor $\mathbf{T}$ is computationally more efficient than that of the rotation tensor $\mathbf{R}$ but the intermediate configuration is significantly closer to the target one. Therefore the additional effort requested to go from the intermediate to the target configuration can be expected to be smaller. In other terms the mesh quality after applying the Inverse Distance Weighting (IDW) interpolation can be expected to be higher, improving the robustness of the overall procedure. Finally we stress that the proposed Sparse Inverse Distance Weighting (SIDW) interpolation is effective also for relatively large values of the threshold parameter up to $\xi = 0.005$ thanks to the iterative procedure to suitably reshape the sparsity pattern.

3.2.1 Cost estimates

First of all it is worthwhile to perform a theoretical analysis of the serial and parallel Key Performance Indicators (KPI) such as memory occupation, computational cost and communication time. The results will be compared with the performances of a reference algorithm to tackle the mesh deformation problem such as a Finite Element (FE) numerical method based on the continuum analogy between the computational grid and an elastic solid, which is among the most widely used viable options today within the framework of Fluid-Structure Interaction (FSI) applications. Surveying once again the various steps of the grid motion process it is possible to write:

a) The Weighted Least-Squares (WLS) identification procedure requires to solve an over-determined linear problem in the following form: $[\,\mathbf{A}\,]\{\mathbf{w}\} = \{\Delta\boldsymbol{x}\}$ where $[\,\mathbf{A}\,] \in \mathbb{R}^{N_{a,\,b} \times N_w}$ is a suitable influence matrix while all the components of the unknown translation vector $\mathbf{s}$ and linear map tensor $\mathbf{T}$ are packed in the array of the N_w unknowns $\mathbf{w} = \{\mathsf{s}_x, \mathsf{s}_y, \mathsf{s}_z, \mathsf{T}_{xx}, \mathsf{T}_{xy}, \mathsf{T}_{xz}, \mathsf{T}_{yx}, \mathsf{T}_{yy}, \mathsf{T}_{yz}, \mathsf{T}_{zx}, \mathsf{T}_{zy}, \mathsf{T}_{zz}\}$. The problem is similar if higher order kernels are also included to describe the mesh motion. Such a problem can be solved in the pre-processing stage by assembling the following operator: $[\,\mathbf{WLS}\,] = ([\,\mathbf{A}\,]^{\mathsf{T}}[\,\mathbf{A}\,])^{-1}[\,\mathbf{A}\,]^{\mathsf{T}} \in \mathbb{R}^{N_w \times N_{a,\,b}}$ so that: $\{\mathbf{w}\} = [\,\mathbf{WLS}\,]\{\Delta\boldsymbol{x}\}$. Therefore at each time instant the identification procedure has a small serial requirements in terms of memory occupation and computational cost of order $\mathcal{O}(N_w\, N_{a,\,b})$. Within the framework of a hypercube network topology the parallel communication time can be evaluated to be of order $\mathcal{O}(N_w\, \log_2 p)$, since it is necessary to sum by means of a collective "reduce" operation the partial results associated with each of the p processors.

b) A naïve implementation of the Inverse Distance Weighting (IDW) multivariate interpolation strategy is either memory-efficient or time-efficient, depending on whether matrix $\mathbf{IDW}$ is computed only once in the pre-processing stage and then stored with a significant memory overhead. In fact the computational cost and memory requirements can be estimated to be of order $\mathcal{O}(N_{a,\,b}\, N_{a,\,v})$. The proposed modified algorithm called Sparse Inverse Distance Weighting (SIDW) effectively addresses such an issue reducing the computational cost and memory requirements to be of order $\mathcal{O}(N_{a,\,v}\, S_{\mathsf{IDW}})$, where S_{IDW} is the average number of active columns per row, or in other terms the sparsity band of matrix $\mathbf{SIDW}$, which can be tuned by means of the cut-off parameter ξ. Within the framework of a hypercube network topology the parallel communication time can be evaluated to be of order $\mathcal{O}(N_{a,\,b}\, \log_2 p)$, since it is necessary to assembly by means of a collective "gather" operation the partial residuals associated with each of the p processors. Such a task is summarized in Figure 3.4 with reference to a convenient row-wise partitioning of matrix $\mathbf{SIDW}$.

c) As transpiration boundary conditions simply rely on a modification of the boundary conditions on solid walls, there is only a little additional overhead in terms of serial memory requirements and computational cost, precisely of order $\mathcal{O}(N_{a,\,b})$ in order to compute and store the deformed normal unit vectors. Viceversa there is not any parallel communication time overhead as each of the p processors is independent of the others.

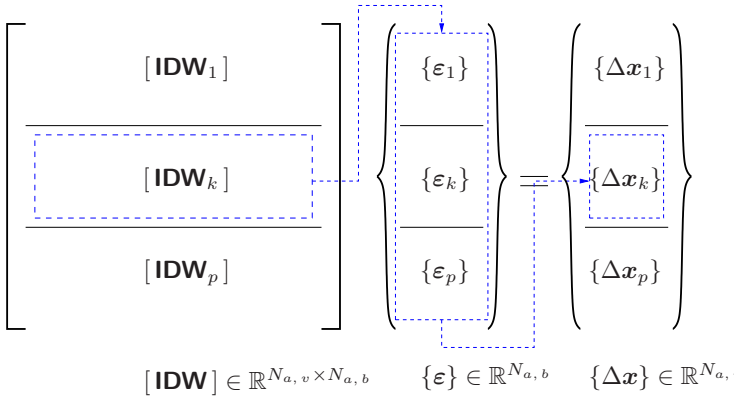

Figure 3.4: Parallel row-wise matrix-array multiplication.

d) Finally the reference algorithm to tackle the mesh deformation problem by means of a Finite Element (FE) discretization has a requirement in terms of memory occupation of order $\mathcal{O}(N_{a,\,v}\,S_{\mathsf{FE}})$ where S_{FE} is the sparsity band of the FE stiffness matrix. The computational cost for solving the resulting linear system by means of a suitable iterative linear solver is of order $\mathcal{O}(M\,N_{a,\,v}\,S_{\mathsf{FE}})$ because for each of the M inner iterations until convergence a sparse matrix-array multiplication is carried out. With a similar argument it is possible to prove that, within the framework of a hypercube network topology, the parallel communication time is of order $\mathcal{O}(M\,N_{a,\,v}\,\log_2 p)$.

If we compare the serial and parallel KPI for each of the steps a), b) and c) we immediately see that the overall requirements in terms of memory occupation, computational cost and communication time are driven by step b). Therefore we choose to focus on a comparison between the performances of the Inverse Distance Weighting (IDW) multivariate interpolation strategy and those of the Finite Element (FE) numerical method based on the elastic analogy. Assuming that the sparsity bands are comparable $S_{\mathsf{IDW}} \simeq S_{\mathsf{FE}}$ (e.g. by tuning the knob ξ) we conclude that the memory requirements are almost identical. However the computational cost of the IDW strategy is M times lower than that of the FE method. In order to fully appreciate the differences in parallel performances of the two options, it is convenient to perform a scalability analysis by evaluating the speedup function $S = T_s/T_p$ and/or the efficiency function $E = S/p$, where T_s and T_p are the computational times required by the serial and parallel algorithms to run on p processors respectively. Of course in the ideal case $S = p$ and $E = 1$ as the communication time overhead is negligible. Viceversa the efficiency functions associated with IDW and FE algorithms are:

$$E_{\mathsf{FE}} = \frac{1}{1 + \tau\, p\, \log_2 p / S_{\mathsf{FE}}} \qquad \text{and} \qquad E_{\mathsf{IDW}} = \frac{1}{1 + \tau\, p\, \log_2 p\, N_{a,\,b}/N_{a,\,v}}, \tag{3.16}$$

where τ is the communication time per unit buffer and depends on the topology and bandwidth of the network. In this analysis the network start-up time τ_0 is neglected.

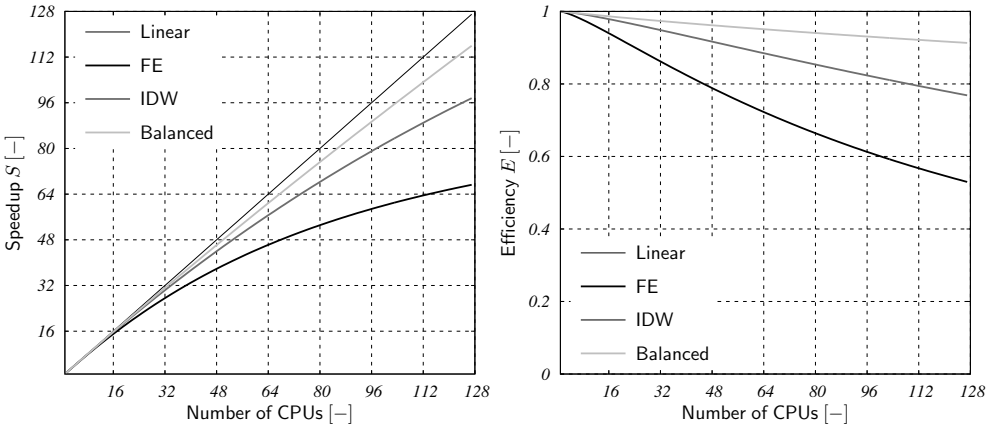

Figure 3.5: Speedup S and efficiency E functions for the IDW and FE algorithms.

Moreover for the IDW algorithm it is interesting to investigate the differences with a so-called balanced scalability analysis by re-evaluating the speedup and efficiency functions with the hypothesis of constant load $L = N_{a,\,v}/p$ (i.e. the size of the problem linearly increases with the overall number of processors p). Assuming conservatively $N_{a,\,b} = N_{a,\,v}^{2/3}$ and carrying out all the computations, it is finally possible to rewrite Eq. (3.16) as follows:

$$\overline{E}_{\mathsf{IDW}} = \frac{1}{1 + \tau\, p^{2/3}\, \log_2 p\, C^{-1/3}}. \tag{3.17}$$

With reference to Figure 3.5 it is possible to appreciate that the IDW strategy yields better parallel performances than the FE method. A non-realistic communication time per unit buffer $\tau = 0.01$ is here used in order to better highlight the differences among the options available.

3.3 Benchmark test problems

In order to assess the credibility in terms of quality and robustness of the proposed mesh deformation strategy it is worthwhile to tackle a series of benchmark test problems of increasing complexity. More in particular we want to stress that the present algorithm is multi-purpose, but particularly suited for aeroservoelastic applications. Therefore we choose realistic benchmark test problems inspired by the aeronautical world, ranging from two-dimensional examples on structured hexahedral anisotropic meshes involving rigid-body motions to three-dimensional examples on unstructured tetrahedral isotropic meshes involving significant levels of deformability. The results are compared with those of the tools built-in within the framework of OpenFOAM software dedicated to dynamic mesh handling, e.g. laplacian smoothing.

The two-dimensional benchmark test problem shown in Figure 3.6-3.7 is concerned with the deformation of a structured hexahedral anisotropic mesh of a multi-element airfoil subject to a rigid rotation of both slat and flap control surfaces up to $\delta \geq 30°$.

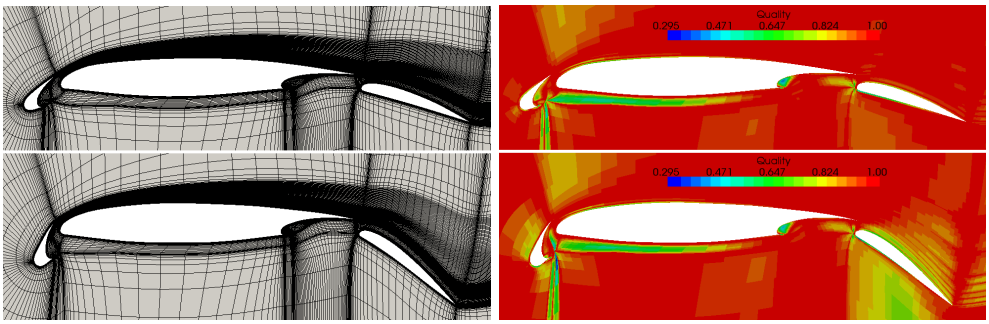

Figure 3.6: Aileron and slat rotation with $\delta = 20°$ applied to the structured hexahedral anisotropic mesh of a multi-element airfoil (left). The cell-wise normalized Jacobian mesh quality measure shows only a moderate deterioration (right).

Such an example is of particular interest because meshes with very high levels of stretching are mandatory within the framework of viscous simulations in order to accurately resolve the laminar and/or turbulent boundary layer close to the body surface. Such a requirement is easily satisfied by using a so-called "C-type" structured mesh generation algorithm. Classical mesh deformation algorithms, e.g. laplacian smoothing, suffer a sudden and significant drop in quality and robustness when the distance between mesh points is decreased below a given tolerance. This drawback is only albeit mitigated by choosing ad hoc diffusivity functions, e.g. quadratic. On the contrary the proposed algorithm is not affected by such issues. With reference to Figure 3.6 it is possible to appreciate the density of mesh points within the boundary layer region in both the reference and target configurations and the small changes in the contours of the cell-wise normalized Jacobian mesh quality measure, especially near-by the slat and flap control surfaces and with peak value at the slat leading edge.

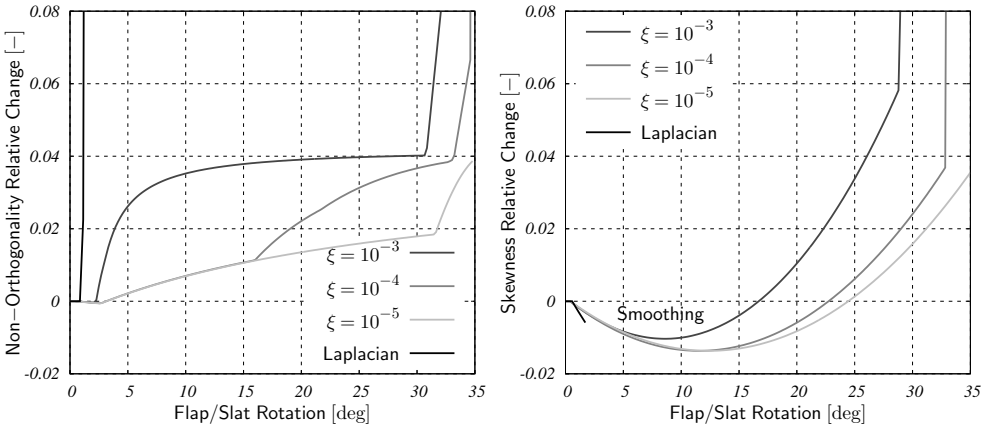

Figure 3.7: Relative changes in cell-wise non-orthogonality (left) and skewness (right) mesh quality measures as a function of slat/flap rotation angle with $p = 2$ and tuning knob ξ.

Moreover we investigate the behaviour of the proposed algorithm (in terms of relative changes with respect to the reference configuration of cell-wise non-orthogonality and skewness mesh quality measures) by choosing a kernel order $p = 2$ and suitably tuning the sparsity band cut-off parameter ξ of the Inverse Distance Weighting (IDW) multivariate interpolation operator. With reference to Figure 3.7 it is very important to remark that the laplacian smoothing algorithm fails even for small slat and flap rotation angles, while the proposed IDW-based strategy preserves the mesh quality with positive relative changes never exceeding 5% up to $\delta \geq 30°$. More in particular we also observe that smaller values of the cut-off parameter ξ correspond to smaller positive relative changes of non-orthogonality and skewness mesh quality measures. In other terms the mesh quality associated with the target configuration is closer to the mesh quality associated with the reference configuration. This is due to the fact that as ξ approaches zero the sparse matrix **SIDW** converges to the full matrix **IDW**. Finally it is interesting to remark that for relatively small slat and flap rotation angles the skewness mesh quality measure shows negative relative changes, i.e. the proposed mesh deformation algorithm improves the mesh quality.

The three-dimensional benchmark test problem shown in Figure 3.8 is concerned with the deformation of an unstructured tetrahedral isotropic mesh of a complete aircraft subject to a first elastic modal shape amplitude $q_7 = 100$ (wing bending) with a maximum vertical displacement at wing tip $\max(\{\boldsymbol{u}_s\}) = \max([\boldsymbol{U}|_7])\, q_7 \simeq 5$ m, quite significant and challenging with a wing span $b = 18.72$ m. Such an example is of particular interest because meshes with high levels of isotropy are recommended within the framework of non-viscous simulations in order to limit the number of cells and therefore the computational cost without jeopardizing the mesh quality. Such a requirement is easily satisfied by using a Delaunay unstructured mesh generation algorithm with each cell very close to the optimal simplex. Classical mesh deformation algorithms, e.g. laplacian smoothing, suffer a so-called "packing" of the mesh points in the vicinity of the boundaries with maximum displacements, e.g. at the wing tip.

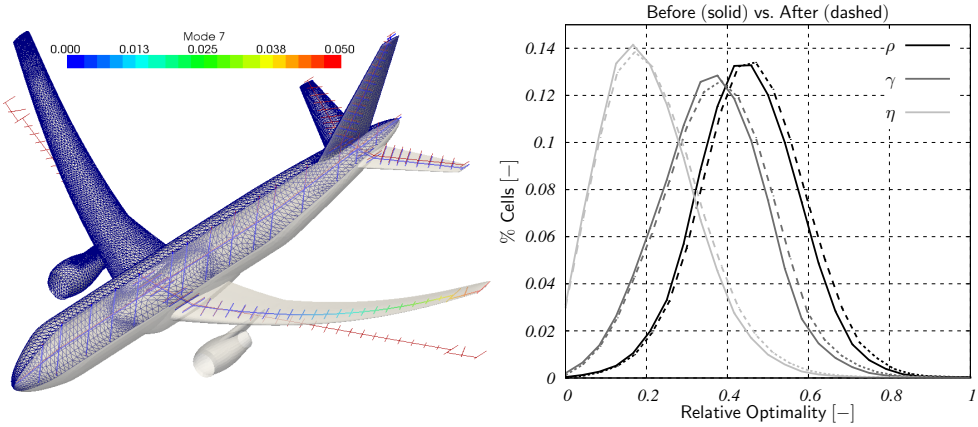

Figure 3.8: A320 aircraft with a first elastic modal shape amplitude $q_7 = 100$ (left) and histograms of cell-wise relative optimality measures ρ, γ and η before and after mesh motion.

Eventually this may lead to non-acceptable non-orthogonality and skewness mesh quality measures and/or negative cell volumes. This drawback is only albeit mitigated by choosing ad hoc diffusivity functions, e.g. quadratic. Such a sudden and significant drop in quality and robustness is related to the fact that the algorithms tackling the mesh deformation problem by means of Finite Element (FE) discretization operators are based on local shape functions. On the contrary the proposed algorithm is not affected by such issues. In fact the Inverse Distance Weighting (IDW) multivariate interpolation strategy relies on global shape functions cut-off by means of the knob ξ.

With reference to Figure 3.8 we now investigate the behaviour of the proposed algorithm (with a comparison of conventional cell-wise relative optimality indicators before and after mesh motion) by choosing a kernel order $p = 3$ and a sparsity band cut-off parameter $\xi = 10^{-4}$ of the Inverse Distance Weighting (IDW) multivariate interpolation operator. More in particular we use the following mesh quality measures, particularly suited for tetrahedral meshes:

$$\rho = \frac{\min(\{L\})}{\max(\{L\})} \qquad \gamma = \frac{V}{\|\{S\}\|_1 \max(\{L\})} \qquad \eta = \frac{V^{2/3}}{\|\{L\}\|_2^2} \tag{3.18}$$

where V is the cell volume while $\{S\}$ and $\{L\}$ are the arrays of the areas and lengths respectively of the faces and edges belonging to the cell. For an equilateral tetrahedron it is worthwhile to remark that the adimensional mesh quality measures above are: $\overline{\rho} = 1$, $\overline{\gamma} = 0.068041$ and $\overline{\eta} = 0.040062$. The histograms shown in Figure 3.8 are built by evaluating the relative distance with respect to such reference values. We do not show the results of the laplacian smoothing algorithm because it fails even for small maximum vertical displacements, while the proposed IDW-based strategy preserves the mesh quality. More in particular we observe that the histograms of cell-wise relative optimality measures ρ, γ and η are slightly shifted towards bigger relative optimality values after the mesh motion. This means that the mesh quality is decreasing but very slowly, without jeopardizing the accuracy of the aeroservoelastic simulation.

4

Static aeroservoelasticity

This Chapter is aimed at assessing the credibility of the proposed aeroservoelastic analysis toolbox by tackling a set of static aeroservoelastic problems and comparing the results with reference experimental and numerical data available in literature. The availability of such an integrated environment is almost mandatory from the very beginning of the design process. More in particular we investigate the sensitivity to different modelling options for representing the aerodynamic sub-system. In such a way it is easier to strike the best balance between accuracy of the results and computational efficiency, choosing within the hierarchy of tools available the lowest-fidelity Doublet Lattice Method (DLM) or the Non-Linear Full Potential (NLFP) equations or the Euler equations or the highest-fidelity Reynolds Averaged Navier-Stokes (RANS) equations.

In §4.1 the static aeroelastic benchmark test problem of computing the reference equilibrium or "trim" configuration of the HiReNASD wing is presented. Such an example is of particular interest because it was selected as a benchmark test problem for the AIAA Aeroelastic Prediction Workshop series with the objective of providing an impartial forum for assessing state-of-the-art CA methods as practical tools for the prediction of static and dynamic aeroservoelastic phenomena within the transonic regime. More precisely, after providing an overview of the structural and aerodynamic models, we compute the static aeroelastic response of the wing in attached axes by means of the iterative method and compare the results with reference experimental data. Such a procedure is repeated for different angles of attack $\alpha \in (-1.5°, 4.5°)$ in order to highlight the non-linear phenomena associated with the transonic regime. In §4.2 we present the numerical results for the non-linear aeroservoelastic trim of a free-flying A320 aircraft equipped with innovative passive aeroelastic wing tip devices. More precisely, after providing an overview of the structural and aerodynamic models, we compute the trim parameters and the static aeroelastic response of the aircraft for different configurations and maneuvers and compare the results with those of Nastran, a "de-facto" standard tool within the aeronautical industry, in order to highlight the differences between lower and higher fidelity tools in the transonic regime.

4.1 HiReNASD wing

Currently, a benchmarking standard for use in validating the accuracy of CA codes does not exist. Many aeroelastic data sets have been obtained in wind-tunnel and flight testing. However none have been globally recognized as an ideal data set. There are numerous reasons for this. One is that often such aeroelastic data sets focus on the aeroelastic phenomena alone (flutter, for example) and do not contain associated information, such as unsteady pressures or structural deflections. Other available data sets focus solely on the unsteady pressures. Other deficiencies include omission of relevant data, such as flutter frequency or the acquisition of qualitative deflection data. In addition to these content deficiencies, all of the available data sets present both experimental and computational technical challenges. Experimental issues include facility influences, non-linearities beyond those being modelled, and data post-processing. From a computational perspective, technical challenges include modelling geometric complexities, coupling between the flow and the structure, turbulence modelling, grid issues, and boundary conditions. Moreover the availability of suitable computational resources in order to yield feasible turn-around times for CA simulations should also be considered as a potential bottleneck. An Aeroelasticity Benchmark Assessment task was initiated at NASA in 2009 with the objectives of a) examining the existing potential experimental data sets and selecting the one(s) viewed as the most suitable for computational benchmarking and b) performing an initial computational evaluation of these configurations using the NASA in-house computational aeroelastic software as part of the code validation process.

A successful effort results in the identification of a focus problem for government, industry, and academia to use in demonstrating and comparing codes, methodologies, and experimental data to advance the state-of-the-art. Ideally such a focus problem would be the first of many put forth for this purpose, with a future goal being the design, fabrication, and testing of an aeroelastic model recognized by the community as a benchmark test case. Excellent examples of such a progression and escalation of code validation in the international community are the series of AIAA Drag Prediction and High Lift Prediction workshops. These workshops have three main objectives: a) to assess the ease and practicality of using state-of-the-art computational methods for aerodynamic load prediction, b) to impartially evaluate the effectiveness of the high-fidelity solvers and c) to identify areas for improvement. The structure of such initiatives provides a template for other computational communities seeking similar improvements in accuracy within their own fields. The examination and selection of aeroelastic data sets within the Aeroelasticity Benchmark Assessment task together with the computational evaluation of these configurations led to initiation of an AIAA Aeroelastic Prediction Workshop series.

The High Reynolds Number Aero-Structural Dynamics (HiReNASD) project was led by Aachen University with funding from the German Research Foundation (DFG). It was initiated in 2004 to produce a high-quality transonic aeroelastic data set at realistic flight Reynolds numbers for a large transport-type wing/body configuration and tested in the European Transonic Windtunnel (ETW) in 2006. This experiment was selected among the benchmark test problems for the AIAA Aeroelastic Prediction Workshop series kick-off. [20]

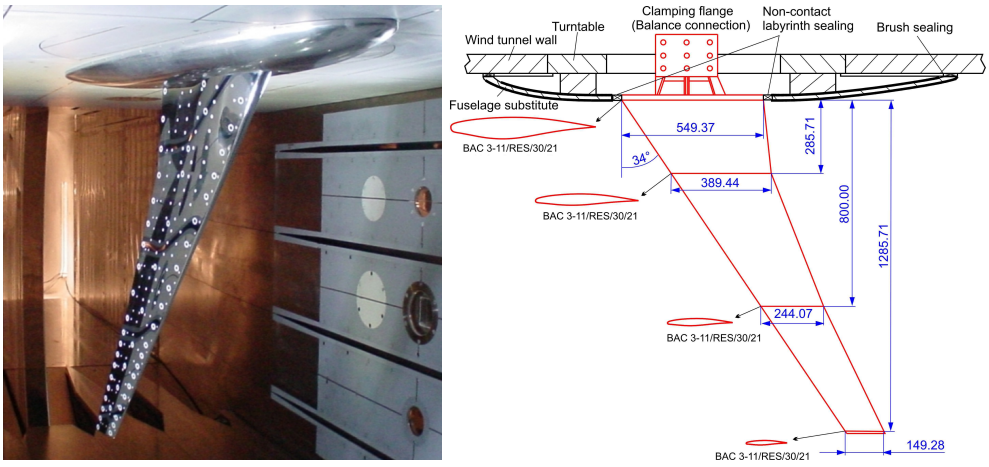

Figure 4.1: Experimental set-up for the HiReNASD wing.

The HiReNASD experimental set-up shown in Figure 4.1 is a ceiling-mounted, semi-span, clean-wing configuration with a leading-edge sweep angle $\Lambda_{LE} = 34°$, a span $b = 1.2857$ m and a mean aerodynamic chord $\bar{c} = 0.3445$ m. It consists of three sections. The two outboard sections use an 11-percent thick BAC3-11/RES/30/21 supercritical airfoil. The inboard section uses the same airfoil thickened linearly from 11-percent at its outer edge to 15-percent at the root. To minimize boundary layer interference during testing, a generic fuselage was included, mechanically isolated from the wing by a labyrinth seal. Extensive measurements were acquired during testing of the HiReNASD model. Instrumentation included a six-component balance, Surface Pattern Tracking (SPT) optical markers for surface deformation measurements on the pressure side of the wing, 11 accelerometers, 28 strain-gages, and 259 unsteady pressure transducers. The pressure transducers were distributed along the upper and lower surfaces at 7 span sections.

The HiReNASD test matrix consisted of both static and dynamic measurements at different flow conditions, with Reynolds number Re varying from $7 \cdot 10^6$ up to $73 \cdot 10^6$ and dynamic pressures up to $q_\infty = 130 \cdot 10^3$ Pa at the following transonic Mach numbers $M_\infty \in (0.70, 0.75, 0.80, 0.83, 0.85, 0.88)$. The test medium was nitrogen. For static testing, pressure distribution and lift and drag coefficients were acquired at different angles of attack. Dynamic testing involved forced vibrations of the wing at the natural frequencies of the first bending, second bending, and first torsion modes and was performed over the range of Reynolds numbers at different angles of attack.

The objective of the present work is that of comparing (in terms of aerodynamic loads and structural displacements) the numerical results of the multi-fidelity toolbox for aeroservoelastic analysis AeroFoam with the experimental data of run No. 132 of the HiReNASD project, corresponding to the static aeroelastic response of the wing/body at Reynolds number $Re = 7 \cdot 10^6$, Mach number $M_\infty = 0.8$ and dynamic pressure $q_\infty = 40055$ Pa and choosing the following angles of attack $\alpha \in (-1.5°, 0.0°, 1.5°, 3.0°, 4.5°)$.

4.1.1 Structural model

In literature the choice of the appropriate structural model is quite controversial. In fact two different Finite Element (FE) are available from the HiReNASD project website. Both are based on a very detailed discretization of the wing/body structure in uniform solid elements, tetrahedral or hexahedral respectively, for more than 200000 grid points. The two models yield slightly different modal frequencies with differences below 5% and the first 8 dynamically relevant modal shapes are almost identical.

However the current trend within the framework of AIAA Aeroelastic Prediction Workshop series is that of choosing a Finite Element (FE) stick beam structural model with limited d.o.f. and successively tuning e.g. the material properties in order to match as closely as possible the natural frequencies and modal shapes measured experimentally by means of Ground Vibration Test (GVT). With reference to Table 4.1 and Figure 4.1 we choose a FE stick beam structural model with only 62 nodes, each connected with 4 additional nodes (at leading edge, trailing edge, maximum and minimum thickness locations within each $x - z$ section of the wing/body) by means of rigid elements for a total of $N_s = 310$ grid points. The addition of such extra nodes is beneficial for assembling the aeroelastic interface operator as it makes possible to use only translation d.o.f. but at the same time accurately reconstruct rotations. It is worthwhile to remark that both the wing and the fuselage are modelled as deformable structures: such a choice is beneficial in terms of robustness of the mesh deformation algorithm. [20]

Mode	$\boldsymbol{f}$ [Hz]	**Description**	**Mode**	$\boldsymbol{f}$ [Hz]	**Description**
1	25.95	1^{st} bending	5	258.38	3^{rd} bending
2	82.42	2^{nd} bending	6	273.20	4^{h} bending
3	117.58	1^{st} in-plane bending	7	275.29	2^{nd} in-plane bending
4	168.42	1^{st} bending-torsion	8	275.29	2^{nd} bending-torsion

Table 4.1: Modal bases used for the non-linear aeroelastic trim analysis of HiReNASD wing. The modal shapes are organized in lower-frequency (left) and higher-frequency (right).

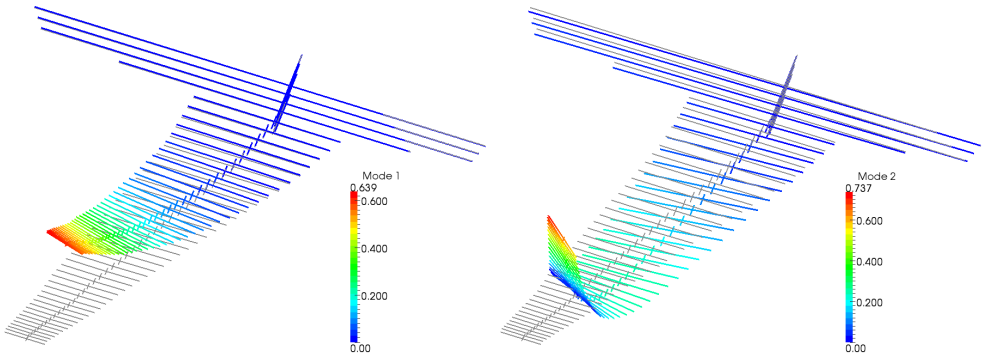

Figure 4.2: Stick beam FE structural model of the HiReNASD wing deformed accordingly to first ($q_1 = 1$, $f_1 = 25.95$ Hz) and second ($q_2 = 1$, $f_7 = 82.42$ Hz) attached modal shapes.

4.1.2 Aerodynamic model

Concerning the aerodynamic model the objective is that of performing a comparison between the numerical results of Euler and RANS simulations. More in particular we choose the Spalart-Allmaras turbulence model popular within the aeronautical industry. In order to speed-up the convergence to the steady-state within each outer iteration of the non-linear aeroelastic trim procedure a 2 levels Multi-Grid (MG) acceleration driver is used in combination with a 5 steps Explicit Runge-Kutta (ERK) time-stepping scheme and Implicit Residual Smoothing (IRS). The inner iteration limit is set to $I = 100$.

To quantify the computational effort, for the Euler runs we use an aerodynamic mesh with $N_{a,\,b} = 136130$ boundary faces and $N_{a,\,v} = 963719$ tetrahedral cells while for the RANS runs we use an aerodynamic mesh with $N_{a,\,b} = 176474$ boundary faces and $N_{a,\,v} = 1909304$ hybrid tetrahedral and hexahedral (within the boundary layer and wake regions) cells as shown in Figure 4.3. Nevertheless, decomposing the problem on 16 Intel Xeon X5650 processors, a non-linear aeroelastic trim simulation converges with residuals below $\epsilon \leq 10^{-3}$ in 2 and 8 hours for Euler and RANS simulations respectively.

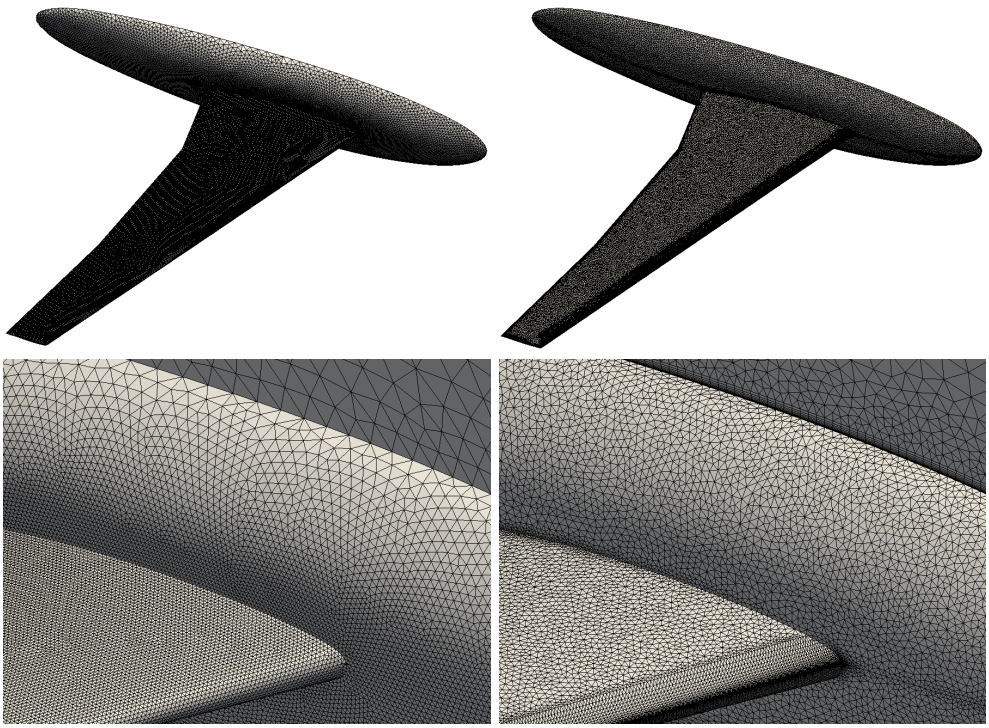

Figure 4.3: Surface aerodynamic meshes (with detailed view at wing-fuselage connection) for the HiReNASD wing for Euler (left) and RANS (right) simulations. In this latter case it is possible to appreciate the higher resolution and the primsatic boundary layer.

4.1.3 Trim analysis

In Figure 4.4 the convergence history of the elastic d.o.f. and of the generalized aerodynamic forces is shown for Euler and RANS simulations for $\alpha = 1.5°$. After a first block of 200 inner iterations to start-up the non-linear aeroelastic trim procedure the elastic d.o.f are updated with a relaxation factor $\omega = 0.5$ until convergence within a suitable tolerance $\epsilon = 10^{-4}$ in less than 3000 inner iterations. It is interesting to remark that the Euler simulation converges monotonically to larger generalized displacements than the RANS simulation. In this latter case it is also necessary to increase the number of inner iterations to drive the residuals below the same threshold.

In Figures 4.5-4.6 the contours of the pressure coefficient C_p and the structural displacements $|\boldsymbol{s}|$ are shown onto the final configuration of the wing/body with elastic deformations suitably magnified for $\alpha = 1.5°$. It is possible to qualitatively appreciate the stronger expansion of the flow on the upper surface of the wing for the Euler simulation with respect to RANS, e.g. because of the absence of diffusive phenomena.

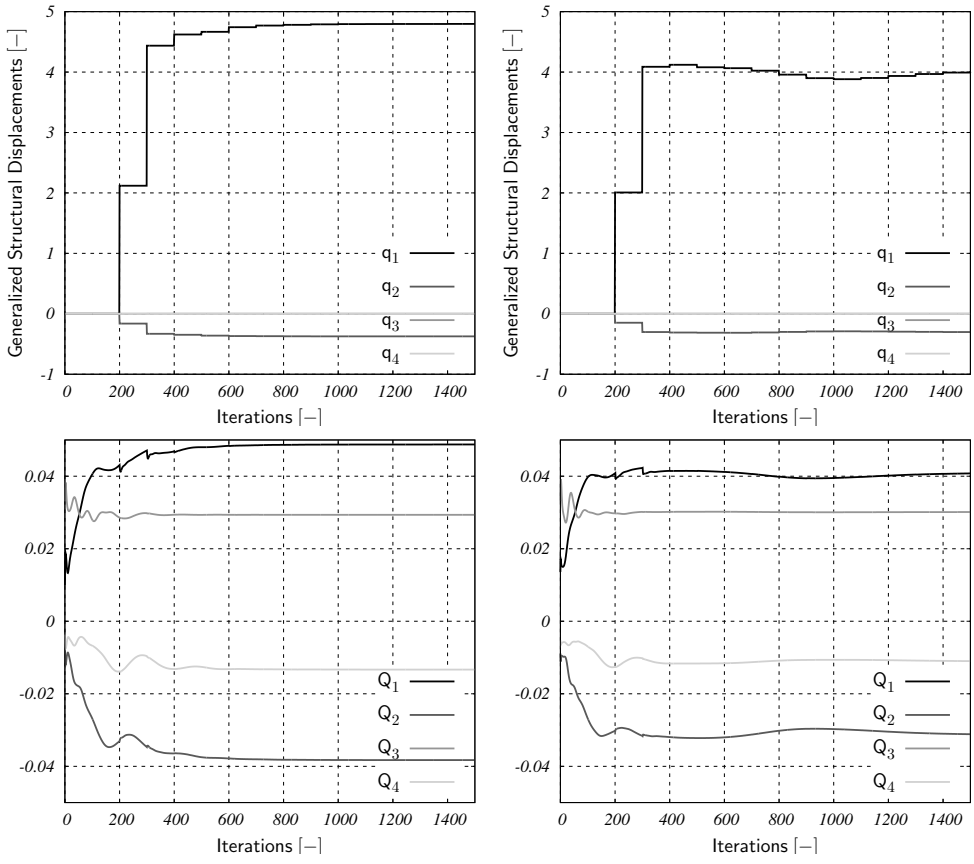

Figure 4.4: Convergence history of the generalized displacements (top) and the generalized aerodynamic forces (bottom) for Euler (left) and RANS (right) simulations for $\alpha = 1.5°$.

As a result the aerodynamic loads and therefore the structural displacements are larger for the Euler simulation with respect to RANS. More quantitative results can be found in Figure 4.7 with a comparison of the distribution of the pressure coefficient C_p along reference wing sections between NLFP, Euler and RANS simulations and experimental data for $\alpha = 1.5°$. It is interesting to remark that the numerical results of RANS simulation fairly agree with the reference experimental and numerical data. Viceversa the numerical results of Euler simulation show a 5% shift downstream of the shock wave position and therefore a significant increment of the aerodynamic loads. The numerical results of NLFP should converge to those of Euler simulation. However they fall quite close to the experimental data because of the numerical dissipation of the NLFP solver here selected. [60] Finally in Figure 4.8 the maximum wing tip displacements are plotted as a function of the angle of attack α together with the relative errors with respect to the experimental data. It is worthwhile to remark that the relative errors associated with RANS is significantly lower than those associated with NLFP or Euler for $\alpha \leq 3.0°$. Viceversa for $\alpha = 4.5°$ the accuracy of NLFP, Euler and RANS predictions are comparable.

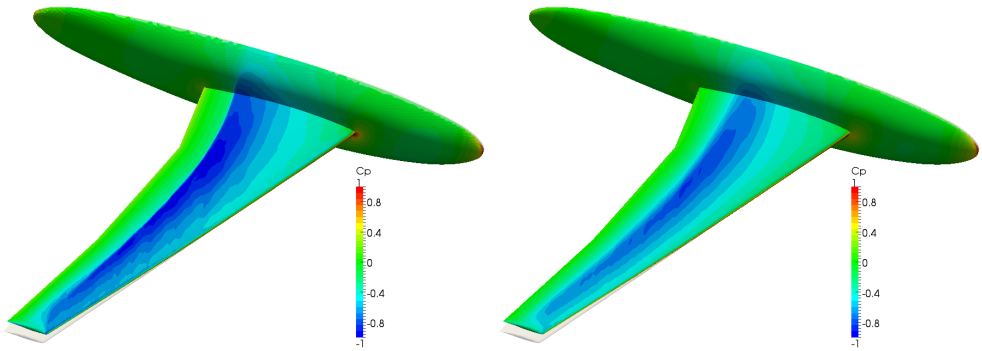

Figure 4.5: Comparison of the pressure coefficient C_p contours between Euler (left) and RANS (right) numerical results for $\alpha = 1.5°$ on the deformed configuration (5× magnified).

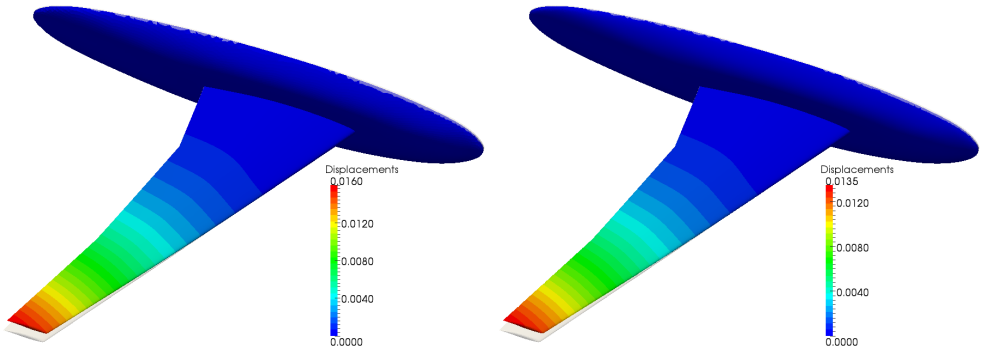

Figure 4.6: Comparison of the structural displacements $|\boldsymbol{s}|$ contours between Euler (left) and RANS (right) numerical results for $\alpha = 1.5°$ on the deformed configuration (5× magnified).

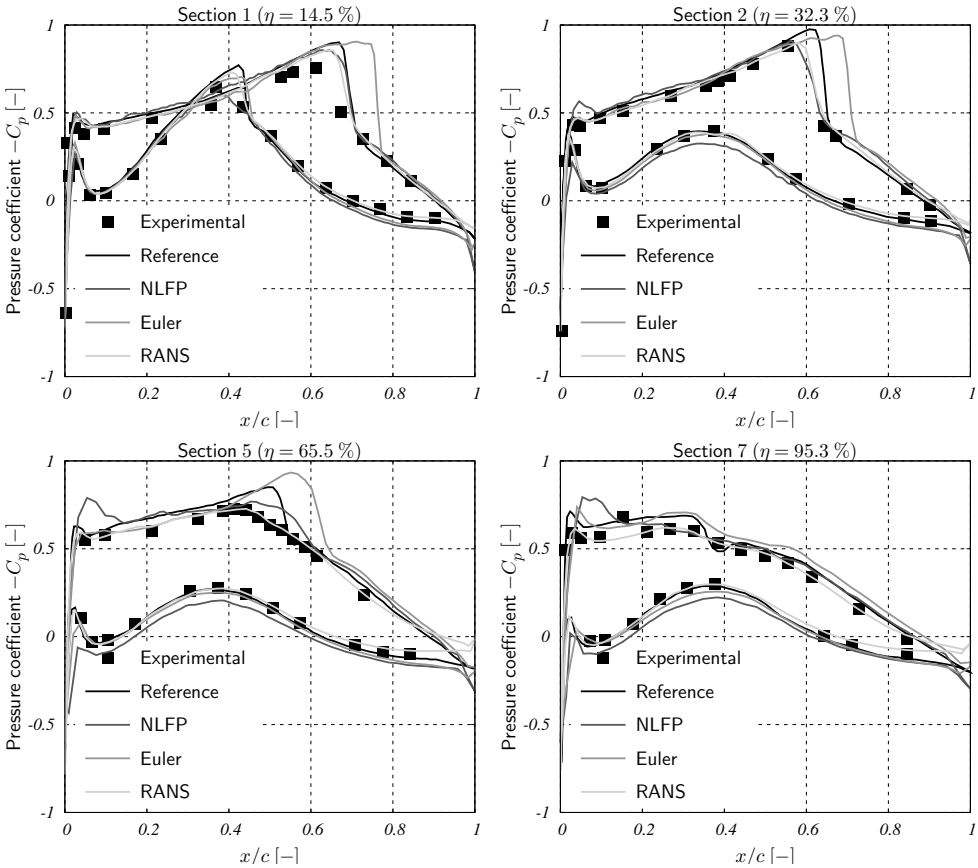

Figure 4.7: Comparison of the distribution of the pressure coefficient C_p along reference wing sections between experimental data and NLFP, Euler and RANS simulations.

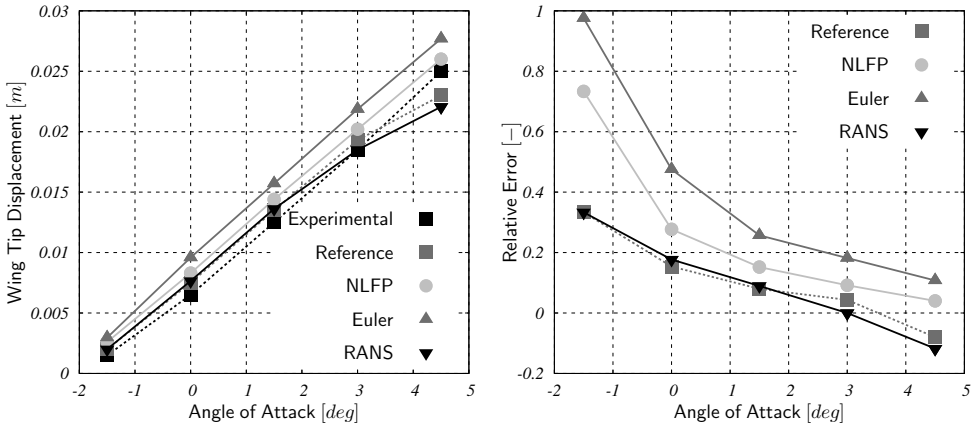

Figure 4.8: Maximum wing tip displacement as a function of angle of attack α (left) and relative error with respect to experiments (right) for NLFP, Euler and RANS simulations.

4.2 A320 aircraft

After tackling the non-linear aeroelastic trim problem of a restrained wing, we now focus on the more challenging problem of the non-linear aeroservoelastic trim of a free-flying aircraft. We include the tag "servo" because it is necessary to solve also for the unknown rigid d.o.f. associated with control surfaces in order to satisfy both the rigid and elastic trim conditions. More in particular the objective of the present work is that of carrying out a comparison between the results of DLM and CFD tools, thus understanding the limits of computationally efficient linearized numerical methods in the transonic regime. We select the Airbus A320 shown in Figure 4.9 (the undisputed best-selling aircraft product line of all time) as reference aircraft and we use the higher-fidelity model to verify the overall performances of innovative passive aeroelastic wing tip devices designed with lower-fidelity models embedded into a multi-disciplinary optimization tool. Such a multi-fidelity approach closely matches today's design best practices within the aerospace industry: together with the availability of more powerful and less expensive computing resources the present trend, even in preliminary design, is that of replacing or better placing side by side classical linear(ized) efficient low-fidelity methods with more sophisticated and expensive high-fidelity ones.

More in particular we consider two different design concepts: a "discrete" option which consists of an additional wing tip surface attached to the wing by means of a suitably tuned flexible element and a "raked" option which is a horizontal wing span extension designed in composite materials in order to achieve a load alleviation aeroelastic tailoring effect. The matrix of test cases under consideration for the CFD verification of DLM data can be summarized as follows:

a) discrete wing tip option, transonic cruise at $M_\infty = 0.78$ and $n = 1$,

b) discrete wing tip option, symmetric pull maneuver at $M_\infty = 0.4$ and $n = 1.5$,

c) raked wing tip option, transonic cruise at $M_\infty = 0.78$ and $n = 1$.

Such an application is quite a relevant topic within the aeronautical industry today. In fact the soaring fuel price and the environmental concerns have triggered intensified efforts to further improve the efficiency of air transportation. A strategy that has been widely deemed successful is the reduction of induced drag, which during cruise conditions constitutes approximately 40% of the total drag, by means of wing tip devices. This concept delivers benefits such as reduction in emissions and fuel consumption, directly translating into money savings for airlines, improvement of take-off and landing performances, with reduced community noise and payload or range increase. An important advantage of this technology is that it can be retrofitted onto existing aircrafts. This is for instance the present trend within the Airbus A320 aircraft product line with the so-called "sharklets" wing tip devices going towards in-flight testing in 2012 in order to validate the expected multiple advantages for operators including more than 3.5% savings in overall fuel consumption on long route sectors, increased range and payload, better takeoff performances and rate-of-climb, reduced engine maintenance costs and higher residual value of the aircraft.

Figure 4.9: Cutaway illustration of the A320 reference aircraft (left) together with a picture of the upgraded A320 aircraft equipped with winglets (right).

Historically the most successful solution are undoubtedly winglets, first introduced by Whitcomb in the 1970's [90]. These devices have however a significant structural impact since they increase the structural loads acting on the wing, leading to the need of reinforcements with therefore weight penalties. Another drawback is the loss of sufficient flutter stability, often solved by mass balancing. Hence a passive aeroelastic load alleviation function would be attractive. This is achieved taking advantage of the unavoidable aeroelastic effects in a beneficial manner: the structure of the device is tailored and made sufficiently flexible to generate a favourable lift distribution for reduced structural loads. This may lead to a reduction of the required wing-box reinforcements and to a net performance gain superior to the traditional devices. Moreover, a totally passive system is favourable because actuators and sensors, with the necessary level of redundancy in case of failure, are not required, thus such a solution turns out to be lighter, simpler and less expensive. [14]

4.2.1 Structural model

For an aircraft with a relatively standard configuration it is appropriate to choose a Finite Element (FE) stick beam structural model with lumped masses. This kind of structural model, highly popular within the aeronautical industry especially in the conceptual design phase, is computationally efficient, easy to create and/or handle and requires a minimal amount of information and yet it is capable of modelling the global inertial and stiffness characteristics of the aircraft structure. To build the FE stick beam structural model the software NeoCASS (Next generation Conceptual Aero-Structural Sizing) is adopted. NeoCASS is a suite of modules that combines state of the art computational, analytical and semi-empirical methods to tackle all the aspects of the aero-structural analysis of a design layout at a conceptual design stage. [19, 18] In particular it includes a module, called GUESS (Generic Unknowns Estimator in Structural Sizing), which produces a first-try mass and stiffness distribution. The only information required is the geometric description of the aircraft and the masses of fuel and payload. The estimation of the non-structural mass distribution is based on handbook methods while the stiffness and structural mass distributions are predicted by an analytical sizing of the airframe based on ultimate loads formulas.

Mode	$\boldsymbol{f}$ [Hz]	**Description**	**Mode**	$\boldsymbol{f}$ [Hz]	**Description**
α	0.0	rigid pitch	α	0.0	rigid pitch
δ	0.0	rigid elevator	δ	0.0	rigid elevator
7	2.34	1^{st} bending	7	2.35	1^{st} bending
10	5.31	2^{nd} bending	10	5.32	2^{nd} bending
11	5.57	in-plane bending	11	5.61	in-plane bending
13	6.62	1^{st} torsion	13	6.61	1^{st} torsion
15	8.33	1^{st} bending-torsion	16	8.05	1^{st} large tip bending
17	8.74	2^{nd} bending-torsion	17	8.65	2^{nd} large tip bending

Table 4.2: Modal bases used for the non-linear aeroelastic trim analysis of discrete (left) and raked (right) wing tip models. Only the symmetric modal shapes are included.

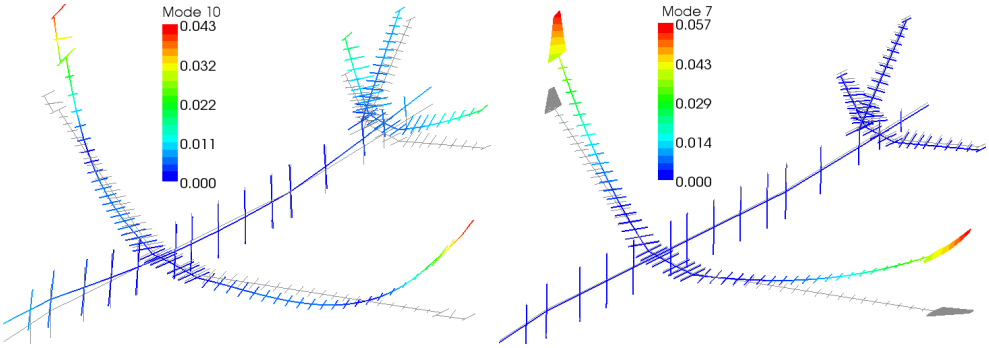

Figure 4.10: FE structural models of A320 aircraft: simple stick beam model (left) and hybrid beam-shell model (right) deformed accordingly to second ($q_{10} = 150$, $f_{10} = 5.31$ Hz) and first ($q_7 = -100$, $f_7 = 2.35$ Hz) symmetric free-free modal shapes.

With reference to Figure 4.10 for the discrete wing tip configuration we choose a FE stick beam structural model with $N_s = 566$ d.o.f. while for the raked wing tip configuration a FE hybrid shell-beam structural model with $N_s = 2576$ d.o.f. is used. Each node associated with a beam element is connected with 4 additional nodes (at leading edge, trailing edge, maximum and minimum thickness locations of the wing sections of the lifting surfaces and at each cross-section of the fuselage) by means of rigid elements. The addition of such extra nodes is beneficial for assembling the aeroelastic interface operator as it makes possible to use only translation d.o.f. but at the same time accurately reconstruct rotations. It is worthwhile to remark that only the flexibility of the engine nacelles is not taken into account, whereas the lifting surfaces and the fuselage are modelled as deformable structures: such a choice is beneficial in terms of robustness of the procedure and quality of the results.

Finally the free-free modal bases shown in Table 4.2 are used to approximate the structural displacements of the A320 aircraft. More in particular we take into account as dynamically relevant the first 8 rigid and deformable symmetric modal shapes. There are significant differences among the structural models associated with the discrete and raked options, especially for the higher frequency modes.

4.2.2 Aerodynamic model

Concerning the aerodynamic model the objective is that of performing a comparison between the numerical results of DLM and CFD simulations. Moreover we investigate the impact of different strategies for dynamic mesh handling, such as DGCL-compliant mesh deformation versus transpiration boundary conditions.

On the one hand the lower-fidelity aerodynamic model is created with NeoCASS. The computational mesh comprises only the wing and the the tailplanes modelled as flat lifting surfaces without twist nor camber, and it is suitable for classical linear(ized) methods based on the small disturbances theory. The wing-body interference of the fuselage is not modelled. With 748 panels on the wing, 254 and 90 panels on the horizontal and vertical tail surfaces respectively, a total of 1092 aerodynamic d.o.f. is used. Both for steady and unsteady cases, the subsonic DLM solver included within the software Nastran is used.

On the other hand the higher-fidelity aerodynamic model is based on AeroFoam toolbox for solving the Euler equations as the best compromise option among the higher-fidelity choices between computational efficiency and accuracy of the results. In order to speed-up the convergence to the steady-state within each outer iteration of the non-linear aeroservoelastic trim procedure a 2 levels Multi-Grid (MG) acceleration driver is used in combination with a 5 steps Explicit Runge-Kutta (ERK) time-stepping scheme and Implicit Residual Smoothing (IRS). The inner iteration limit is set to $I = 100$. To quantify the computational effort, for the discrete wing tip configuration cases we use an aerodynamic mesh with $N_{a,b} = 87684$ boundary faces and $N_{a,v} = 635700$ tetrahedral cells while for the raked wing tip configuration cases we use an aerodynamic mesh with $N_{a,b} = 90838$ boundary faces and $N_{a,v} = 690957$ tetrahedral cells as shown in Figure 4.11. Nevertheless, decomposing the problem on 16 Intel Xeon X5650 processors, a non-linear aeroservoelastic trim simulation converges with residuals below $\epsilon \leq 10^{-3}$ in less than 2 hours.

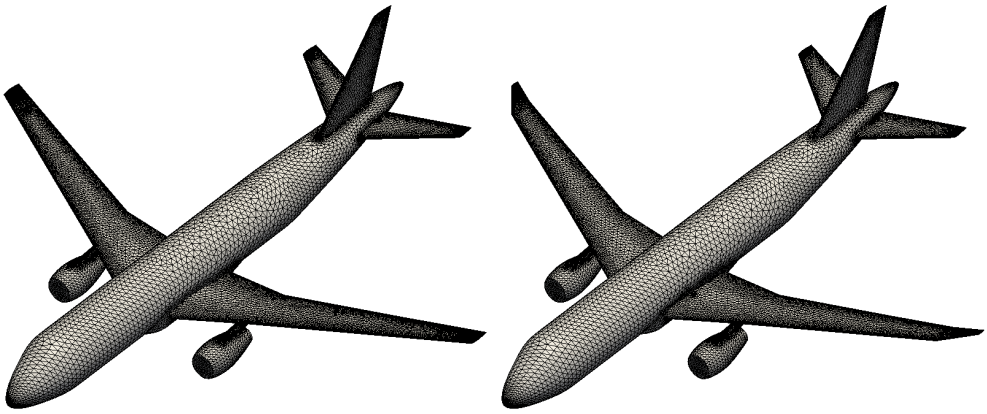

Figure 4.11: Surface aerodynamic meshes of the A320 aircraft for the discrete wing tip design concept (left) and the raked wing tip design concept (right).

4.2.3 Trim analysis

In Figure 4.12 the convergence history of the rigid and elastic d.o.f. and of the rigid-body and generalized aerodynamic forces is shown. It is easy to notice the first block of 200 inner iterations for building a FD approximation of the stability derivatives matrix perturbing α and then δ with $\Delta\alpha = \Delta\delta = 2°$. The following block of 200 inner iterations are used to start-up the non-linear trim of the rigid aircraft updating only α and δ with a relaxation factor $\omega = 0.5$ while constraining the elastic d.o.f. to zero. Finally also the elastic d.o.f are updated until convergence to the non-linear trim of the elastic aircraft within a suitable tolerance $\epsilon = 10^{-4}$ in less than 3000 inner iterations.

In Figures 4.13-4.15 the contours of the pressure coefficient C_p are shown onto the final configuration of the aircraft with rigid-body motions and elastic deformations. For instance it is possible to qualitatively appreciate the different pitch attitudes of the aircraft in cruise and during a symmetric pull maneuver or also the significantly different torsion deformation of the wing tip devices between the discrete and raked design concepts. More quantitative results can be found in Table 4.3 with a comparison between the converged values of the rigid d.o.f. α and δ computed with AeroFoam (CFD) and Nastran (DLM). It is remarkable that the values predicted by low-fidelity models are always larger in absolute value than those predicted by high-fidelity ones. A similar argument is valid if we examine the results of test case a*) corresponding to a lower-fidelity simulation of problem a) by choosing transpiration boundary conditions in order to simulate the geometric effects of the boundary motion without actually deforming the computational grid. In Figure 4.16 a quantitative comparison between AeroFoam and Nastran is presented for the bending and torsion deformation of the wing. It is interesting to observe that for all the test cases the results are fairly comparable for the vertical displacements with a maximum relative error at wing tip ranging from $\|e_{a)}\| \simeq \|e_{c)}\| \simeq 8\%$ to $\|e_{b)}\| \simeq 16\%$. On the contrary the results are significantly biased for the torsion rotations with a maximum relative error at wing tip ranging from $\|e_{c)}\| \simeq 47\%$ to $\|e_{a)}\| \simeq \|e_{b)}\| \simeq 52\%$.

Concerning the higher relative errors in twist, the discrepancy may be attributed to the significantly different local aerodynamic loads distribution predicted by the linear numerical methods (DLM) rather than by the more sophisticated tools (CFD). In Figure 4.17 the results of a grid convergence study (with a coarser and finer mesh in addition to the baseline one) on test case a) are presented. The distribution of the pressure coefficient C_p predicted by AeroFoam shows that the shock wave at about 55% of the local chord on the upper surface is captured more sharply as the grid is refined. However also with the coarser mesh it is possible to obtain a reliable prediction of the resultant aerodynamic force and torque. On the contrary the distribution of the pressure coefficient C_p predicted by Nastran shows a suction peak at the leading edge, a feature typical of subsonic flows. Although the resultant aerodynamic force is, in both cases, of similar magnitude, the supersonic region and the shock wave generate relatively strong rear loading with a consequent big change in the torque acting on the wing section with respect to the linear solution. This effect is important since it modifies the aeroelastic deformation of the wing and it has an impact on the sizing of the structure. [66]

a) Discrete wing tip: cruise at $M_\infty = 0.78$ and $n = 1$

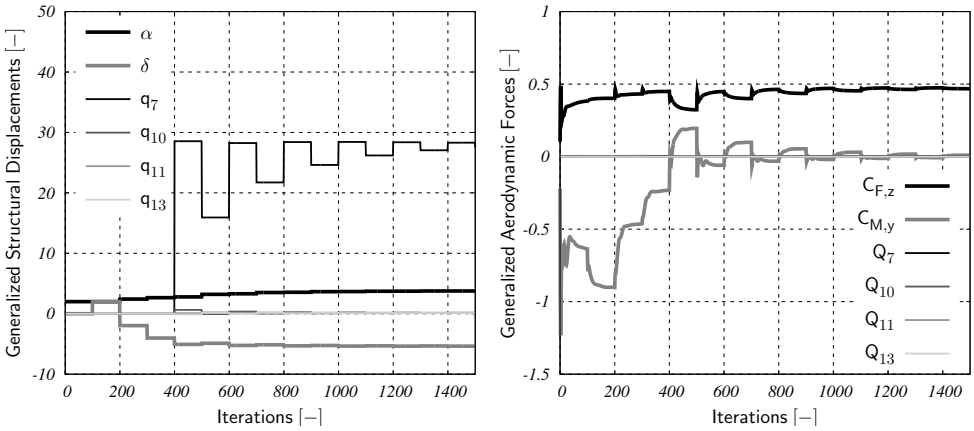

b) Discrete wing tip: pull at $M_\infty = 0.40$ and $n = 1.5$

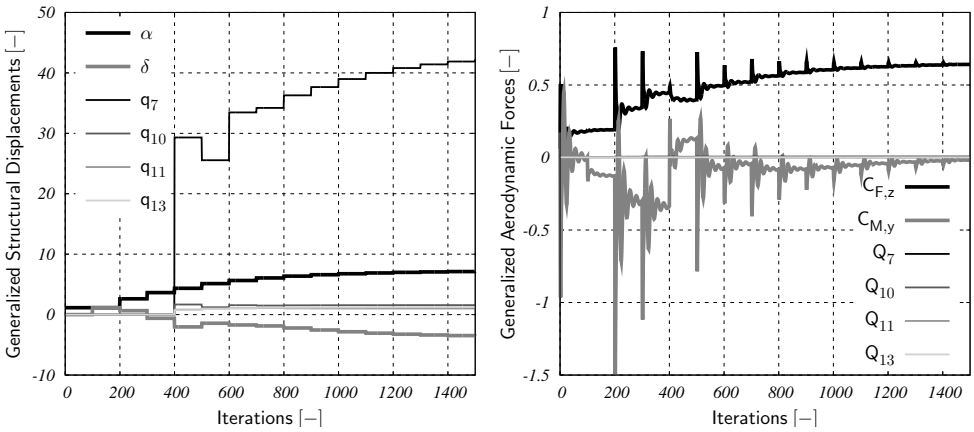

c) Raked wing tip: cruise at $M_\infty = 0.78$ and $n = 1$

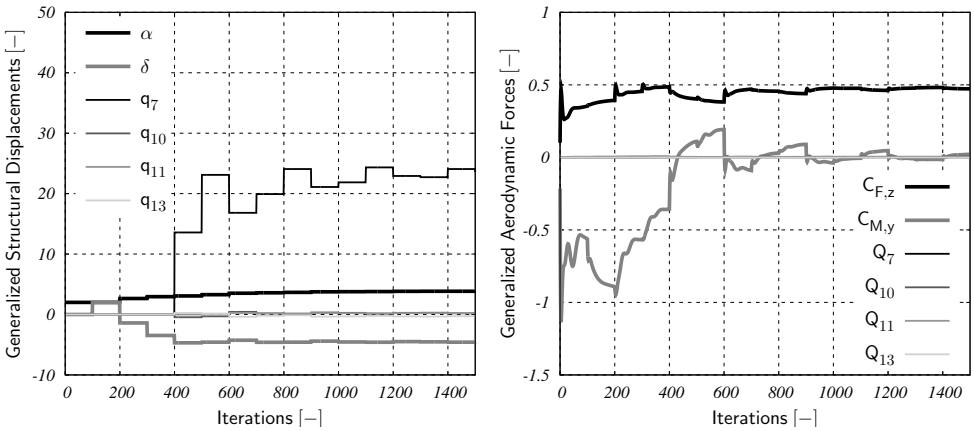

Figure 4.12: Convergence history of the generalized displacements (left) and the generalized aerodynamic forces (right) for test cases a), b) and c).

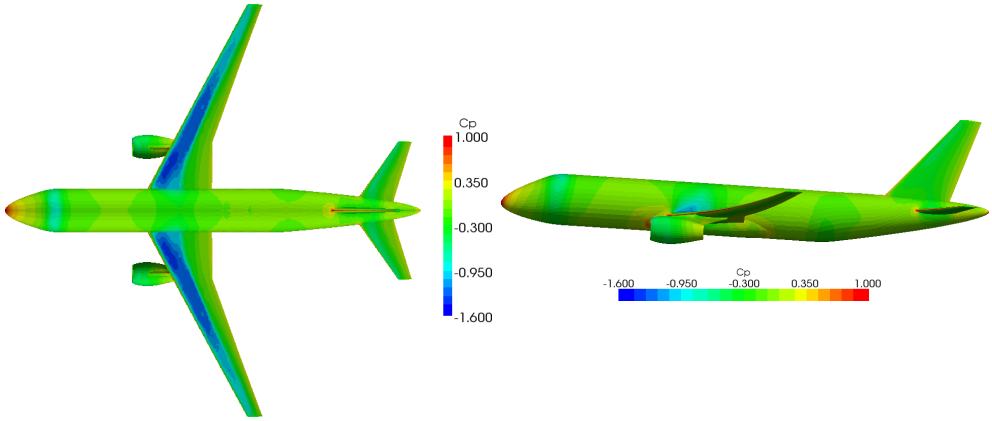

Figure 4.13: Top and side views of the pressure coefficient C_p contours for test case a).

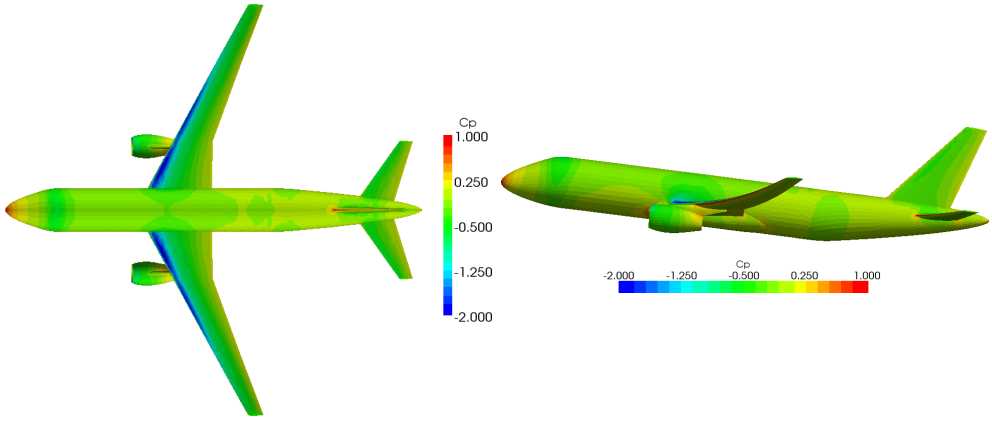

Figure 4.14: Top and side views of the pressure coefficient C_p contours for test case b).

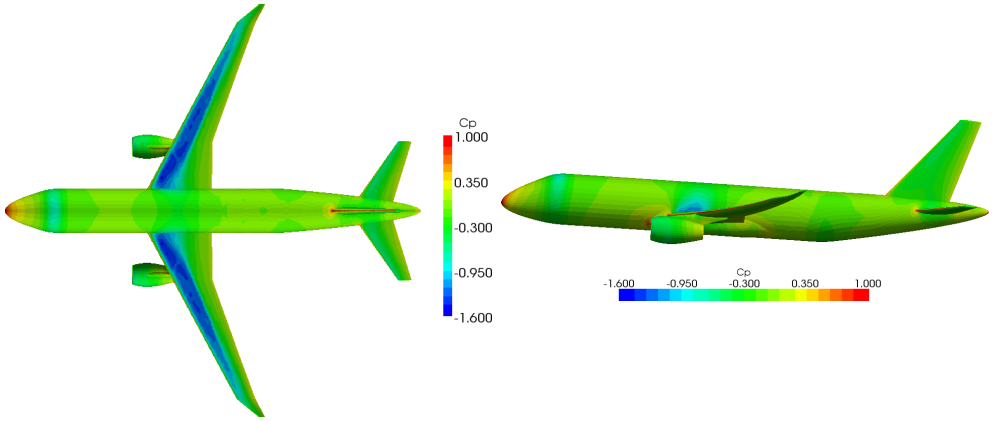

Figure 4.15: Top and side views of the pressure coefficient C_p contours for test case c).

Case	CFD	DLM	Error	Case	CFD	DLM	Error
a	3.80	4.83	21.3%	a	−5.37	−7.11	24.4%
a*	3.61	4.83	25.2%	a*	−5.71	−7.11	19.6%
b	7.31	8.25	11.4%	b	−3.79	−13.1	71.1%
c	3.88	4.81	19.3%	c	−4.54	−7.30	37.8%
	Pitch angle α [deg]				Elevator rotation δ [deg]		

Table 4.3: Comparison of the non-linear aeroelastic trim procedure for rigid d.o.f. α and δ for test cases a), a*) b) and c).

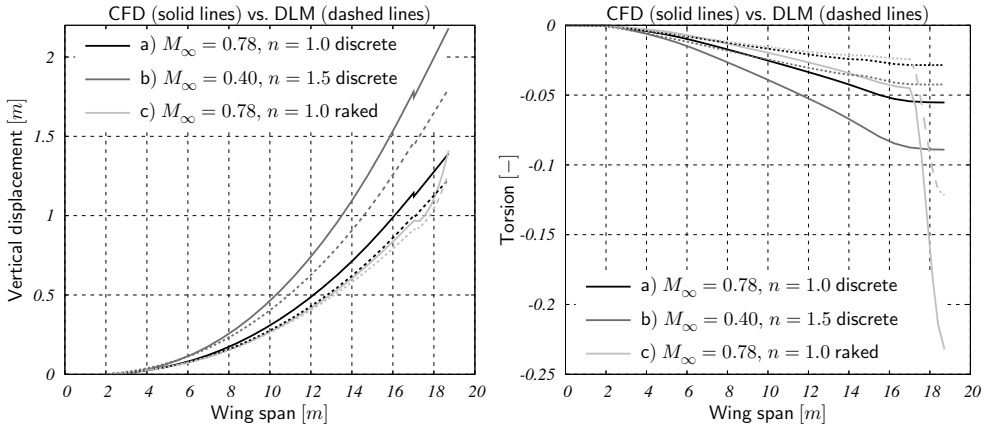

Figure 4.16: Comparison between AeroFoam (CFD) and Nastran (DLM) results for the bending (left) and torsional (right) deformation of the wing for test cases a), b) and c).

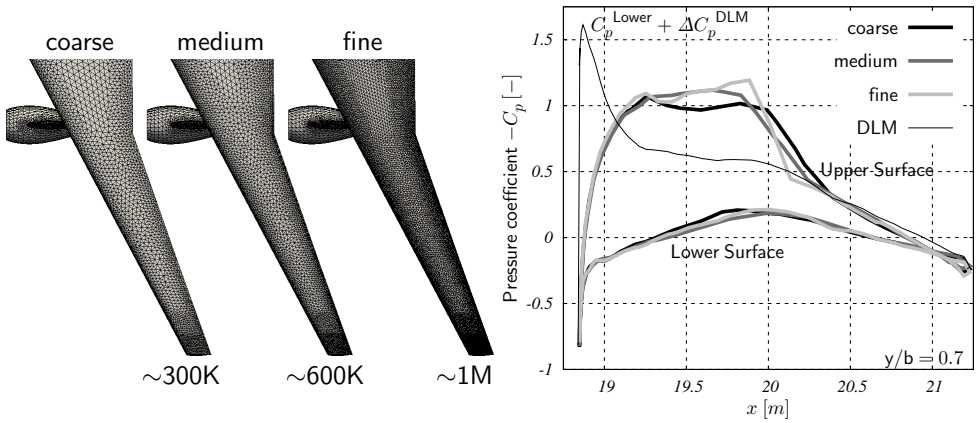

Figure 4.17: Convergence study on three progressively refined grids (left) of the distribution of the pressure coefficient C_p along a wing section at $y/b = 0.7$ for test case a) and comparison between AeroFoam (CFD) and Nastran (DLM) (right).

5

Dynamic aeroservoelasticity

This Chapter is aimed at assessing the credibility of the proposed aeroservoelastic analysis toolbox by tackling a set of dynamic aeroservoelastic problems and comparing the results with reference experimental and numerical data available in literature. The availability of such an integrated environment is almost mandatory from the very beginning of the design process. More in particular we investigate the sensitivity to different modelling options for representing the aerodynamic sub-system. In such a way it is easier to strike the best balance between accuracy of the results and computational efficiency, choosing within the hierarchy of tools available the lowest-fidelity Doublet Lattice Method (DLM) or the Non-Linear Full Potential (NLFP) equations or the Euler equations or the highest-fidelity Reynolds Averaged Navier-Stokes (RANS) equations.

In §5.1 the classical dynamic aeroelastic benchmark test problem of computing the transonic flutter boundary of the AGARD 445.6 wing is presented. More precisely, after providing an overview of the structural and aerodynamic models, we compute the reference equilibrium or "trim" configuration for the (numerical) linearization of the generalized aerodynamic forces. Successively we build the aerodynamic transfer functions matrix and we choose a root-tracking non-linear method for computing the so-called $V_\infty - \omega$ and $V_\infty - g$ diagrams. Such a procedure is repeated for different Mach numbers $M_\infty \in (0.678, 1.140)$ in order to cover the whole transonic regime. In §5.2 we illustrate an example aeroservoelastic problem of how to design a flutter suppression active control system to operate within the highly non-linear transonic regime with a linear, low-fidelity but efficient model and then verify the performances with a non-linear, high-fidelity but expensive model. This strategy yields a significant added value to the workflow since it makes possible to appreciate how important the neglected non-linear effects actually are and therefore the robustness of the designed active control system. More precisely we design a simple Proportional-Integral (PI) active control system by means of a multi-objective optimization strategy based on Genetic Algorithms (GA). Successively we compare the results of a post-flutter direct simulation with control system on and off with both the low and high-fidelity tools.

5.1 AGARD 445.6 wing

The objective of the present work is that of computing the so-called transonic flutter boundary (in terms of flutter velocity V_F and frequency ω_F) for the AGARD 445.6 wing. In order to cover the whole transonic regime, the following Mach numbers are considered $M_\infty \in (0.678, 0.901, 0.960, 1.072, 1.140)$. More in particular we are interested in the following adimensional Flutter Speed Index (FSI) and Frequency Ratio (FR):

$$\mathsf{FSI} = \frac{V_F}{L_a\,\omega_t\,\sqrt{\mu}} \qquad \text{and} \qquad \mathsf{FR} = \frac{\omega_F}{\omega_t}, \tag{5.1}$$

where L_a is the reference aerodynamic length, ω_t is the first torsional frequency and finally μ is the mass ratio. The numerical results of the multi-fidelity toolbox for aeroservoelastic analysis AeroFoam will be compared with the reference data available in literature relative to the experimental campaign carried out at NASA Transonic Dynamics Tunnel (TDT) back in 1961. [13]

Flutter data from such an experimental campaign have been publicly available for over 20 years and have been widely used for preliminary benchmarking of the sophisticated tools within the framework of Computational Aeroservoelasticity (CA). Unfortunately this data set lacks unsteady surface pressure measurements necessary for more extensive code validation. Such a benchmark test problem is of particular interest because in the transonic regime it is possible to observe a significant and sudden drop of the flutter velocity, the so-called transonic dip phenomenon. The classical, computationally efficient, linear(ized) numerical methods such as DLM do not yield reliable information. Nevertheless, after a survey of the numerical results available in literature, it is interesting to remark that also CFD tools significantly over-estimate the flutter velocity with respect to the experimental data, in particular for supersonic Mach numbers M_∞. A better understanding of such a trend is a further challenge. [20]

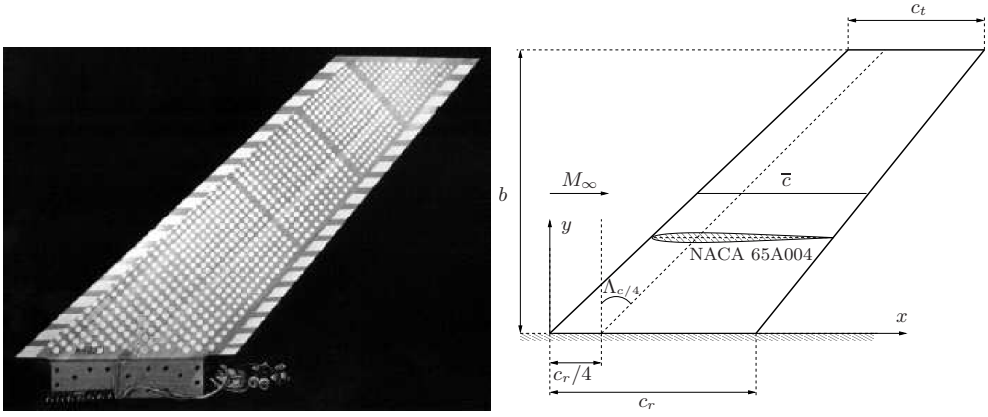

Figure 5.1: Experimental set-up for the AGARD 445.6 wing.

The AGARD 445.6 experimental set-up shown in Figure 5.1 is a sidewall-mounted, clean-wing configuration (weakened model No. 3) with a quarter-chord sweep angle $\Lambda_{c/4} = 45°$, a span $b = 0.762$ m, a root chord $c_r = 0.558$ m and a taper ratio $\lambda = 0.66$. The wing section is a NACA 65A004 airfoil.

5.1.1 Structural model

Below we present the numerical results of the problem of building the Finite Element (FE) structural model for the AGARD 445.6 wing which best fits the numerical and Ground Vibration Tests (GVT) data available in literature. [4, 13] More in particular we consider the experimental wall-mounted semi-span model No. 3 built in laminated mahogany and successively weakened (both in bending and torsion) by drilling holes through the wing normal to the chord plane and using a structurally non-cooperating plastic foam filler to preserve the smoothness of the wing surface. In the present work we assembly a FE structural model in Code_Aster discretizing the chord plane with $N_n = 121$ nodes and $N_e = 200$ homogeneous orthotropic triangular plate elements of density $\rho = 381.980$ kg/m^3, parallel and orthogonal Young's moduli $E_\parallel = 3.151 \cdot 10^9$ Pa and $E_\perp = 4.162 \cdot 10^8$ Pa respectively, tangential elastic modulus $G = 4.392 \cdot 10^8$ Pa and Poisson's coefficient $\nu = 0.310$. The thickness distribution $\{\boldsymbol{t}\}$ of the plate elements is automatically computed by means of an optimization utility based on Genetic Algorithms (GA). [37] The functional to be minimized is a weighted sum of the relative errors between the numerical and the experimental values of the first four dynamically relevant normal modes of vibration frequencies f_i and shapes $\boldsymbol{U}_i$, namely:

$$J(\{\boldsymbol{t}\}) = \sum_{i=0}^{4} W_{f_i} \frac{\|f_i^{\mathsf{FEM}} - f_i^{\mathsf{Exp}}\|}{\|f_i^{\mathsf{Exp}}\|} + \sum_{i=0}^{4} W_{\boldsymbol{U}_i} \frac{\|\boldsymbol{U}_i^{\mathsf{FEM}} - \boldsymbol{U}_i^{\mathsf{Exp}}\|}{\|\boldsymbol{U}_i^{\mathsf{Exp}}\|}. \tag{5.2}$$

Such an optimization procedure converges rapidly to a thickness distribution close to that of the NACA 65A004 airfoil, however with a significant relative error on the total wing mass $\|e_M\| = \|M^{\mathsf{FEM}} - M^{\mathsf{Exp}}\|/\|M^{\mathsf{Exp}}\| \simeq 8\%$. With reference to Table 5.1 and Figure 5.2 the natural frequencies and modal shapes of the resulting FE structural model are in satisfactory agreement with the experimental [13] and numerical [4] data available in literature, with maximum relative errors $\|e_{f_3}\|_{\mathrm{L}^1} \simeq 4\%$ and $\|e_{\boldsymbol{U}_3}\|_{\mathrm{L}^1} \simeq 5\%$ respectively. The experimental modal shapes are normalized to a unitary generalized mass of 1 lbf in/s^2 = 175.125 kg in imperial units. Therefore it is recommended to rescale the modal shapes in order to achieve a unitary generalized mass of 1 kg.

Mode	$\boldsymbol{f}^{\mathsf{Exp}}$ [Hz]	$\boldsymbol{f}^{\mathsf{FEM}}$ [Hz]	**Error**	$\boldsymbol{f}^{\mathsf{FEM}}$ [Hz]	**Error**	**Description**
1	9.60	9.46	1.45%	9.57	0.30%	1$^{\mathrm{st}}$ bending
2	38.17	39.44	3.32%	39.28	2.90%	1$^{\mathrm{st}}$ torsion
3	48.35	49.71	2.81%	50.35	4.15%	2$^{\mathrm{nd}}$ bending
4	91.54	94.39	3.11%	93.63	2.10%	2$^{\mathrm{nd}}$ torsion
		Nastran [4]		Code_Aster [74]		

Table 5.1: Modal bases used for the transonic flutter analysis of AGARD 445.6 wing.

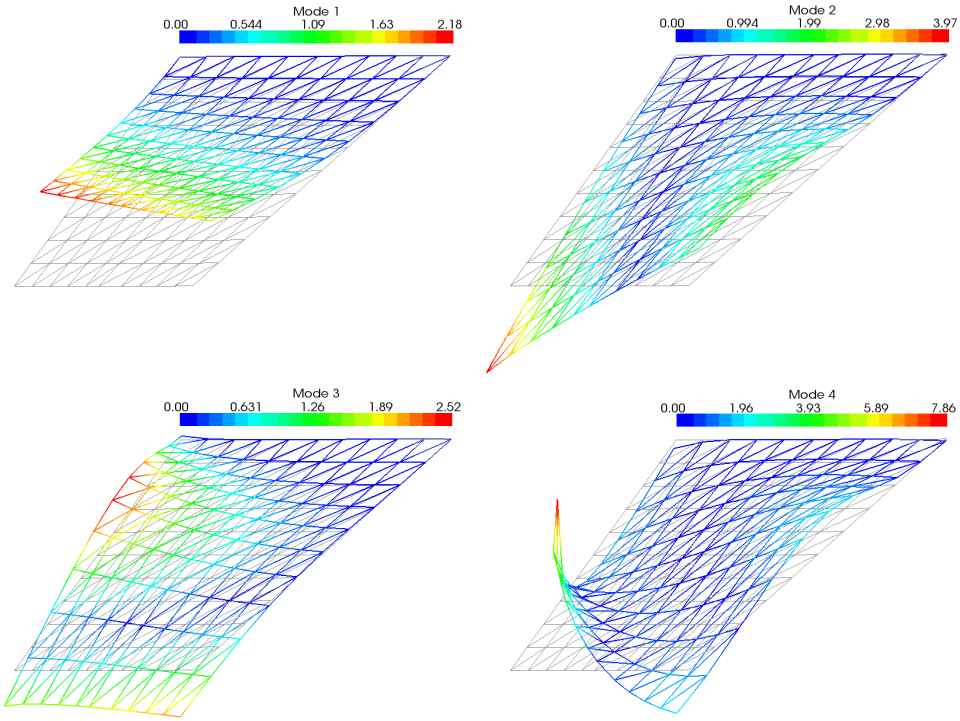

Figure 5.2: First four dynamically relevant modal shapes $\boldsymbol{U}_i$ of AGARD 445.6 wing.

5.1.2 Aerodynamic model

Concerning the aerodynamic model the objective is that of performing a comparison between the numerical results of Euler and RANS simulations. More in particular we choose the Spalart-Allmaras turbulence model popular within the aeronautical industry. In order to speed-up the convergence to the steady-state within each outer iteration of the Dual Time-Stepping (DTS) procedure a 3 levels Multi-Grid (MG) acceleration driver is used in combination with a 5 steps Explicit Runge-Kutta (ERK) time-stepping scheme and Implicit Residual Smoothing (IRS).

To quantify the computational effort, for the Euler runs we use an aerodynamic mesh with $N_{a,\,b} = 4992$ boundary faces and $N_{a,\,v} = 358840$ hexahedral cells while for the RANS runs we use an aerodynamic mesh with $N_{a,\,b} = 4992$ boundary faces and $N_{a,\,v} = 531704$ hexahedral cells as shown in Figure 5.3. The number of boundary d.o.f. is identical for both inviscid and viscous simulations, but the number of volume d.o.f. is significantly higher for viscous simulations in order to accurately resolve the boundary layer close to the wing surface. More in particular the growth ratio of the mesh size in the direction normal to the wing surface is suitably chosen in such a way that the threshold on the adimensional wall distance of the first near-wall cell $y^+ \leq 50$ is satisfied, as recommended when dealing with wall-functions boundary conditions.

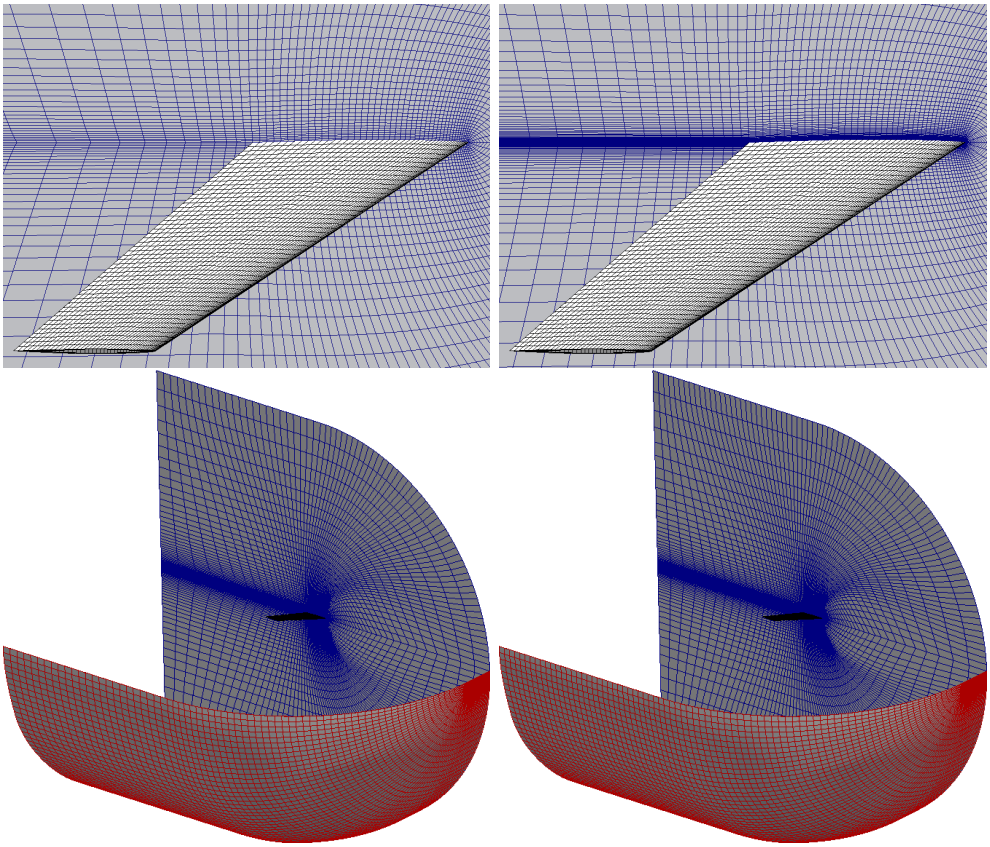

Figure 5.3: Surface aerodynamic meshes for the AGARD 445.6 wing for Euler (left) and RANS (right) simulations. It is possible to appreciate the higher resolution in the boundary layer. The infinity (●), symmetry (●) and wing (●) boundary patches are highlighted.

Nevertheless, decomposing the problem on 16 Intel Xeon X5650 processors, a time-accurate unsteady numerical simulation of the variation of the array of the generalized aerodynamic forces due to a prescribed excitation time history applied to each j-th generalized d.o.f. requires 1 and 20 hours for Euler and RANS cases respectively. Such an imbalance of the computational costs between inviscid and viscous simulations is related to the difficulty of driving the residuals of turbulent variables below $\varepsilon \leq 10^{-3}$.

5.1.3 Trim analysis

Below we illustrate the results of the trim analysis for the AGARD 445.6 wing, which corresponds to the reference equilibrium or "trim" configuration for the (numerical) linearization of the generalized aerodynamic forces. In the present work the geometry and the boundary conditions of the AGARD 445.6 wing are symmetric and therefore the reference equilibrium solution does not involve any structural deformability.

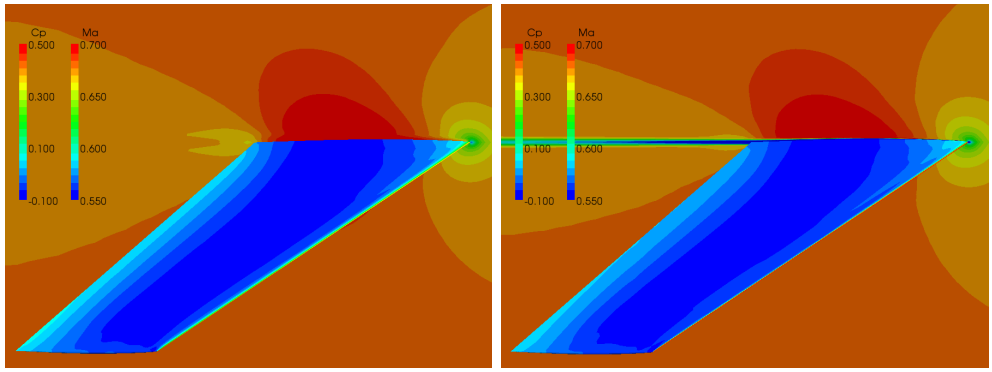

Figure 5.4: Comparison of the contours of the pressure coefficient C_p and the local Mach number M between Euler (left) and RANS (right) simulations for $M_\infty = 0.678$ and $\alpha = 0°$.

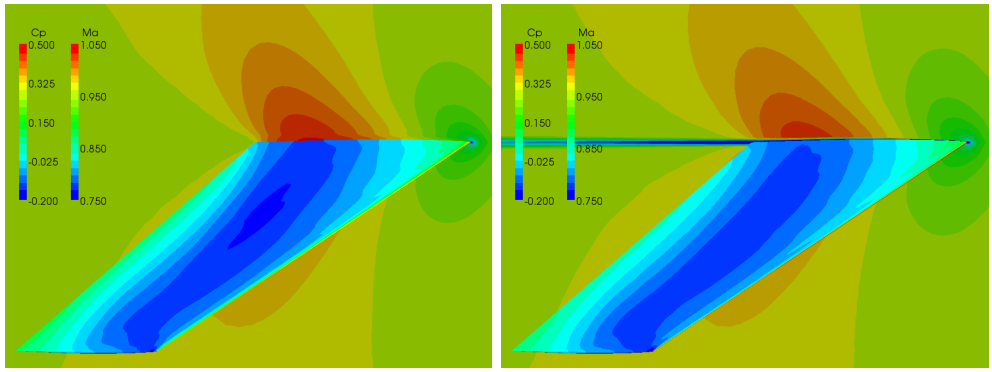

Figure 5.5: Comparison of the contours of the pressure coefficient C_p and the local Mach number M between Euler (left) and RANS (right) simulations for $M_\infty = 0.960$ and $\alpha = 0°$.

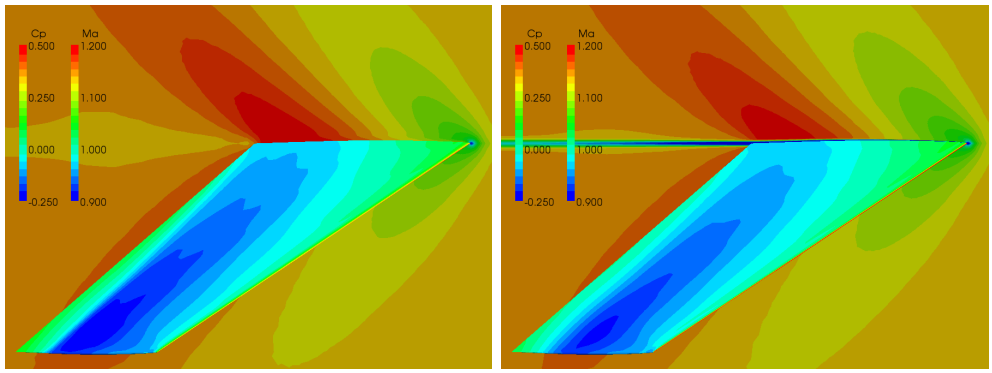

Figure 5.6: Comparison of the contours of the pressure coefficient C_p and the local Mach number M between Euler (left) and RANS (right) simulations for $M_\infty = 1.140$ and $\alpha = 0°$.

Case	**Mean μ**	**Variance σ^2**	**Case**	**Mean μ**	**Variance σ^2**
a	0.5011	$6.708 \cdot 10^{-4}$	a	0.5013	$4.243 \cdot 10^{-4}$
c	0.5052	$2.958 \cdot 10^{-4}$	c	0.5035	$1.299 \cdot 10^{-4}$
e	0.5057	$2.131 \cdot 10^{-4}$	e	0.5042	$1.232 \cdot 10^{-4}$
	Euler			RANS	

Table 5.2: Comparison between Euler (left) and RANS (right) results for the dynamic linearity benchmarks in terms of mean value μ and variance σ^2 of the ratio $H(t) = Q_1^*(t)/Q_1(t)$.

In Figures 5.4-5.6 the contours of the pressure coefficient C_p and the local Mach number M for the AGARD 445.6 wing at $\alpha = 0°$ are shown only for the minimum, intermediate and maximum Mach numbers within the matrix of test cases here considered, that is: a) with $M_\infty = 0.678$, c) with $M_\infty = 0.960$ and e) with $M_\infty = 1.140$. More in particular it is possible to compare the numerical results of Euler and RANS modelling options. Of course a remarkable difference between inviscid and viscous simulations is the appearance of the boundary layer and wake regions. However, because of the extremely small thickness of the airfoil the differences are qualitatively minimal especially for $M_\infty = 0.678$ but it is is possible to appreciate more and more changes between Euler and RANS runs as the Mach number is increased.

Moreover it is recommended to perform suitable dynamic linearity benchmarks in order to precisely define what we mean with "small" before moving to the (numerical) linearization of the generalized aerodynamic forces due to the structural motion. To this end we compute the unsteady variation of the generalized aerodynamic force $Q_1(t)$ due to a blended step excitation time history prescribed only to the generalized displacement $q_1(t)$. We repeat such an experiment, this time doubling the amplitude of the input signal, namely: $q_1^*(t) = 2\,q_1(t)$, and storing the corresponding unsteady variation of the generalized aerodynamic force $Q_1^*(t)$. Of course for a linear system the ratio $H(t) = Q_1^*(t)/Q_1(t) = 1/2$. Such a ratio is a suitable indicator for monitoring if the chosen input signal is well above the numerical error threshold but without triggering non-linearities, thus jeopardizing the hypothesis of small perturbations. More quantitative data can be found in Table 5.2 with a comparison of the mean value μ and the variance σ^2 of the ratio $H(t)$ evaluated with Euler and RANS modelling options. It is interesting to remark that the relative error increases while the variance decreases with the Mach number. Moreover it is possible to conclude that the chosen threshold $\varepsilon = \tan 1°$ does not trigger significant non-linearities.

5.1.4 Flutter analysis

Below we illustrate the results of the (numerical) linearization of the generalized aerodynamic forces due to the structural motion about the reference equilibrium or "trim" configuration and the identification of the aerodynamic transfer functions matrix. Eventually it is possible to carry out the flutter analysis for the AGARD 445.6 wing. For brevity we only present the results for test cases a), c) and e) and we focus on the first two generalized d.o.f. only.

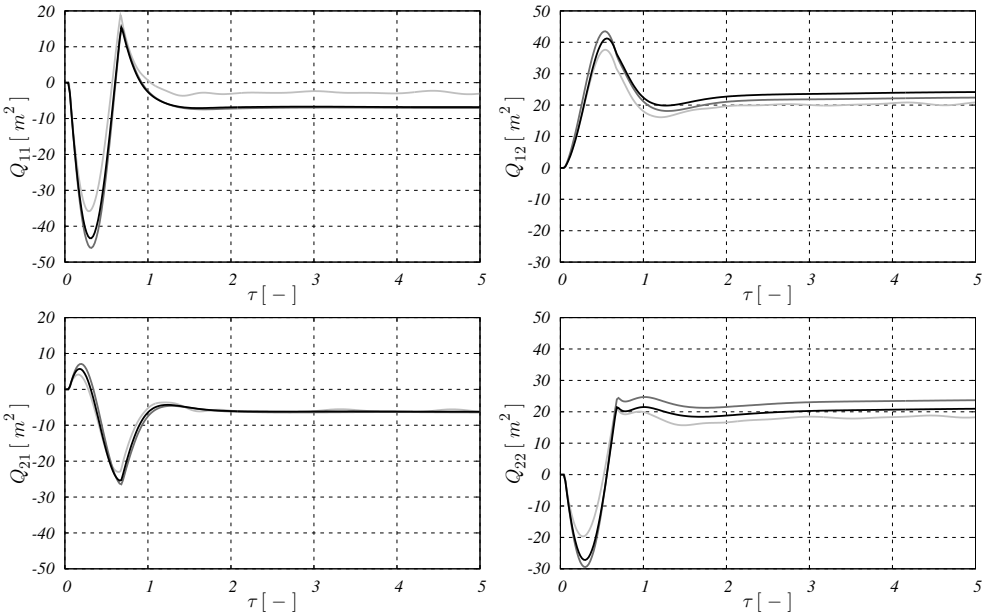

Figure 5.7: Comparison of the unsteady generalized aerodynamic forces $\{\boldsymbol{Q}^a(t)\}$ computed with NLFP (●), Euler (●) and RANS (●) modelling options at $M_\infty = 0.678$.

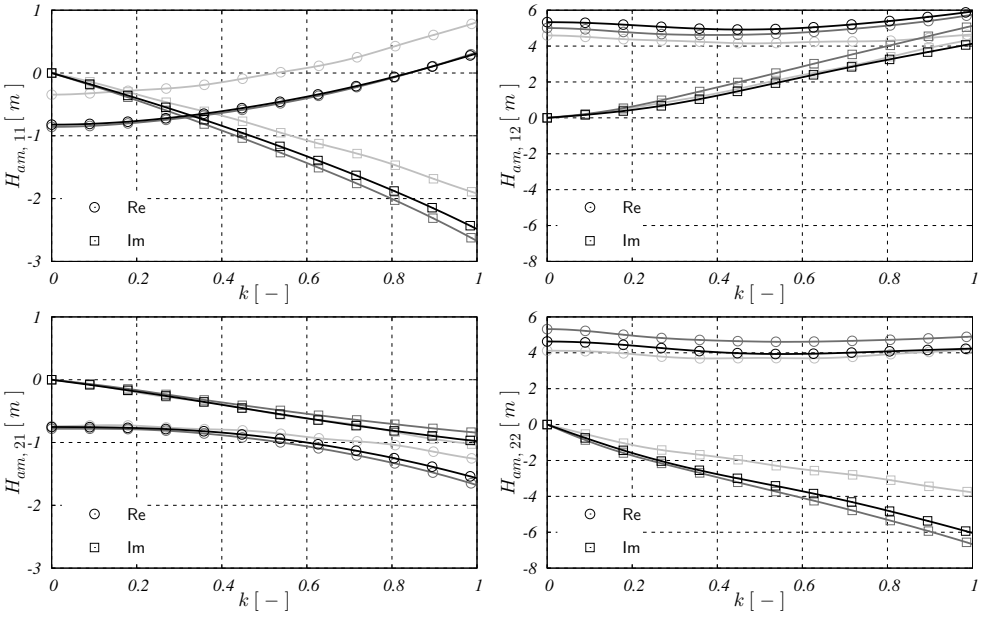

Figure 5.8: Comparison of the aerodynamic transfer functions matrix $[\,\boldsymbol{H}_{am}(k)\,]$ computed with NLFP (●), Euler (●) and RANS (●) modelling options at $M_\infty = 0.678$.

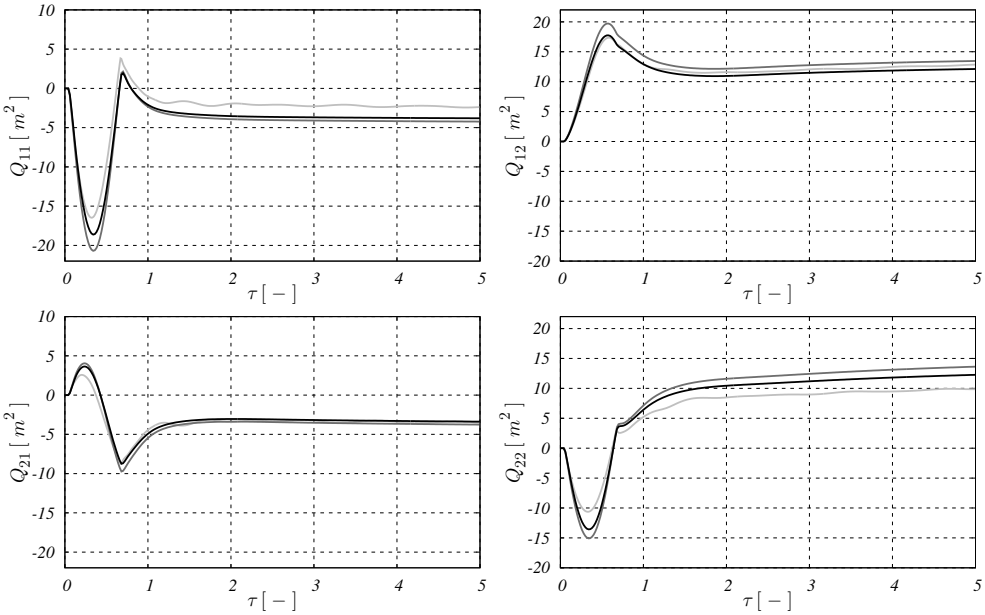

Figure 5.9: Comparison of the unsteady generalized aerodynamic forces $\{\boldsymbol{Q}^a(t)\}$ computed with NLFP (●), Euler (●) and RANS (●) modelling options at $M_\infty = 0.960$.

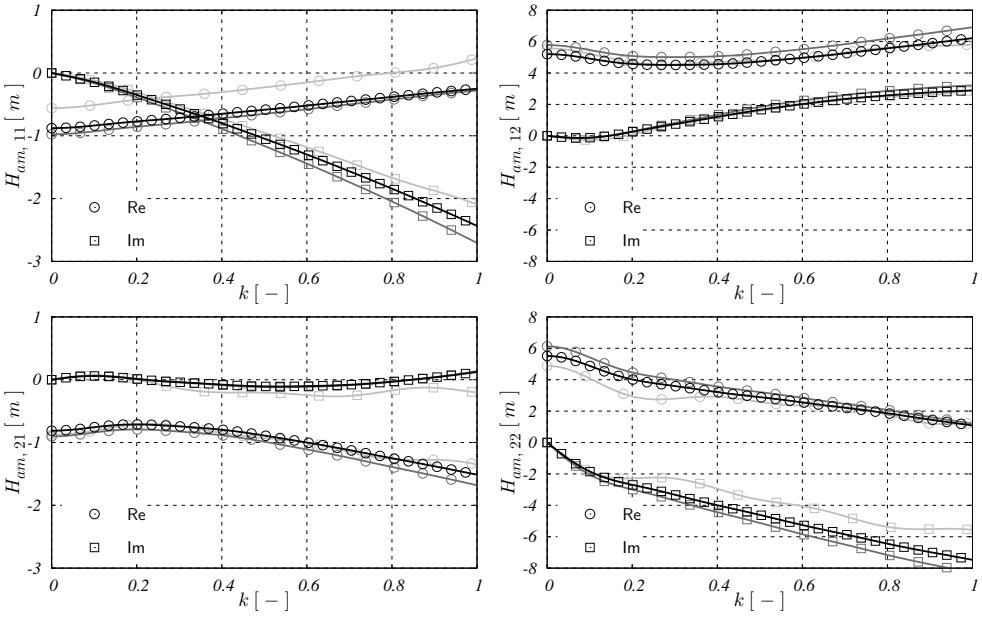

Figure 5.10: Comparison of the aerodynamic transfer functions matrix $[\,\boldsymbol{H}_{am}(k)\,]$ computed with NLFP (●), Euler (●) and RANS (●) modelling options at $M_\infty = 0.960$.

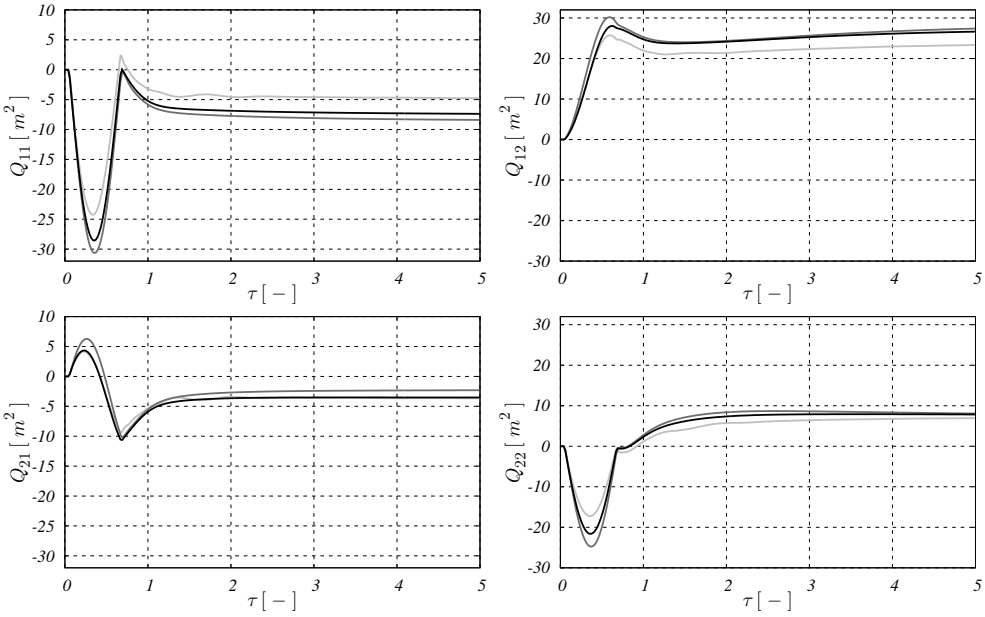

Figure 5.11: Comparison of the unsteady generalized aerodynamic forces $\{\boldsymbol{Q}^a(t)\}$ computed with NLFP (●), Euler (●) and RANS (●) modelling options at $M_\infty = 1.140$.

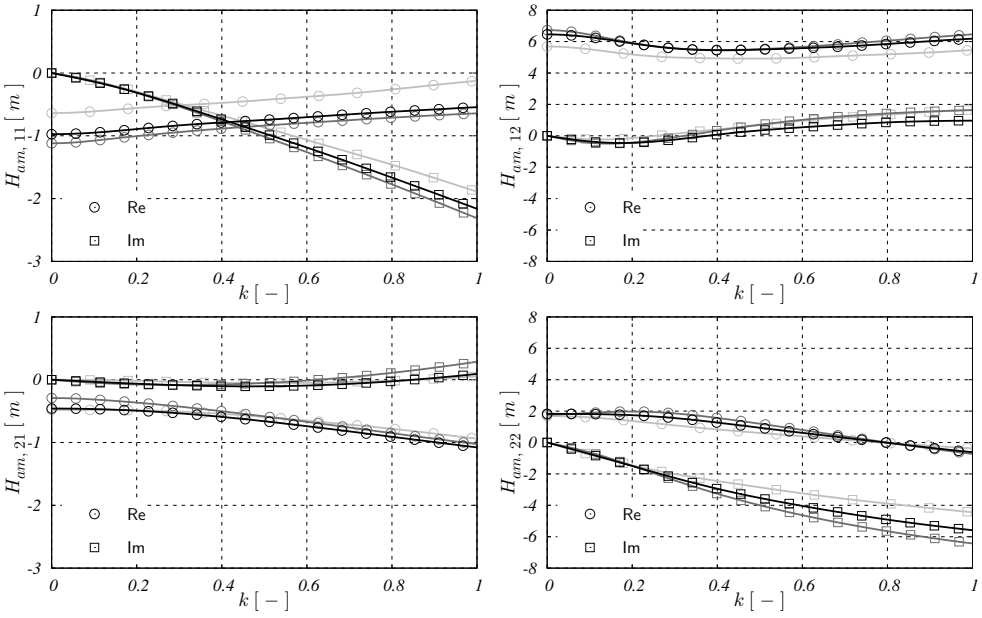

Figure 5.12: Comparison of the aerodynamic transfer functions matrix $[\,\boldsymbol{H}_{am}(k)\,]$ computed with NLFP (●), Euler (●) and RANS (●) modelling options at $M_\infty = 1.140$.

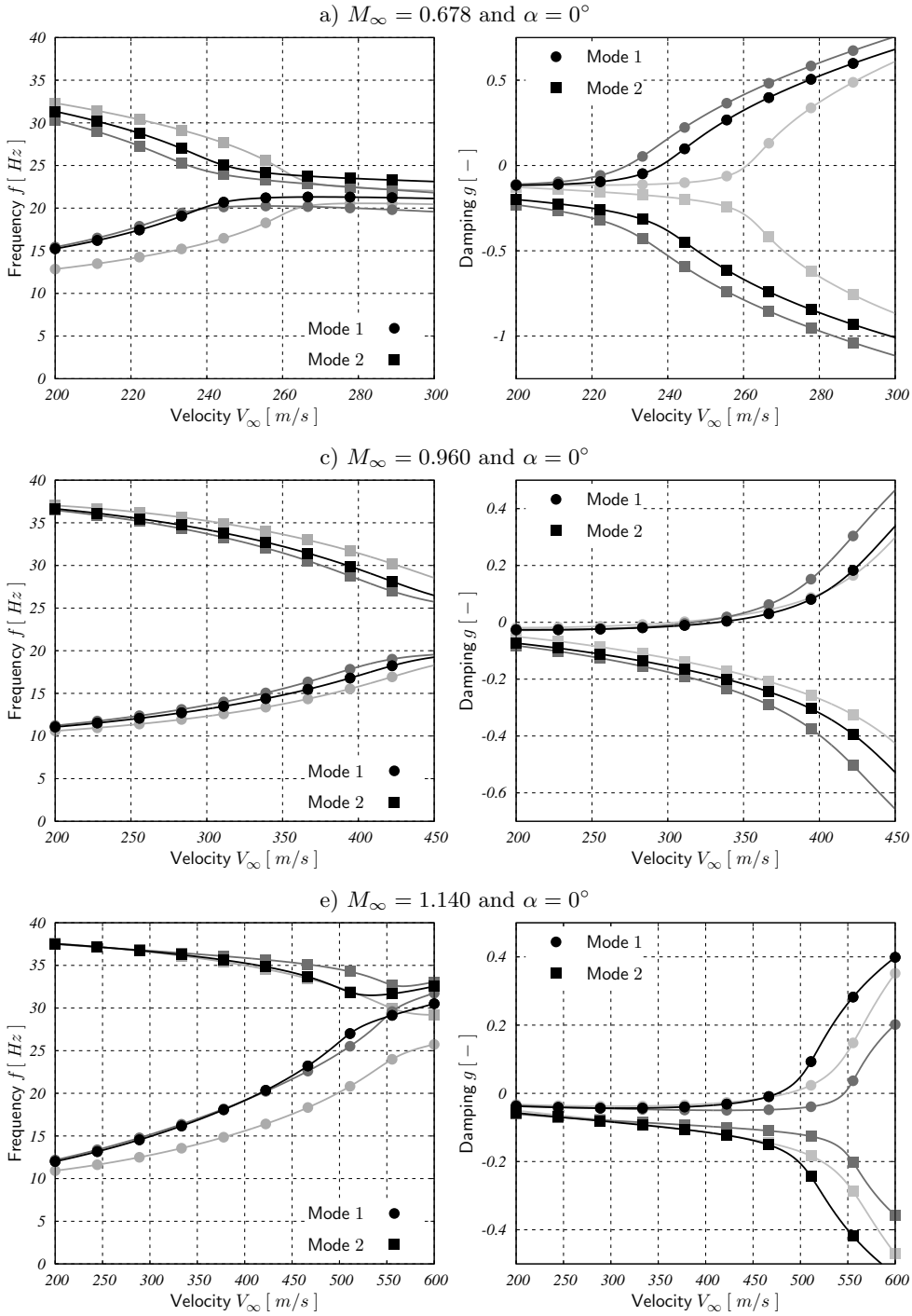

Figure 5.13: Comparison of the $V_\infty - \omega$ (left) and $V_\infty - g$ (right) diagrams computed with NLFP (●), Euler (●) and RANS (●) modelling options.

In Figures 5.7, 5.9 and 5.11 the unsteady variation of the array of the generalized aerodynamic forces $\{\boldsymbol{Q}^a(\tau)\}$ due to a blended step excitation time history of the array of the generalized coordinates $\{\boldsymbol{q}(\tau)\}$ is presented as a function of the adimensional time $\tau = t\,V_\infty/L_a$ only for test cases a), c) and e). With such data it is possible to assembly the aerodynamic transfer functions matrix $[\,\boldsymbol{H}_{am}(k)\,]$ as a function of the reduced frequency $k = \omega L_a/V_\infty$, as shown in Figures 5.8, 5.10 and 5.12. More in particular it is possible to compare the numerical results of NLFP, Euler and RANS modelling options. It is worthwhile to remark that the differences between inviscid and viscous simulations are minimal, with slightly higher dampings in the latter case. Viceversa the gap between Euler data and the numerical results of NLFP modelling option becomes more and more remarkable as the Mach number is increased.

In Figure 5.13 the $V_\infty - \omega$ and $V_\infty - g$ diagrams built resorting to a suitable PK approximation and non-linear root-tracking method are presented only for test cases a), c) and e). It is interesting to observe that near-by the flutter point the bending and torsional frequencies in the $V_\infty - \omega$ diagrams tend to coalesce. Moreover it is worthwhile to remark that for test cases a) and c) with subsonic Mach numbers the flutter point predicted with RANS modelling option falls in-between the numerical results associated with NLFP and Euler runs. Such a pattern is reversed for test case e) with supersonic Mach number.

Finally in Figure 5.14 the adimensional Flutter Speed Index (FSI) and Frequency Ratio (FR) computed with NLFP, Euler and RANS modelling options are plotted as a function of Mach number M_∞ and compared with the reference experimental and numerical data available in literature. It is interesting to remark that for subsonic Mach numbers Euler and RANS modelling options yield fairly accurate results. Viceversa for supersonic Mach numbers the flutter point is significantly overpredicted by Euler and even if to a lesser extent also by RANS simulations. For $M_\infty = 1.140$ it is remarkable that NLFP modelling option apparently yields better results than both Euler and RANS simulations.

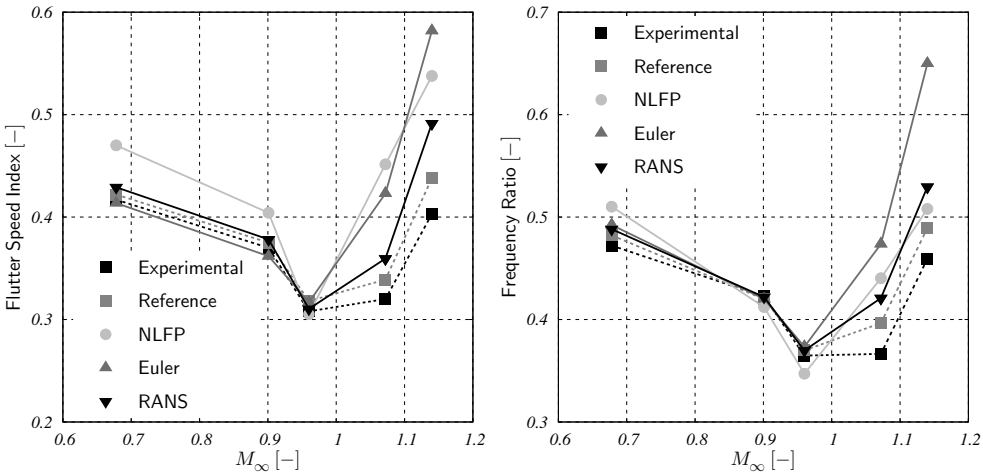

Figure 5.14: Comparison with reference experimental data of Flutter Speed Index (FSI) (left) and Frequency Ratio (FR) (right) for NLFP, Euler, RANS modelling options.

5.2 BACT wing

Active control of aeroservoelastic phenomena, especially in the transonic flow regime, is a key technology for the design of future aircraft. The Benchmark Active Controls Technology (BACT) project is part of NASA Langley Research Center Benchmark Models Program for studying transonic aeroservoelastic phenomena. For instance the BACT wind-tunnel model was developed to collect high quality unsteady aerodynamic data (pressures and loads) near transonic flutter conditions and demonstrate the potential of designing and implementing active control systems for flutter suppression using flaps and spoilers. [88]

As shown in Figure 5.15 the BACT wind-tunnel model is a rigid rectangular wing with a NACA 0012 airfoil section. It is equipped with a trailing-edge control surface and upper and lower-surface spoilers that can be controlled independently by means of hydraulic actuators. The wind-tunnel model is instrumented with pressure transducers, accelerometers, control surface position sensors, and hydraulic pressure transducers. The accelerometers are the primary sensors for feedback control and are located at each corner of the wing. The wing is mounted to a device called the Pitch and Plunge Apparatus (PAPA) which is designed to permit motion in principally two modes, rotation (or pitch) and vertical translation (or plunge). The mass, inertia, and center of gravity location of the system can be controlled by locating masses at various points along the mounting bracket. The stiffness properties can be controlled by changing the properties of the rods. The PAPA is instrumented with strain gauges to measure normal force and pitching moment and it is mounted to a turntable that can be rotated to control the wing angle of attack. The combination of the BACT wing section and PAPA mount will be referred to as and it was precisely tuned to flutter within the operating range of the Transonic Dynamics Tunnel (TDT) at NASA Langley Research Center

The BACT system has dynamic behavior very similar to the classical 2 d.o.f. wing section. The difference is primarily the complexity of the aerodynamic behaviour and the presence of additional structural modes. The finite span and low aspect ratio of the BACT wing introduce significant three-dimensional flow effects. Higher frequency structural degrees of freedom are associated with the PAPA mount and the fact that the wing section is not truly rigid. The control surfaces also introduce complexities not typically reflected in the classical 2 d.o.f. system. The mass and inertia of the control surfaces and potential flexibility in their support structures introduce inertial

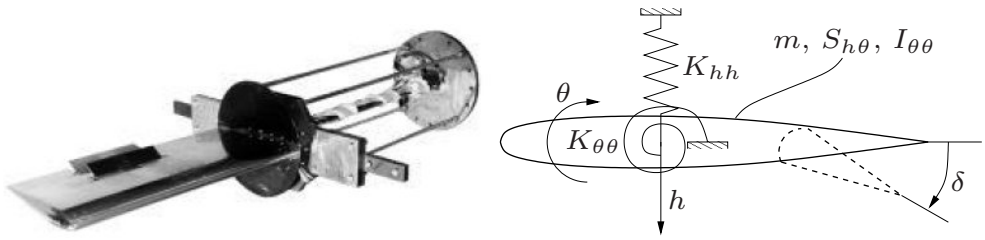

Figure 5.15: Experimental set-up for the BACT wing.

coupling effects. The finite span of the control surfaces and their close proximity to each other also introduce significant aerodynamic effects. All these issues influence the development of the equations of motion but, as will be seen, do not force the abandonment of the 2 d.o.f. system structure.

The objective of the present work is to design a flutter suppression active control system for the BACT wing to operate within the highly non-linear transonic regime with a linear, low-fidelity but efficient model and then verify the performances with a non-linear, high-fidelity but expensive model (surveying both Euler and RANS modelling options). More precisely we design a simple Proportional-Integral (PI) active control system by means of a multi-objective optimization strategy based on Genetic Algorithms (GA). Successively we compare the results of post-flutter direct simulations with control system on and off with both the low and high-fidelity tools. Preliminarly we stick to a two-dimensional approximation also for the high fidelity model. Of course further three-dimensional high-fidelity direct simulations are required in order to fully assess the potential of the proposed flutter suppression strategy.

5.2.1 Low-fidelity model

For the design of active control systems it is convenient to adopt an approximated and efficient numerical model with a small number of d.o.f. providing satisfactory results within the frequency range of interest, rather than choosing an over-detailed and expensive numerical model. To this end the BACT wing and each control surface are assumed to be rigid in both the spanwise and chordwise directions. This assumption is supported by the fact that the wing and control surfaces were constructed to be as rigid as possible. It is also assumed that the motion is limited to the 2 d.o.f. of pitch and plunge. This assumption implies that the other structural modes of the BACT wing are not significant. Investigation of the structural vibration characteristics of the PAPA mount was shown to support this assumption. In fact the next lowest frequency for any transverse mode was more than six times the frequency of the pitch and plunge modes and well outside the frequency range of interest. [88]

Within such a framework the structural model for the BACT wing can be written as the following system of Ordinary Differential Equations (ODE) in the unknown generalized coordinates $\{\boldsymbol{q}(t)\} = \{h(t),\, \theta(t)\}^{\mathsf{T}}$:

$$[\,\mathbf{M}\,]\,\{\ddot{\boldsymbol{q}}\} + [\,\mathbf{C}\,]\,\{\dot{\boldsymbol{q}}\} + [\,\mathbf{K}\,]\,\{\boldsymbol{q}\} = \{\boldsymbol{Q}_a(t)\} + \{\boldsymbol{Q}_c(t)\}, \tag{5.3}$$

where the structural mass, damping and stiffness matrices $[\,\mathbf{M}\,]$, $[\,\mathbf{C}\,]$ and $[\,\mathbf{K}\,] \in \mathbb{R}^{2\times 2}$ can be written as follows:

$$\begin{aligned}
[\,\mathbf{M}\,] &= \begin{bmatrix} m & S_{h\theta} \\ S_{h\theta} & I_{\theta\theta} \end{bmatrix} \\
[\,\mathbf{C}\,] &= \begin{bmatrix} C_{hh} & 0 \\ 0 & C_{\theta\theta} \end{bmatrix} = \begin{bmatrix} 2\,m\,\zeta_h\,\omega_h & 0 \\ 0 & 2\,I_{\theta\theta}\,\zeta_\theta\,\omega_\theta \end{bmatrix} \\
[\,\mathbf{K}\,] &= \begin{bmatrix} K_{hh} & 0 \\ 0 & K_{\theta\theta} \end{bmatrix} = \begin{bmatrix} m\,\omega_h^2 & 0 \\ 0 & I_{\theta\theta}\,\omega_\theta^2 \end{bmatrix},
\end{aligned} \tag{5.4}$$

where $m = 88.73$ kg is the mass, $S_{h\theta} = 6.31 \cdot 10^{-2}$ kg m the static unbalance and $I_{\theta\theta} = 3.79$ kg m^2 the moment of inertia of the BACT wing. The structural natural frequencies and damping coefficients for the plunge and pitch d.o.f. respectively are $\omega_h = 21.01$ rad/s, $\omega_\theta = 32.72$ rad/s, $\zeta_h = 1.4 \cdot 10^{-3}$ and $\zeta_\theta = 10^{-3}$.

Similarly the aerodynamic model for the BACT wing is based on a quasi-steady linear(ized) approximation of the array of the Generalized Aerodynamic Forces (GAF) due to structural motion $\{\boldsymbol{Q}_a(t)\}$ and control surfaces deflection $\{\boldsymbol{Q}_c(t)\}$ respectively, with stability and control derivatives computed by means of a Finite Differences (FD) strategy from wind tunnel experimental data measured at $M_\infty = 0.77$ and $q_\infty = 6846.84$ Pa, namely:

$$\begin{aligned} \{\boldsymbol{Q}_a\} &= \frac{L_a^2}{V_\infty^2} [\,\mathbf{M}_a\,] \{\ddot{\boldsymbol{q}}\} + \frac{L_a}{V_\infty} [\,\mathbf{C}_a\,] \{\dot{\boldsymbol{q}}\} + [\,\mathbf{K}_a\,] \{\boldsymbol{q}\} \\ \{\boldsymbol{Q}_c\} &= [\,\mathbf{M}_c\,] \ddot{\delta} + \frac{L_a}{V_\infty} [\,\mathbf{C}_c\,] \dot{\delta} + [\,\mathbf{K}_c\,] \delta, \end{aligned} \tag{5.5}$$

where the aerodynamic mass, damping and stiffness matrices associated with the structural motion $[\,\mathbf{M}_a\,]$, $[\,\mathbf{C}_a\,]$, $[\,\mathbf{K}_a\,] \in \mathbb{R}^{2\times 2}$ and with the control surfaces deflection $[\,\mathbf{M}_c\,]$, $[\,\mathbf{C}_c\,]$, $[\,\mathbf{K}_c\,] \in \mathbb{R}^{2\times 1}$ can be written as follows:

$$\begin{aligned} [\,\mathbf{M}_a\,] &= q_\infty \frac{2\,S}{c} \begin{bmatrix} -C_{L/\dot{\alpha}} & -\ell\, C_{L/\dot{\alpha}} \\ c\, C_{M/\dot{\alpha}} & c\,\ell\, C_{M/\dot{\alpha}} \end{bmatrix} & [\,\mathbf{M}_c\,] &= - \begin{bmatrix} S_{h\delta} \\ S_{\theta\delta} \end{bmatrix} \\ [\,\mathbf{C}_a\,] &= q_\infty \frac{2\,S}{c} \begin{bmatrix} -C_{L/\alpha} & -\ell\, C_{L/\alpha} \\ c\, C_{M/\alpha} & c\,\ell\, C_{M/\alpha} \end{bmatrix} & [\,\mathbf{C}_c\,] &= q_\infty\, S \begin{bmatrix} -C_{L/\dot{\delta}} \\ c\, C_{M/\dot{\delta}} \end{bmatrix} \\ [\,\mathbf{K}_a\,] &= q_\infty\, S \begin{bmatrix} 0 & -C_{L/\alpha} \\ 0 & c\, C_{M/\alpha} \end{bmatrix} & [\,\mathbf{K}_c\,] &= q_\infty\, S \begin{bmatrix} -C_{L/\delta} \\ c\, C_{M/\delta} \end{bmatrix} \end{aligned} \tag{5.6}$$

where $c = 0.4053$ m is the chord, $S = 0.3298$ m^2 is the surface and $\ell = -0.1750$ is the relative distance between the elastic axis and the aerodynamic center of the BACT wing. The aerodynamic reference length is here considered equal to half the aerodynamic chord, namely: $L_a = c/2$. Finally the stability and control derivatives evaluated experimentally are tabulated in literature. [88] The need to include more sophisticated aerodynamic modelling options such as unsteady kernel approximations or time accurate CFD is albeit mitigated by the fact that the reduced frequency for the BACT wing is relatively low, approximately $k \simeq 0.05$.

As discussed above the primary objective of the present work is that of assessing the dynamic stability properties of the BACT wing by computing the flutter velocity V_F. More in general it is convenient to investigate the behaviour of the eigenvalues of the aeroservoelastic system $s = \sigma + \boldsymbol{i}\omega$ as a function of the the flight velocity V_∞. Below we illustrate the results of the non-linear root-tracking procedure of Eq. (2.65) for automatically building the $V_\infty - \omega$ and $V_\infty - g$ diagrams as applied to the following matrix, resulting from the quasi-steady approximation presented above:

$$[\,\mathbf{A}(s, V_\infty)\,] = s^2 \left([\,\mathbf{M}\,] - \frac{L_a^2}{V_\infty^2} [\,\mathbf{M}_a\,] \right) + s \left([\,\mathbf{C}\,] - \frac{L_a}{V_\infty} [\,\mathbf{C}_a\,] \right) + \left([\,\mathbf{K}\,] - [\,\mathbf{K}_a\,] \right). \tag{5.7}$$

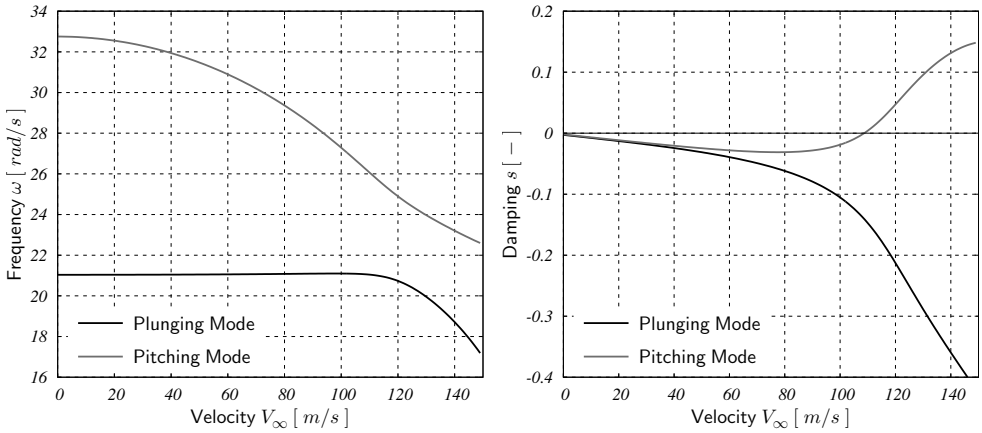

Figure 5.16: $V_\infty - \omega$ and $V_\infty - g$ diagrams for the BACT wing.

In Figure 5.16 the $V_\infty - \omega$ and $V_\infty - g$ diagrams for the BACT wing are presented. It is interesting to observe that near-by the flutter point the bending and torsional frequencies in the $V_\infty - \omega$ diagram tend to coalesce. The pitching mode is unstable yielding an open-loop flutter velocity $V_F^{\mathsf{OL}} = 108.66$ m/s almost perfectly matching with the reference value available in literature $V_F^{\mathsf{Exp}} = 108.57$ m/s. [88]

5.2.2 Active control system design

The secondary objective of the present work is to design a flutter suppression active control system for the BACT wing, e.g. in such a way that the flutter velocity V_F is increased by $10\% - 15\%$. From a regulatory point of view such an achievement is highly favourable since it is necessary to demonstrate flutter clearance within a flight envelope expanded by 15% on V_D.

More precisely we choose a very simple active control system architecture based on a Proportional-Integral (PI) feedback of the flap control surface, which can be represented as follows within the frequency domain:

$$\delta = \left([\, \mathbf{D}_P \,] + \frac{1}{s} [\, \mathbf{D}_I \,] \right) \{ \boldsymbol{q} \} \tag{5.8}$$

where the proportional and integral gain matrices $[\, \mathbf{D}_P \,], [\, \mathbf{D}_I \,] \in \mathbb{R}^{1\times 2}$ are unknown. It is now possible to assess the closed-loop dynamic stability properties of the BACT wing by means of the non-linear root-tracking procedure as applied to the following matrix, resulting from the additional contributions associated with the active control system:

$$\begin{aligned} [\, \mathbf{B}(s, V_\infty, [\, \mathbf{D}_P \,], [\, \mathbf{D}_I \,]) \,] = [\, \mathbf{A}(s, V_\infty) \,] - \left(s^2 [\, \mathbf{M}_c \,] + s \frac{L_a}{V_\infty} [\, \mathbf{C}_c \,] + [\, \mathbf{K}_c \,] \right) [\, \mathbf{D}_P \,] \\ - \left(s [\, \mathbf{M}_c \,] + \frac{L_a}{V_\infty} [\, \mathbf{C}_c \,] + \frac{1}{s} [\, \mathbf{K}_c \,] \right) [\, \mathbf{D}_I \,]. \end{aligned} \tag{5.9}$$

The unknown proportional and integral gain matrices $[\,\mathbf{D}_P\,]$, $[\,\mathbf{D}_I\,]$ should be computed in such a way that the stability of the pitching mode is increased while the stability of the pitching mode is unaltered. In other terms the $V_\infty - g$ diagram of the closed loop aeroservoelastic system should match as closely as possible a user's defined target $V_\infty - g^{\mathsf{Tgt}}$ diagram. Such a task is not trivial since we are not focusing on a single flight condition but we are trying to design an active control system robust enough to provide the desired stability augmentation capabilities on the whole flight envelope. With reference to Figure 5.17 we resort to a multi-objective optimization strategy based on Genetic Algorithms (GA). The unknown proportional and integral gain matrices $[\,\mathbf{D}_P\,]$, $[\,\mathbf{D}_I\,]$ are computed solving an evolution-like problem, minimizing the following weighted-sum functional:

$$\mathcal{J}([\,\mathbf{D}_P\,],[\,\mathbf{D}_I\,]) = \frac{1}{2}\frac{\|g - g^{\mathsf{Tgt}}\|^2}{\|g^{\mathsf{Tgt}}\|^2} + \frac{1}{2}\frac{\|[\,\mathbf{D}_P\,]\|^2}{D_{\mathsf{Max}}^2} + \frac{1}{2}\frac{\|[\,\mathbf{D}_I\,]\|^2}{D_{\mathsf{Max}}^2}, \tag{5.10}$$

where the first term is related to stability augmentation while the other terms are related to active control system energy attenuation. The knob D_{Max} can be used to adjust the relative weight between these two opposing requirements.

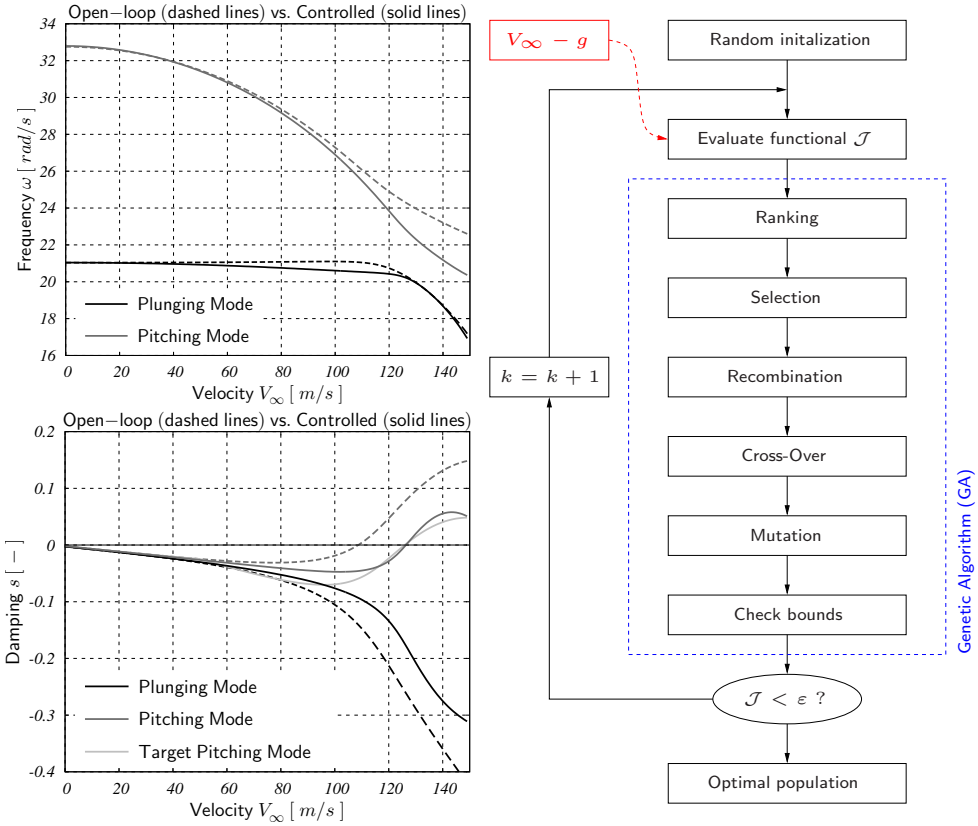

Figure 5.17: Closed-loop $V_\infty - \omega$ and $V_\infty - g$ diagrams for the BACT wing.

In Figure 5.17 the closed-loop $V_\infty - \omega$ and $V_\infty - g$ diagrams for the BACT wing are compared with the open-loop and with the user's defined target ones. It is remarkable that the stability of the plunging mode is minimally altered while the stability of the pitching mode is significantly augmented with a closed-loop flutter velocity of $V_F^{\mathsf{CL}} = 126.37$ m/s, more or less 15% higher than the open-loop value.

Besides the the analysis of the stability properties, it is also convenient to run a numerical simulation formally identical to a wind-tunnel or in-flight experimental campaign. Such a "direct simulation" procedure paves the way for the investigation more in detail of the behaviour of the BACT wing near-by the flutter point. To this end it is possible to perform a deep-dive on how the robustness of the active control system is affected by the sensors (mono-directional accelerometers) and actuators (hydraulic servo-systems with saturation set at $\overline{\delta} = 12^\circ$) modelled with reference to experimental data. Moreover the effects of the digital realization of the active control system are also modelled by including a pseudo-integrator to reconstruct the position given the outputs of the accelerometers and an anti-aliasing analogic filter.

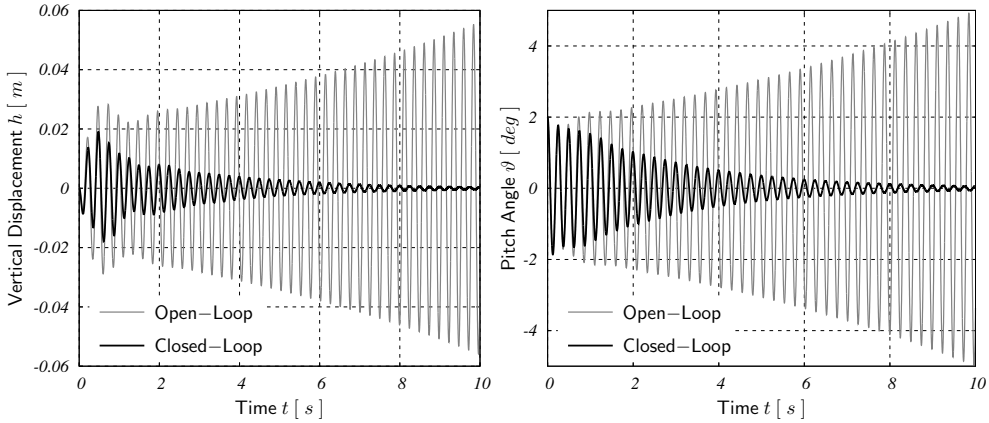

Figure 5.18: Vertical displacement h (left) and pitch angle θ (right) at $V_\infty = 1.05 V_F^{\mathsf{OL}}$.

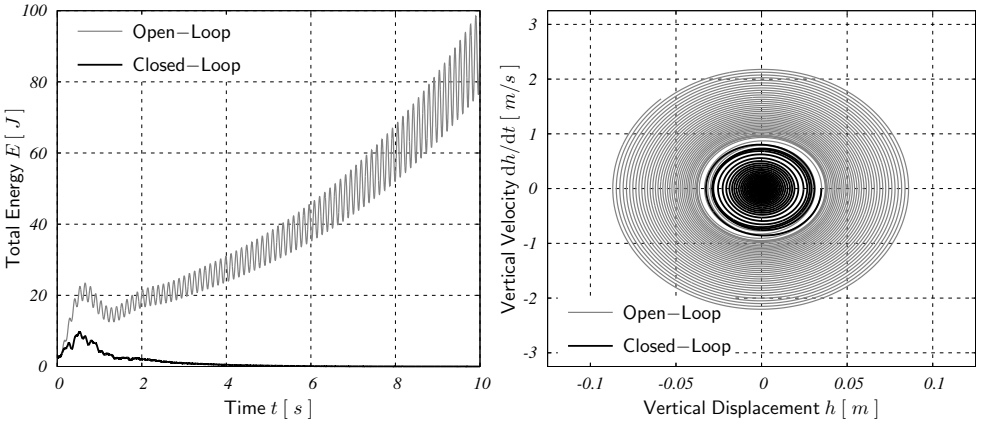

Figure 5.19: Total energy E (left) and phase-space plot (right) at $V_\infty = 1.05 V_F^{\mathsf{OL}}$.

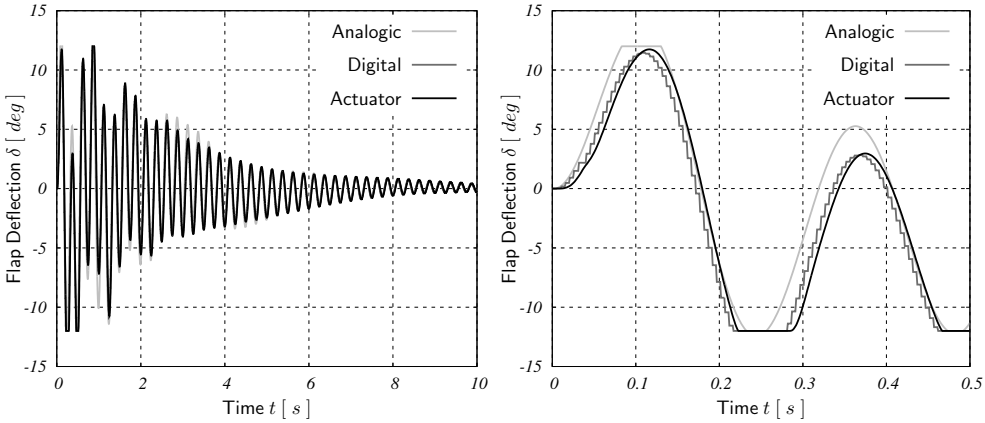

Figure 5.20: Flap deflection δ (left) together with a zoom (right) at $V_\infty = 1.05 V_F^{\mathsf{OL}}$.

In Figures 5.18 and 5.19 the numerical results of the direct simulations of the open-loop and closed-loop (with the designed PI active control system active) behaviour of the BACT wing are presented. Firstly it is possible to observe that beyond the open-loop flutter velocity $V_F^{\mathsf{OL}} = 108.66$ m/s the BACT wing is unstable to a small perturbation of the initial condition of the pitch angle $\theta_0 = 2°$, with both plunge and pitch d.o.f. rapidly diverging to infinity together with the total energy. Viceversa when the active control system is switched on it is possible to verify the robustness of the designed PI feedback law. In fact both both plunge and pitch d.o.f. rapidly converge to zero together with the total energy. Finally in Figure 5.20 the time history of the flap deflection corresponding to the designed active control system law is presented for analogic or digital implementations. It is interesting to highlight the saturation of the hydraulic actuators at $\overline{\delta} = 12°$, occurring within the first time instants. Moreover it is worthwhile to remark the significant time delay between the numerical results associated with an analogic implementation and a more realistic digital implementation (including within the verification model also the anti-aliasing analogic filter).

5.2.3 High-fidelity model

The final objective of the present work is to verify the performances of the designed flutter suppression active control system for the BACT wing by means of a non-linear, high-fidelity but expensive model (surveying both Euler and RANS modelling options). Preliminarly we stick to a two-dimensional approximation also for the high fidelity model. Of course further three-dimensional high-fidelity direct simulations are required in order to fully assess the potential of the proposed flutter suppression strategy. To this end we repeat with a high-fidelity non-linear model the post-flutter direct simulations presented above for a low-fidelity linear model with control system on and off. This strategy yields a significant added value to the workflow since it makes possible to appreciate how important the neglected non-linear effects actually are and therefore the robustness of the designed active control system.

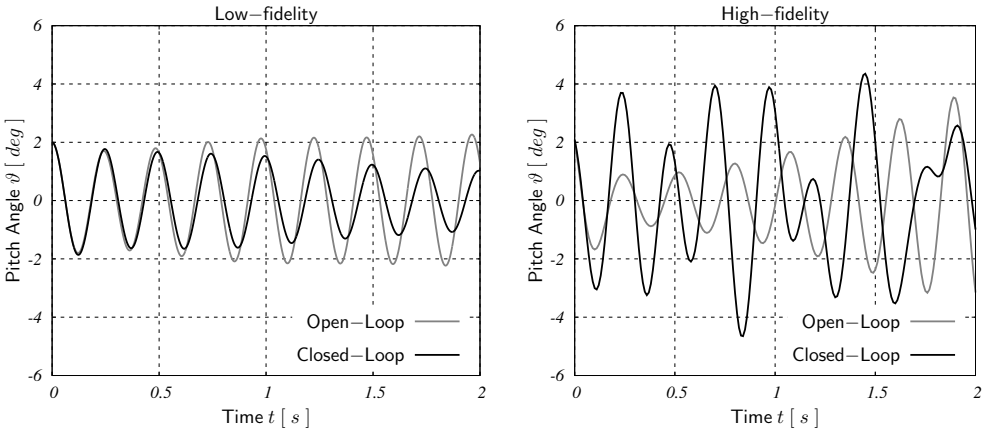

Figure 5.21: Pitch angle θ compared between low-fidelity (left) and high-fidelity models.

In Figure 5.21 the numerical results of the direct simulations of the open-loop and closed-loop behaviour of the BACT wing computed with the low-fidelity model are compared with those of the high-fidelity model. Firstly it is interesting to observe that the open-loop responses are significantly different, with the pitch angle time history predicted by the high-fidelity model diverging much more rapidly than the low-fidelity model (with maximum amplitude almost doubled at $t = 2$ s). Moreover it is worthwhile to stress that the closed-loop responses do not provide encouraging insights on the robustness of the designed active control system. In fact within the high-fidelity framework the active control system is not robust enough to drive the total energy of the system to zero as observed within the low-fidelity framework. On the contrary the PI feedback only limits the total energy below a rather high threshold with $\Delta\theta \simeq \pm 4°$.

6

Conclusions

The reduced weight and improved efficiency of modern, highly flexible, aeronautical structures (as a consequence of multidisciplinary optimization procedures and the extensive use of composite materials) result in a smaller and smaller separation of rigid and elastic modes frequency ranges. Therefore the availability of an integrated environment for tackling both static (stability derivatives correction, control surfaces efficiency, non-linear trim of maneuvering flexible aircraft) and/or dynamic (flutter, gust and turbulence response, active control systems design) aeroservoelastic problems is almost mandatory from the very beginning of the design process. Together with the availability of more and more powerful computing resources, current trends pursue the adoption of high-fidelity tools and state-of-the-art technology within the very active and fruitful research fields of Computational Structural Dynamics (CSD), Multibody System Dynamics (MSD) and Computational Fluid Dynamics (CFD). This choice is somehow obliged when dealing with non-linear aeroservoelastic phenomena, such as transonic flutter, aileron buzz and buffeting.

In the present work we illustrated the design and implementation of a platform for solving multidisciplinary non-linear Fluid-Structure Interaction (FSI) problems with a partitioned approach, that is coupling high-fidelity state-of-the-art CSD/MSD and CFD tools by means of robust and flexible aeroelastic interface and dedicated mesh deformation schemes. An innovative contribution to the challenging research field of Computational Aeroservoelasticity (CA) consisted in demonstrating that such a platform can be assembled using only free software. Within such a framework the structural sub-system is modelled with the Finite-Element (FE) solver Code_Aster or the Multi-Body (MB) solver MBDyn. The aerodynamic sub-system is modelled with the Finite-Volume (FV) aerodynamic solver AeroFoam which kicked-off back in 2008, as an ambitious academic experiment with the challenging target of filling the empty space left in OpenFOAM software for a density-based compressible RANS solver, and is still growing today, with more and more original features released pushing it towards real-world industrial applications. Among the innovative contributions it is worthwhile to remark: the dedicated aeroelastic interface scheme based on Moving

Least Squares (MLS) interpolation strategy, providing all the functionalities necessary to link the structural sub-system with the aerodynamic one, and the dedicated hierarchical mesh deformation tool for dealing with moving boundary problems in Arbitrary Lagrangian Eulerian (ALE) formulation.

The credibility of the proposed aeroservoelastic analysis toolbox was successfully assessed by tackling a set of realistic static and dynamic problems and comparing the results with reference experimental and numerical data available in literature. More in particular we investigated the sensitivity to different modelling options for representing the aerodynamic sub-system. In order to strike the best balance between accuracy of the results and computational efficiency, we chose, within the hierarchy of tools available the lowest-fidelity Doublet Lattice Method (DLM) or the Non-Linear Full Potential (NLFP) equations or the Euler equations or the highest-fidelity Reynolds Averaged Navier-Stokes (RANS) equations. To begin with we illustrated the static aeroelastic benchmark test problem of computing the reference equilibrium or "trim" configuration of the HiReNASD wing. Such an example is particularly interesting because it was selected as benchmark test problem for the 1-st AIAA Aeroelastic Prediction Workshop series with the objective of providing an impartial forum for the assessment of state-of-the-art CA methods. Successively we presented the numerical results for the non-linear aeroservoelastic trim of a free-flying A320 aircraft equipped with innovative passive aeroelastic wing tip devices and carried out a detailed comparison with the results of Nastran, a "de-facto" standard tool within the aeronautical industry. Moreover we tackled the classical dynamic aeroelastic benchmark test problem of computing the transonic flutter boundary of the AGARD 445.6 wing. Finally we surveyed an example aeroservoelastic problem of how to design a flutter suppression active control system to operate within the highly non-linear transonic regime with a linear, low-fidelity but efficient model and then verify the performances with a non-linear, high-fidelity but expensive model. More precisely we designed a simple Proportional-Integral (PI) active control system by means of a multi-objective optimization strategy based on Genetic Algorithms (GA).

However we do know that our effort has only been a small step. In fact significant improvements are still required to allow a more extensive and routinary usage of Computational Aeroservoelasticity. To this end many challenging opportunities for future developments can be clearly identified, with three main lines of actions:

a) on a "low" (programming) level there are still some routes to be fully explored in order to reduce the turn-around times of high fidelity CSD/CFD tools and to simplify the aeroservoelastic model set-up procedures, with particular focus on the interface scheme and mesh deformation strategy. Within the "low" level line of action it is worthwhile to remark the opportunities associated with the design and implementation of a mixed density and pressure-based kernel for CFD tools (clustering the best of both, e.g. massively parallel implicit multigrid time stepping schemes) and with robust dynamic mesh handling techniques (seamless integration of mesh deformation, Generic Grid Interface and Chimera approaches). Leveraging effectively these opportunities would surely impact positively the credibility of CA tools, not only within an academic environment but also in the industrial world.

b) on a “mid” (integration) level there are many opportunities to be explored in terms of multidisciplinary integration of different tools. Moreover this line of action would provide precious stress tests for a continuous improvement of the interface scheme. To begin with it would be interesting to suitably frame thermal analysis tools (possibly licensed as free software) within the proposed CA toolbox, as required e.g. by turbomachinery problems. Moreover it would be remarkable to integrate the proposed CA toolbox within an automatic optimization platform based e.g. on genetic algorithms.

c) finally on a “high” (application) level there are plenty of opportunities to be explored, e.g. the most appealing and challenging testbed for the proposed CA toolbox would be the numerical simulation of a maneuvering helicopter with moving meshes, unsteady aerodynamics, structural deformability and active control systems all together at once.

Bibliography

[1] H. Ashley. "Role of Shocks in the Sub-Transonic Flutter Phenomena". *Journal of Aircraft, Vol. 17, No. 3*, 1980.

[2] J. Ayre and F. Gasperoni. "A Successfull Business Model for Free Software". *1-st International Conference on Open Source Systems*, 2005.

[3] K. J. Badcock, S. Timme, S. Marques, H. Khodaparast, M. Prandina, J. E. Mottershead, A. Swift, A. Da Ronch, and M. A. Woodgate. "Transonic aeroelastic simulation for instability searches and uncertainty analysis". *Progress in Aerospace Sciences*, 2011.

[4] R. J. Beaubien, F. Nitsche, and D. Feszty. "Time and Frequency Domain Flutter Solutions for the AGARD 445.6 Wing". *International Forum on Aeroelasticity and Structural Dynamics*, 2005.

[5] K. Becker and J. Vassberg. "Numerical Aerodynamics in Transport Aircraft Design". *Notes on Numerical Fluid Mechanics*, 2009.

[6] J. A. Benek, P. G. Buning, and J. L. Steger. "A 3D Chimera Grid Embedding Technique". *7-th Computational Fluid Dynamics Conference*, 1985.

[7] R. M. Bennet and J. W. Edwards. "An Overview of Recent Developments in Computational Aeroelasticity". *29-th AIAA Fluid Dynamics Conference*, 1998.

[8] M. Biava, W. Khier, and L. Vigevano. "CFD Prediction of Air Flow Past a Full Helicopter Configuration". *Aerospace Science and Technology*, 2011.

[9] R. L. Bisplinghoff, H. Ashley, and R. L. Halfman. *Aeroelasticity*. Dover, 1996.

[10] J. Blazek. *Computational Fluid Dynamics: Principles and Applications*. Oxford University Press, 2001.

[11] F. Bos. "Moving and Deforming Meshes for Fapping Fight at Low Reynolds Numbers". *5-th OpenFOAM Workshop*, 2005.

[12] L. Cambier and M. Gazaix. "elsA: an Efficient Object-Oriented Solution to CFD Complexity". *AIAA Paper 2002-0108*, 2002.

[13] E. Carson Yates. "AGARD Standard Aeroelastic Configurations for Dynamic Response. Candidate Configuration I Wing 445.6". *AIAA Technical Memorandum 100492*, 1987.

[14] M. Castellani, S. Ricci, and G. Romanelli. "Multi-Fidelity Design of Aeroelastic Wing Tip Devices". *53-rd AIAA/ASME/ASCE Structures, Structural Dynamics and Materials Conference*, 2012.

[15] L. Cavagna, P. Masarati, and G. Quaranta. "Coupled Multibody/CFD Simulation of Maneuvering Flexible Aircraft". *Journal of Aircraft, Vol. 48, No. 1*, 2011.

[16] L. Cavagna, G. Quaranta, G. L. Ghiringhelli, and P. Mantegazza. "Efficient Application of CFD Aeroelastic Methods Using Commercial Software". *International Forum on Aeroelasticity and Structural Dynamics*, 2005.

[17] L. Cavagna, G. Quaranta, and P. Mantegazza. "Application of Navier-Stokes Simulations for Aeroelastic Stability Assessment in Transonic Regime". *Computers & Structures, Vol. 85, No. 11*, 2007.

[18] L. Cavagna, S. Ricci, and L. Travaglini. "Structural Sizing and Aeroelastic Optimization in Aircraft Conceptual Design using NeoCASS suite". *13-th AIAA Multidisciplinary Analysis Optimization Conference*, 2010.

[19] L. Cavagna, S. Ricci, and L. Travaglini. "NeoCASS: an Integrated Tool for Structural Sizing, Aeroelastic Analysis and MDO at Conceptual Design Level". *AIAA Atmospheric Flight Mechanics Conference*, 2010.

[20] P. Chwalowski, J. P. Florance, J. Heeg, C. D. Wieseman, and B. Perry. "Preliminary Computational Analysis of the HiReNASD Configuration in Preparation for the Aeroelastic Prediction Workshop". *International Forum on Aeroelasticity and Structural Dynamics*, 2011.

[21] M. J. de C. Henshaw, K. J. Badcock, G. A. Vio, C. B. Allen, J. Chamberlain, I. Kaynes, G. Dimitriadis, J. E. Cooper, M. A. Woodgate, A. M. Rampurawala, D. Jones, C. Fenwick, A. L. Gaitonde, M. A. Taylor, D. S. Amor, T. A. Eccles, and C. J. Denley. "Non-linear Aeroelastic Prediction for Aircraft Applications". *Progress in Aerospace Sciences*, 2007.

[22] J. Donea, A. Huerta, J. P. Ponthot, and A. Rodriguez. "Arbitrary Lagrangian Eulerian Methods". *Computational Methods for Transient Analysis*, 1983.

[23] P. Eliasson. "Edge, a Navier-Stokes Solver for Unstructured Grids". *Finite Volumes for Complex Applications*, 2002.

[24] P. Eliasson and S. H. Peng. "Drag Prediction for the DLR-F6 Wing-Body Configuration Using the Edge solver". *45-th AIAA Aerospace Sciences Meeting*, 2007.

[25] T. Fanion, M. Fernandez, and P. Le Tallec. "Deriving Adequate Formulations for Fluid-Structure Interaction Problems: From ALE to Transpiration". *INRIA Rapport de Recherche 3879*, 2000.

[26] C. Farhat, P. Geuzaine, and G. Brown. "Application of a Three-Field Non-Linear Fluid-Structure Formulation to the Prediction of the Aeroelastic Parameters of a F-16 Fighter". *Computers & Fluids, Vol. 32, No. 3*, 2002.

[27] C. Farhat, P. Geuzaine, and C. Grandmon. "The Discrete Geometric Conservation Law and the Nonlinear Stability of ALE Schemes for the Solution of Flow Problems on Moving Grids". *Journal of Computational Physics, Vol. 174*, 2001.

[28] M. Feistauer, J. Felcman, and I. Straškraba. *Mathematical and Computational Methods for Compressible Flow.* Oxford University Press, 2003.

[29] J. H. Ferziger and M. Peric. *Computational Methods for Fluid Dynamics.* Springer, 1996.

[30] L. Formaggia and F. Nobile. "A Stability Analysis for the Arbitrary Lagrangian Eulerian Formulation with Finite Elements". *International Journal of Numerical Methods in Engineering*, 1999.

[31] L. Formaggia and V. Selmin. "A Unified Construction of Finite Element and Finite Volume Discretizations for Compressible Flows". *International Journal of Numerical Methods in Engineering*, 1996.

[32] T. Gerhold, O. Friederich, J. Evans, and M. Galle. "Calculation of Complex Three-Dimensional Configurations Employing the DLR TAU Code". *AIAA Paper 1997-0167*, 1997.

[33] M. Ghommem, A. H. Nayfeh, and M. R. Hajj. "Control of Limit Cycle Oscillations of a Two-Dimensional Aeroelastic System". *Mathematical Problems in Engineering*, 2009.

[34] W. G. Gray and M. A. Celia. "On the Use of Generalized Functions in Engineering Analysis". *Journal of Applied Engineering, Vol. 6, No. 1*, 1990.

[35] C. J. Greenshields, H. G. Weller, L. Gasparini, and J. M. Reese. "Implementation of Semi-Discrete, Non-Staggered Central Schemes in a Colocated, Polyhedral, Finite Volume Framework, for High-Speed Viscous Flows". *International Journal of Numerical Methods in Fluids*, 2009.

[36] R. J. Hirsch. *Numerical Computation of Internal & External Flows.* Wiley, 1989.

[37] T. H. Holst and T. H. Pullman. "Aerodynamic Shape Optimization Using a Real Number Encoded Genetic Algorithm". *AIAA Technical Paper 2463*, 2001.

[38] M. Islam, F. Decker, E. de Villiers, A. Jackson, J. Gines, T. Grahs, A. Gitt-Gehrke, and J. Comas. "Application of Detached-Eddy Simulation for Automotive Aerodynamics Development". *SAE World Congress & Exhibition*, 2009.

[39] D. Isola, A. Guardone, and G. Quaranta. "Arbitrary Lagrangian Eulerian formulation for Two-Dimensional Flows Using Dynamic Meshes With Edge Swapping". *Journal of Computational Physics, Vol. 230*, 2011.

[40] A. Jameson. "Analysis and Design of Numerical Schemes for Gas Dynamics 1: Artificial Diffusion, Upwind Biasing, Limiters and Their Effect on Accuracy and Multigrid Convergence". *NASA Contractor Report 196476*, 1994.

[41] A. Jameson. "Analysis and Design of Numerical Schemes for Gas Dynamics 2: Artificial Diffusion and Discrete Shock Structure". *NASA Contractor Report 196477*, 1994.

[42] H. Jasak. "Dynamic Mesh Handling in OpenFOAM". *47-th AIAA Aerospace Sciences Meeting*, 2009.

[43] H. Jasak and Z. Tuković. "Dynamic Mesh Handling in OpenFOAM Applied to Fluid-Structure Interaction Simulations". *5-th European Conference on Computational Fluid Dynamics*, 2010.

[44] W. H Jou. "A Systems Approach to CFD Code Development". *International Council of the Aeronautical Sciences*, 1998.

[45] R. Kamakoti and W. Shyy. "Fluid-Structure Interaction for Aeroelastic Application". *Progress in Aerospace Sciences*, 2004.

[46] E. M. Lee-Rausch and J. T. Batina. "Calculation of AGARD Wing 445.6 Flutter Using Navier-Stokes Aerodynamics". *AIAA Technical Paper 3476*, 1993.

[47] E. M. Lee-Rausch and J. T. Batina. "Wing Flutter Boundary Prediction Using Unsteady Euler Aerodynamics". *NASA Technical Memorandum 107732*, 1993.

[48] R. J. LeVeque. *Numerical Methods for Conservation Laws*. Birkäuser, 1992.

[49] R. J. LeVeque. *Finite Volume Methods for Hyperbolic Problems*. Cambridge University Press, 2002.

[50] M. J. Lighthill. "On displacement thickness". *Journal of Computational Physics, Vol. 4*, 1958.

[51] M. J. Lighthill. *Introduction to Fourier Analysis and Generalized Functions*. Cambridge University Press, 1975.

[52] E. Livne. "Future of Airplane Aeroservoelasticity". *Journal of Aircraft, Vol. 40, No. 6*, 2003.

[53] E. Livne and T. A. Weisshaar. "Aeroelasticity of Nonconventional Airplane Configurations: Past and Future". *Journal of Aircraft, Vol. 40, No. 6*, 2003.

[54] P. Mantegazza. "Attached-Mean Axes and Calculation of Deformable Static and Damped-Undamped Vibration Modes of Free-Free Structure". *Journal of Aeroelasticity and Structural Dynamics, Vol. 2, No. 1*, 2011.

[55] L. Meirovitch. *Introduction to Dynamics and Control*. Wiley, 1985.

[56] R. D. Milne. "Some Remarks on the Dynamics of Deformable Bodies". *AIAA Journal, Vol. 6, No. 3*, 1968.

[57] R. D. Milne and D. K. Schmidt. "Hybrid State Equations of Motion for Flexible Bodies in Terms of Quasi-Coordinates". *Journal of Control, Guidance and Dynamics, Vol. 14, No. 5*, 1991.

[58] E. Moglen and R. Stallman. "The GNU General Public License (GPL)". *Free Software Foundation Inc.*, 1991.

[59] S. A. Morton, R. M. Cummings, and D. Kholodar. "High Resolution Turbulence Treatment of F-18 Tail Buffet". *Journal of Aircraft, Vol. 44, No. 6*, 2007.

[60] A. Parrinello and P. Mantegazza. "Independent Two-Fields Solution for Full-Potential Unsteady Transonic Flows". *AIAA Journal, Vol. 48, No. 7*, 2010.

[61] M. Patil and D. Hodges. "Flight Dynamics of Highly Flexible Flying Wings". *Journal of Aircraft, Vol. 43, No. 6*, 2006.

[62] S. B. Pope. *Turbulent Flows*. Cambridge University Press, 2000.

[63] G. Quaranta, P. Masarati, and P. Mantegazza. "A Conservative Mesh-Free Approach for Fluid-Structure Interface Problems". *Coupled Problems*, 2005.

[64] A. Quarteroni, R. Sacco, and F. Saleri. *Numerical Mathematics*. Springer, 2004.

[65] A. M. Rampurawala and K. J. Badcock. "Buzz Prediction for a Supersonic Transport Configuration". *International Forum of Aeroelasticity and Structural Dynamics*, 2005.

[66] D. E. Raveh. "Computational-Fluid-Dynamics-Based Aeroelastic Analysis and Structural Design Optimization: a Researcher's Perspective". *Computer Methods in Applied Mechanics and Engineering, Vol. 194, No. 30*, 2005.

[67] D. E. Raveh, Y. Levy, and M. Karpel. "Structural Optimization Using Computational Aerodynamics". *AIAA Journal, Vol. 38, No. 10*, 2000.

[68] S. Rebay. "Efficient Unstructured Mesh Generation by Means of Delaunay Triangulation and Bowyer-Watson Algorithm". *Journal of Computational Physics, Vol. 106*, 1993.

[69] D. M. Richwine and D. F. Fisher. "In-Flight Leading-Edge Extension Vortex Flow-Field Survey Measurements on a F-18 Aircraft at High Angle of Attack". *NASA Technical Memorandum 4398*, 1992.

[70] W. P. Rodden and J. R. Love. "Equation of Motion of a Quasi-Steady Flight Vehicle Utilizing Restained Static Aeroelastic Characteristics". *Journal of Aircraft, Vol. 22, No. 9*, 1985.

[71] G. Romanelli, M. Castellani, and S. Ricci. "Coupled CSD/CFD Non-Linear Aeroelastic Trim of Free-Flying Flexible Aircraft". *53-rd AIAA/ASME/ASCE Structures, Structural Dynamics and Materials Conference*, 2012.

[72] G. Romanelli and L. Mangani. "Object-Oriented Redesign of Density-Based RANS Solver AeroFoam for Aerodynamic/Aeroelastic Industrial Applications". *5-th OpenCFD Conference*, 2010.

[73] G. Romanelli, E. Serioli, and P. Mantegazza. "A New Accurate Compressible Solver for Aerodynamic Applications". *3-rd OpenFOAM Workshop*, 2008.

[74] G. Romanelli, E. Serioli, and P. Mantegazza. "A Free Approach to Modern Computational Aeroelasticity". *48-th AIAA Aerospace Sciences Meeting*, 2009.

[75] V. Schmitt and F. Charpin. "Experimental Data Base for Computer Program Assessment: *Pressure Distribution on the ONERA M6 Wing at Transonic Mach Numbers*". *AGARD Advisory Report 138*, 1979.

[76] D. M. Schuster, D. D. Liu, and L. J. Huttsell. "Computational Aeroelasticity: Success, Progress, Challenge". *Journal of Aircraft, Vol. 40, No. 5*, 2003.

[77] A. H. Shapiro. *Dynamics and Thermodynamics of Compressible Fluid Flows*. Crieger, 1983.

[78] D. Shepard. "A Two-Dimensional Interpolation Function for Irregularly-Spaced Data". *ACM National Conference*, 1968.

[79] R. Steijl and G. Barakos. "A Sliding Mesh Algorithm for CFD Analysis of Helicopter Rotor-Fuselage Aerodynamics". *International Journal of Numerical Methods in Fluids, Vol. 58*, 2008.

[80] C. H. Stephens, A. S. Arena, and K. K. Gupta. "Application of the Transpiration Method for Aeroservoelastic Prediction Using CFD". *AIAA Technical Report 2071*, 1998.

[81] J. J. Thibert, M. Grandjacques, and L. H. Ohman. "Experimental Data Base for Computer Program Assessment: *NACA 0012 Airfoil*". *AGARD Advisory Report 138*, 1979.

[82] Various Authors. "Code_Aster v.10.0.0 User's Guide". *www.code-aster.org*, 2010.

[83] Various Authors. "Airworthiness Standards for Transport Category Airplanes Part-25". *Federal Aviation Administration www.faa.gov*, 2011.

[84] Various Authors. "Certification Standards for Large Airplanes CS-25". *European Aviation Safety Agency www.easa.eu*, 2011.

[85] Various Authors. "MBDyn v.1.4.0 User's Guide". *www.mbdyn.org*, 2011.

[86] Various Authors. "OpenFOAM v.2.0.0 User's Guide". *www.openfoam.com*, 2011.

[87] J. B. Vos, A. Rizzi, D. Darracq, and E. H. Hirschel. "Navier-Stokes Solvers in European Aircraft Design". *Progress in Aerospace Sciences*, 2002.

[88] M. R. Waszak. "Modeling the Benchmark Active Control Technology Wind-Tunnel Model for Application To Flutter Suppression". *AIAA Technical Paper 3437*, 1996.

[89] M. R. Waszak and D. K. Schmidt. "Flight Dynamics of Aeroelastic Vehicles". *Journal of Aircraft, Vol. 25, No. 6*, 1988.

[90] R. T. Whitcomb. "A Design Approach and Selected Wind-Tunnel Results at High Subsonic Speeds for Wing-Tip Mounted Winglets". *NASA Technical Note 8260*, 1976.

[91] J. Witteveen. "Explicit Mesh Deformation Using Inverse Distance Weighting Interpolation". *47-th AIAA Aerospace Sciences Meeting*, 2009.

[92] R. Yurkovich. "Status of Unsteady Aerodynamic Prediction for Flutter of High-Performance Aircraft". *Journal of Aircraft, Vol. 40, No. 5*, 2003.

[93] O. Zienkiewicz and J. Zhu. "Adaptivity and Mesh Generation". *International Journal of Numerical Methods in Engineering*, 1991.